DESIGN AND FABRICATION OF FIBER OPTIC INTEGRATED SENSOR MICROSYSTEM FOR INTERVENTIONAL MEDICAL DEVICES

by

Oğuz Kaan Erden

B.S., Electrical and Electronics Engineering, Istanbul Bilgi University, 2017

Submitted to the Institute for Graduate Studies in
Science and Engineering in partial fulfillment of
the requirements for the degree of
Master of Science

Graduate Program in Electrical and Electronics Engineering
Boğaziçi University
2020

ACKNOWLEDGEMENTS

I would like to express my gratitude to my thesis supervisor Prof. Arda Deniz Yalçınkaya for giving me an opportunity to be a part of this project. His guidance and support throught this study was extremely valuable for me.

I would also show my appreciation to Prof. Onur Ferhanoğlu for his great support. The precious time he spend for this study is very important to me. I would also like to thank to Prof. Sema Dumanlı Oktar for joining to my thesis committee. Her positiveness in the lab has always been an inspiration for me.

I express my gratitude to Parviz Zolfaghari for his valuable co-operation. We were often in contact and with him throughout two years. He contributed this thesis with COMSOL simulations for pressure sensing, and we collaborated on the every stage of pressure sensor, temperature sensor and producing the holders which are going to use to couple fibers with sensors. It was a pleasure to work together.

I would like to express my deepest thanks to my brother, my comrade, my blood Semih Ramazanoğlu. Thanks to his partnership and support, this difficult process has become easy and enjoyful.

I would also like to say thanks to the members of BETA and MNCL Laboratories, Deniz Özen, Barış Can Efe, Berk Çamlı, Berk As, Erdem Çil, Naci Pekçokgüler, Mustafa Becermiş, Ertaç Kızılca, Baran Demirer, Mohammad Ahmadlou, Amin Soltani, Merve Albayrak, Hilmi Artun Oyman and Rifat Kısacık.

I would like to present my special thanks to Hasan Şahin, Mehmet Yumak and Ahmet Turan Talaş for being kind friends and their support in cleanroom processes.

I would like to thank The Scientific and Technological Research Council of Turkey (TÜBİTAK) which supported this thesis study as a part of grant EEEAG 116E814.

I would like to express my deepest appreciation to Anastasia Osipova. She has always believed in me even from hundreds of kilometers away. She has always encouraged me intellectually and emotionally.

Finally and most importantly, I would like to express my profound gratitude to my beloved parents Ayhan and Yasemin, and my dear sisters, my princesses Merve and Miray, for their endless support, encouragements, and unconditional love throughout my journey and I would like to dedicate this thesis to them.

ABSTRACT

DESIGN AND FABRICATION OF FIBER OPTIC INTEGRATED SENSOR MICROSYSTEM FOR INTERVENTIONAL MEDICAL DEVICES

In this thesis, there is presented the design, fabrication and characterization of a medical device prototype for real time monitoring of pressure, temperature and localization information for Magnetic Resonance Imaging (MRI) supported interventional radiological applications. The system allows to determine the position of the medical device used in surgery, as well as environmental conditions in real time by combining fiber optical components with micro electro mechanical system (MEMS) sensors, fabricated on an inner diameter of 2.2 mm platform. The system mainly consists of localization, temperature and pressure sensors, where each component takes measurement optically, and transmits data in the same way. The localization detection is realized due to the observation of Magneto Optical Kerr Effect (MOKE), which is a method to measure the magnetization of the sample surface by the change in the polarization of the light. In the controllable magnetic field area, which is created by gradient field, the precision is reported for steel grade 430 as 0.475 mm and for Fe_2O_3 as 4.44 mm. Ambient temperature sensing is based on absorption change in semiconductor due to variations of energy bandgap of a GaAs sample with temperature. Incident light, at a specific wavelength, on the GaAs is reflected back with the temperature change signature. The sensitivity of the sensor is reported as 0.494 nm/°C. Lastly, the environmental pressure change with respect to chamber pressure of the metallic membrane is measured interferometrically. Among different designs, the best sensitivity is reported as 1.456 mV/mmHg by 200 μm diameter sized sensor.

ÖZET

GİRİŞİMSEL TIBBİ CİHAZLAR İÇİN FİBER OPTİK TÜMLEŞİK ALGILAYICI MİKROSİSTEM TASARIMI VE ÜRETİMİ

Bu çalışmada, Manyetik Rezonans Görüntüleme (MRG) destekli girişimsel radyolojik uygulamalar için basınç, sıcaklık ve lokalizasyon bilgilerinin gerçek zamanlı olarak izlenebildiği bir tıbbi cihaz prototipinin tasarım, üretim ve karakterizasyon çalışmaları sunulmuştur. Sistem, iç çapı 2.2 mm olan bir platform üzerinde üretilen mikro elektro mekanik sistem (MEMS) sensörleri, fiber optik bileşenleri ile birleştirerek ameliyatta kullanılan tıbbi cihazın konumunu ve çevresel koşulların gerçek zamanlı olarak belirlenmesine olanak tanır. Sistem temel olarak, her bir bileşenin optik olarak ölçüm aldığı ve verileri aynı şekilde detektörlere ilettiği lokalizasyon, sıcaklık ve basınç sensörlerinden oluşur. Konum tespiti, ışığın polarizasyonundaki değişim ile örnek yüzeyinin manyetizasyonunu ölçmek için kullanılan bir yöntem olan Manyeto Optik Kerr Etkisi (MOKE) gözlemi sayesinde gerçekleştirilir. MR gradyan alanı ile oluşturulan, kontrol edilebilir 30 mT manyetik alan aralığında, hassasiyet değerleri, 430 kalite çelik için 0.475 mm ve Fe_2O_3 için 4.44 mm olarak rapor edilmiştir. Ortam sıcaklığının algılanması, GaAs yarıiletken malzemenin enerji bant aralıklarının, sıcaklığa bağlı olarak değişimi esas alınarak gerçekleştirilir. Bu değişim, sıcaklığa bağlı olarak, yarıiletkenin soğurma katsayısının değişimine sebep olmaktadır. Yarıiletkenden yansıyan ışığın dalga boyunun, yarıiletkenin ölçülmek istenen sıcaklıktaki enerji bant aralığı değeri ile orantılı olarak değişmektedir. Sensörün hassasiyeti 0.494 nm/°C olarak rapor edilmiştir. Çevresel basınç ise, metalik zarın oda basıncı baz alınarak zar üzerinde gerçekleşen bükülmenin interferometrik olarak okunması ile ölçülür. Farklı tasarlanmış membranlar arasında en iyi hassasiyet, 200 μm çaplı sensör ile 1.456 mV / mmHg olarak ölçülmüştür.

TABLE OF CONTENTS

LIST OF FIGURES

LIST OF TABLES

LIST OF SYMBOLS

d	Distance in between Membrane and the Substrate
d_s	Slit Width of the Gratings
E_0	Incident Electric Field of the Light
E_g	Bandgap Energy
I_0	Incident Intensity of the Light
$I_{\pm}1$	Intensity of the First Grating Order Light
I_T	Transmitted Intensity of the Light.
m	The Number of the Order
n	Refraction Index of Material
α	Absorption Coefficient
β	Debye Temperature
$\beta_t(i)$	Backward variable
ΔH	Change in Magnetic Field
Δx	Position Change
δ	Optical Path Difference
δ_p	Phase Retardation for p-polarized Light
δ_s	Phase Retardation for s-polarized Light
$\varepsilon_s^{(w)}$	Modal Amplitude for s-polarized Light
$\varepsilon_p^{(w)}$	Modal Amplitude for p-polarized Light
ε	Ellipticity Degree
κ	Extinction Coefficient
λ	Wavelength of the Light
λ_c	Optical Cut-off Wavelength
μ_0	Magnetic Permeability
t	Thickness
θ	Angle of the Diffraction Order
θ_k	Azimuth Degree

LIST OF ACRONYMS/ABBREVIATIONS

2D	Two Dimensional
3D	Three Dimensional
A	Absorbance
B	Magnetic Flux Density
B_0	Main Magnetic Field
CVD	Chemical Vapour Deposition
dB	Decibel
E	Electric Field
EM	Electromagnetic
EMI	Electromagnetic Interference
EMTS	Electromagnetic Tracking Systems
FBG	Fiber Bragg Gratings
Fe_2O_3	Iron (III) Oxide
FEM	Finite Element Method
FFT	Fast Fourier Transform
FID	Free Induction Decay
FOPS	Fiber Optical Pressure Sensors
FOTS	Fiber Optical Temperature Sensors
GaAs	Gallium Arsenide
GRIN	Gradient Index
H	Magnetic Field
H_2SO_4	Sulphuric Acid
H_c	Coercive Magnetic Field
HF	Hydrogen Fluoride
HIFU	High Intensity Focused Ultrasound
HMDS	Hexamethyldisilicate
IR	Infrared
LED	Light-Emitting Diode
M	Magnetization

MEMS	Micro Electro Mechanical Systems
MOKE	Magneto Optical Kerr Effect
M_r	Permanent Magnetization
M_s	Magnetization Saturation
MRI	Magnetic Resonance Imaging
N	Nitrogen Gas
NIR	Near Infrared
OPD	Optical Path Difference
OSA	Optical Spectrum Analyzer
OTS	Optical Tracking Systems
PD	Photo Diode
PM	Polarization Maintained
PVD	Physical Vapour Deposition
QWP	Quarter Wave Plate
R	Reflectance
RF	Radio Frequency
SMOKE	Surface Magneto Optical Kerr Effect
SOP	State of Polarization
SS 430	Stainless Steel Grade 430
T	Transmittance
US	Ultra Sound
UV	Ultra Violet
XF	X-Ray Fluroscopy

1. INTRODUCTION

As the inter-body biological systems are better understood, the basic features of medical devices used in interventional treatment methods are enhancing rapidly. On the one hand, while reducing their general dimensions to reduce possible risks during the operation, designs that perform more than one function have started to emerge. Therefore, minimization of the invasive diagnosis and treatment methods is leading the development of more operable biocompatible devices. In parallel with the development of micro electro mechanical systems (MEMS) in medical applications, basic sensors such as temperature and pressure which have been used in different applications for a long time, have been able to shrink into medical devices.

This thesis is a part of a TÜBİTAK project EEEAG 116E814 which presents to develop a medical device prototype for MRI-supported interventional radiological applications that can obtain temperature, pressure and location tracking information in real time by combining fiber optic lines with micro electro mechanical system (MEMS) sensors. This proposed system will provide real-time information about environmental conditions of vessel or tissue in it, and the operator will be able to report the location of the interventional device in medical applications. The literature research and working principles of the system are described below in details under subsections.

1.1. Medical Tracking Systems

Minimally invasive medical interventions can provide both a reduced risk for the patient and an increase in information about the working system of the human body [1, 2]. These minimized systems are very advantageous compared to their traditional counterparts, which involve cutting the target tissue starting from the skin. Among many of these techniques, catheter based endovascular applications shaping a considerable group of this area. Due to the necessity for the success of the operation as well as minimal tissue deformation during the operation, instrument relative to the patient's anatomy should be found and tracked as accurately as possible.

There are several tracking systems developed since the first mechanical ones [3]. Even primitive tracking methods could provide position information around in some millimeters when they first introduced, they have some disadvantages such as lack of ability to track multiple devices and operation complexity. Accordingly, there were developed some alternative methods. Ultrasonic(US) transducers were one of them as used for localization [4, 5]. However Ultrasonic sensing procedure is based on the speed of sound. In consequence of the sound wave is dependent on environmental factors, such as humidity and temperature, ultrasound tracking technique is prone to distortions.

Additionally, there are some other commonly used medical imaging techniques such as X-ray fluroscopy (XF) and optical tracking systems(OTS). The three dimensional resolution of OTS are really good to be underestimated, however, there are too many instruments that should be maintained in between them, which poses great difficulty during interventional operations [6, 7]. Besides, XF is mainly used one for catheter based applications. Although it is an important advantage of XF to be able to observe vascular structures by giving contrast agents to the vein, due to the ionizing radiation effect of X rays, the possibility of creating harmful effects in patients and healthcare workers in long-term procedures prevents XF from being the most optimal solution [8, 9].

In addition to these the promising method for monitoring is Magnetic Resonance Imaging(MRI), a safe image acquisition method with high soft tissue contrast [10, 11]. As the main advantage, MRI does not utilize ionizing radiation during operation which has some problematic issues mentioned in XF. Also, electromagnetic tracking systems(EMTS) for MRI can provide three dimensional(3D) images instead XF which can provide two dimensional(2D) images. One another major advantage is, MRI based tracking systems detect the catheter position with identifying a magnetic material at the tip of the device. They have lower resolution ratios than OTS, however, they do not need any line of sight alignments. These advantages makes MRI based systems more usable way to track catheter position in minimally invasive interventional operations [12–21].

1.2. MRI Operating Principle and Proposed System

The nuclei of atom is a charged particle and possess spin with a magnetic dipole moment, that can be represented as tiny spinning magnetic balls. Since the human body is mostly water and and water molecules contain hydrogen, to construct an image in MRI, Hydrogen H^1 nuclei is chosen, which are basically referred as protons. Without any external magnetic field, nuclei have both up-spin and down-spin dipoles which are spinning randomly around themselves. At that point, the number of up-spin dipoles are the same with down-spin ones which results in zero net magnetic moment (M=0).

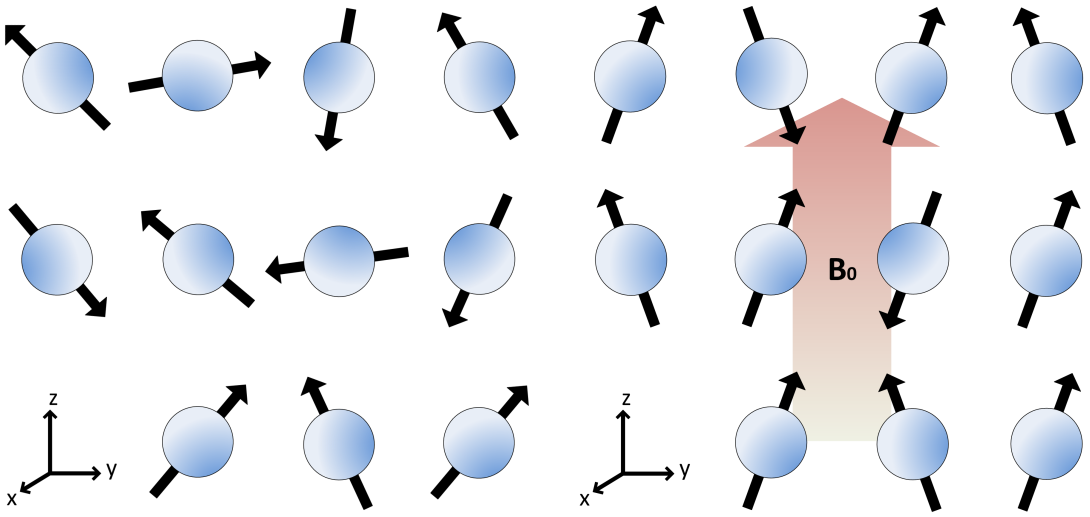

(a) (b)

Figure 1.1. The alignment of the dipoles (a) in the absence (b) in the presence of magnetic field [22].

When the external DC magnetic field $\vec{B_0}$ is applied, the dipoles are diverted and precessed in the direction of they are magnetized by an external field stimulation as shown in Figure 1.1 [22]. After the external field effect is removed, they returned to the direction defined by DC field. The emitted signal during this process is called free induction decay (FID). The FID signal at each physical point can be associated with the resonance frequency with the help of gradient magnetic fields. Frequency-position relationship can be established with motion from here.

Alternatively, there is also a pulse sequence based technique that will show the catheter position as a cursor on the MR image. Thus, the medical device can be used for both imaging of the intervention and functional examination [23, 24].In addition, inductive coupling can be used as a wireless solution for MRI tracking in medical devices [25]. A more advanced form of monitoring is the active method in which electronic components are used on the catheter tip. In this method, micro coils are used as antennas. However, micro antennas cause distortion in the MR image because they disrupt the magnetic field regularity [26]. This monitoring technique causes gaps in the MR image.

The vast majority of MRI catheter monitoring systems are based on the power and signal carrying of conductive lines [27, 28]. The main problem arising in MRI studies is that the catheters and stents made of conductive materials are heated under the RF field. Leakage currents, inductive cycles and RF fields in resonance cause medical devices to warm up [29,30]. Many studies have been proposed to overcome the heating problem. Although in the literature, there are suggested methods to solve the heating problem either by dividing long wires into specific lengths and using transformers between wire segments [30] or resonance shifting [31] methods, they have been described as difficult and unreliable ways for cable/transformer integration in catheters.

Alternatively, as a solution to the heating problem, using optical transmission, that removes the electrical cable for interventional medical devices, can significantly improve patient safety. In the literature, there are application-specific integrated circuit systems for optical communication [32, 33]. However, electrical power is supplied to such circuits, usually via a battery or by conductors.

In order to develop a fully MRI-compatible microsystem, an optoelectronic power source, such as photovoltaic cells, optical-electrical converters, and optical power transfer are required [34]. Besides, serial connected photodiodes can be used as a power source for the microsystems [35]. The main disadvantage here is, the area spent by the photodiodes connected in series is large and makes the miniaturization process difficult. As a result, it is needed opto electronical power and transmission units integrated on

single MEMS based substrate for biomedical implants.

MEMS technology, has been used in communication using light for a very long time [36]. Thanks to MEMS based structures integrated with laser sources, physically movable optical apertures and reflectors can be realized [37–39].

In this part of thesis, fiber optic lines with a MEMS structure have been proposed as an alternative for transmitting the position mark. In this approach, the phenomenon known as the Magneto-Optical Kerr Effect(MOKE), in which the change of the polarization of the light reflected from a magnetic material can be associated with the magnetization conditions of the material will be used for localization under MRI. The polarization change created by magnetic field is associated linearly to the position.

1.3. Temperature Sensing Applications and Proposed System

In interventional oncology and cardiology, many different types of methods have been used for the purpose of treatment through catheters in recent years. The main aim is the reaching the treatment area and destruction of the tissue or creating scar tissue with transferred electromagnetic energy to the diseased tissue. The primary sources of energy used for this purpose are surgical laser, high intensity focused ultrasound and radio frequency energy [40–42]. In general, it has been found that it is sufficient to expose healthy tissue to a temperature of 45-50 °C for a few seconds to permanently damage it [43]. Therefore, the feedback of the ambient temperature during the treatment will result as minimal healthy tissue destruction as possible.

The use of laser catheters has increased significantly in recent years, especially flexible catheters [44, 45]. The most important factors in laser-tissue interaction are depth of penetration, thermal effect and reflection. Monitoring ambient temperature plays an important role in determining the energy to be given, especially since the reflection will cause unintended thermal effects on the healthy tissue in the environment.

On the other hand, in recent years, the use of of High Intensity Focused Ultrasound (HIFU) method has been developing rapidly in the prostate cancer treatments. In the HIFU, focused ultrasonic waves are sent to the cancer tissue and increasing the temperature of this area up to 100 °C in a short time [46]. For the successful outcome of the treatment, preserving the healthy tissue around is as important as the complete destruction of the cancer tissue. Therefore, the temperature rise caused by ultrasonic waves should be measured precisely in real time.

As another method, radio frequency energy is frequently used in the treatment of atrial fibrillation disease [47]. The applied RF current electrically isolates the regional fibrillation sources and ensures that the heart gets the normal beat rhythm. The major disadvantage of this treatment method is the risk of stroke due to temperature change during the operation. Therefore, it is necessary to monitor the temperature increase on the contact surface of the cardiac tissue and the electrode while RF energy is applied.

In this part of the study, there is designing a fiber optical temperature sensor which depends on energy band gap change method to detect the temperature value. This method is based on the principle that the wavelength of the light, reflected from the semiconductor, changes proportional to the energy band gap value of the semiconductor at the desired temperature. Since the light intensity reflected from the Semiconductor and returning to the fiber will change with the temperature, it is possible to detect the temperature at the catheter tip by measuring the intensity and spectrum of the light.

1.4. Pressure Sensing Applications and Proposed System

Blood pressure in a human body is affected by lots of parameters such as muscle activities, fluids, and externally gravity and atmospheric forces. Measurement of in vivo blood pressure is a key aspect of many biomedical applications. In recent studies, it has been observed that the decrease in blood pressure during the treatment of heart failure indicates a deterioration in kidney function. Since this condition is not important to diagnose early and may result in death, measurement of blood pressure with arterial

catheter in patients with heart failure is recommended as a standard procedure [48].

Recently, the mainstream devices for pressure measurement are based on catheters and guide wires in different methods. One of them is air-charged catheters, which has a wide range of use in urological operations [49]. As an alternative method, fluid-filled catheters are very popular in urology and cardiovascular applications [50, 51]. Besides these electro-mechanical sensors, the fiber optical pressure sensors(FOPS) have become more widely used in this field over time. Thanks to there is no electrical conductivity and their geometrical versatility, they are usable for catheter based applications. Also having immunity to electromagnetic interference(EMI), and possibility of remote operation and sensing, FOPS are suitable for use in MRI rooms.

The most common working principles of FOPS for biomedical applications are based on intensity, phase and wavelength modulation and lately fiber Bragg gratings(FBG). The working principle of the light intensity modulated method basically based on the changing the amplitude of signal in light. One configuration uses a fiber guides the light to the mirror and the intensity of the light changes according to distance change in between mirror and fiber. Another method occurs a using fiber bundles instead of single fiber and a mirror. As the distance change in between coupled fibers, the intensity of transmitted light changes measurably. Accordingly in the literature, some different micro bending methods are applied to compensate changes in light source intensity or losses [52, 53].

In this section of the study, it is proposed to design a fiber optical pressure sensor based on the diffraction grating interferometer procedure to measure in-vivo blood pressure. The membrane structure to be used for pressure sensing is manufactured in a way that creates a reference pressure by micro-processing methods. This process allows the membrane to form a chamber that is kept in a sealed pressure at micro dimensions. According to environmental pressure changes, the displacement occurring on the membrane is determined interferometrically by optical reading of reflected laser beam from the membrane surface. The pressure change data is obtained by detecting the reflected light on a photodetector.

In summary, this thesis aims to develop an integrated microsystem for real time monitoring of localization, temperature and pressure information for the non-invasive medical devices used for interventions performed in MRI. The sensors to be developed will be placed on a MEMS platform and will be combined with three fibers as shown in figure 1.2. This designed platform, which fits in a medical intervention device with an internal diameter of 2.2 mm, have a cover that allows the media fluids to contact the surface of the MEMS devices but prevents leakage under the platform. The three structures on the MEMS platform that will be used for local position (Δx), temperature (T) and pressure (P) detection are located on the same substrate and are irradiated by a laser beam. The gradient index lens (GRIN-lens) at the end of the fibers provides the light emitted without scattering.

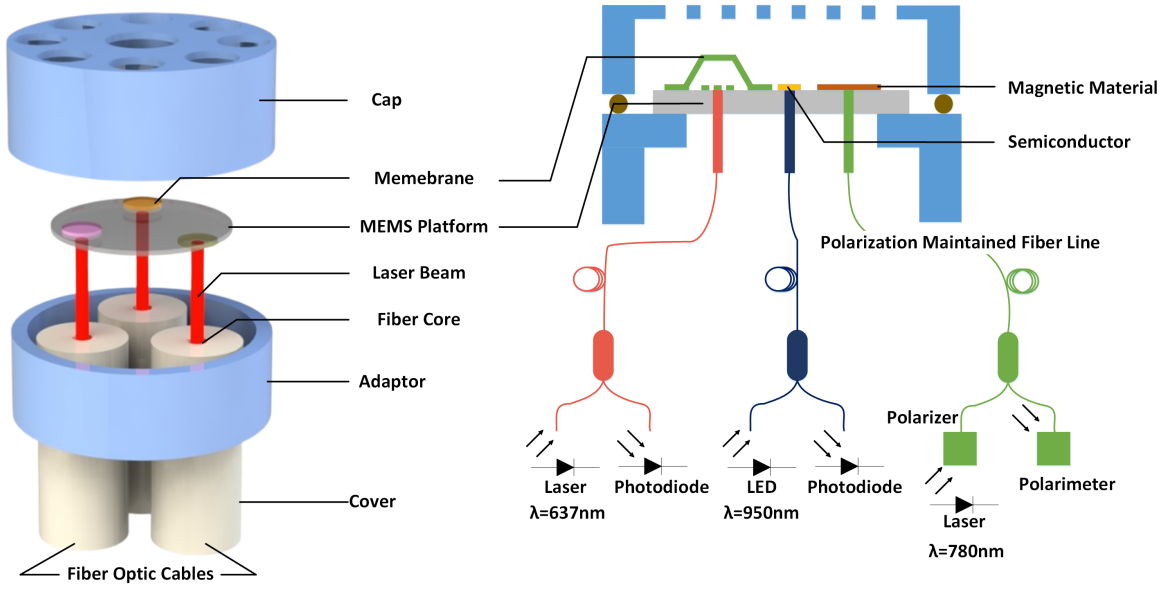

Figure 1.2. The components of microsystem and data transmission schematic.

In general, the system is discussed under three main groups for each sensing method. In Chapter 2, the position of the medical device will be determined by the magnetization of a magnetic material by changing the polarization of light due to the Kerr Effect as explained in details. Chapter 3 discusses the physical phenomenon of the change in energy bandgap as a method to detect the temperature change. Chapter 4 shows the design steps of pressure sensing method which is based on diffraction grating interferometer. Finally, Chapter 5 concludes the thesis with future work.

2. LOCALIZATION SENSING

Advances in imaging technology increase the use of minimally invasive and image-supported medical interventions. While catheter-based interventions have traditionally been performed under XF, interest in the use of magnetic resonance imaging (MRI) is growing in this area with the contribution of technological advances. For device tracking inside an MR environment, there are two methods that are commonly used: passive and active tracking. Passive tracking based on the monitoring a device within MRI images. By using contrast agents or magnetic material in device, the contrast change can be visualized [54, 55]. On the other hand, active devices with embedded antennas or RF coils can generate detectable signals for localization. One another active tracking method is the measurement of gradients, which does not rely on the visualization of MR imaging, but using the spatially varying gradients of the MR system. Besides placing three orthogonal coils to measure the induced voltage by changing magnetic fields, another mechanism is developed to measure the magneto optical effects using the gradient fields with optical sensors [56, 57].

2.1. Magneto-Optical Effects

The magneto-optical effect is caused by the interaction of light with magnetic material. Michael Faraday observed that the polarization of light passing through the magnetic field applied glass material has changed and the first magneto-optical effect is discovered. Faraday tried the same effect for the light reflected from the magnetic surface applied metal surface, but he could not observe a meaningful result from these studies due to surface defects. In 1877, John Kerr observed the magneto-optical effect while examining the polarization of light reflected from the polished electromagnet pole. Thus, the change of the polarization of the light passing through the magnetic material was called the Faraday effect, and the change of the polarization of the light reflected from the magnetic material was called the Kerr effect as shown in Figure 2.1.

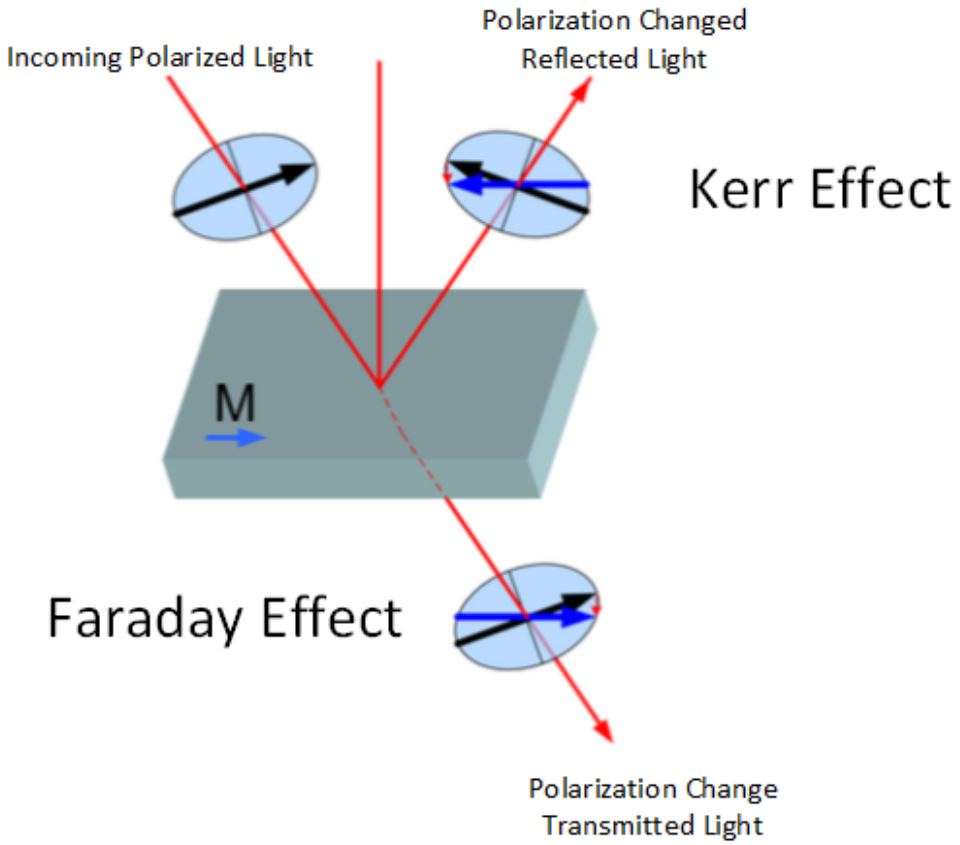

Figure 2.1. Interaction of the light with magnetic material.

Later on, Mogg et al. used the Kerr effect for surface magnetization and called it SMOKE (Surface Magneto-Optical Kerr Effect) [58]. Thus, SMOKE has become the most commonly used surface magnetization measurement technique in laboratories around the world. Because of this technique is a simple, inexpensive and able to determine hysteresis curves very quickly, SMOKE is one of the most used methods for magnetization researches.

2.2. The Domain Theory of Magnetism

Each atom with unpaired electrons has a magnetic moment. These magnetic moments are caused by orbital angular and spin angular momentum of unpaired electrons. In this direction, magnetic behaviour of a material depends on the atomic magnetic interactions with neighboring atoms and also reactions to external magnetic field.

For paramagnetic and diamagnetic materials, direction of each magnetic moment of atom is independent. Thus, the net magnetic moment is zero when there is no external magnetic field. Contrarily, ferromagnetic materials have atomic magnetic dipole moments that attempt to orient parallel to each other. Once the moments are get parallel, the ferromagnetic material will remain magnetized even in the case of outer field is removed. This continuous orientation causing by the strong interaction between adjacent magnetic moments. As a result of this interaction, regions consisting of atoms with magnetic moments in the same direction occur in the ferromagnetic material and these regions are called magnetic domains. [59].

The behaviour and structure of these domains determine the magnetization curve of material, which is also named as hysteresis curve(Figure 2.2). This curve gives the change in the net magnetization of the material, which changes with external magnetic field. When the magnetic field H is applied to a magnetic material that has never been magnetized or demagnetized, magnetization increases from zero to saturation M_s. As the magnetic field decreases, magnetization decreases slowly, following a different path from the first path. When the outer magnetic field is zero, the material still has a

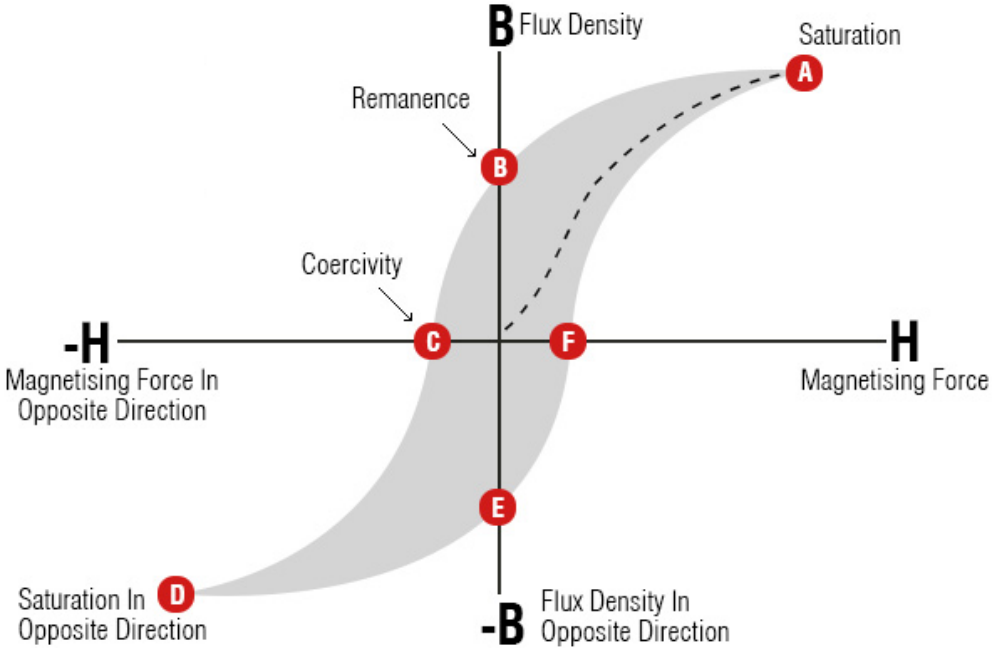

Figure 2.2. Magnetization curve of ferromagnetic material [59].

magnetization value, and this is known as permanent magnetization M_r. To reduce magnetization to zero, magnetic field (coercive field H_c) is applied in reverse direction. Increasing the magnetic field further in the opposite direction, the magnetization reaches saturation again in the direction parallel to the magnetic field as -M_s. Reducing magnetic field back to zero causes the sample to have -M_r magnetization.

2.3. Polarization of Light

An electromagnetic (EM) wave has electrical and magnetic field at the right angles to the direction of propagation. As light is the form of energy emitted in electromagnetic waves, it diffuses in space towards the direction of propagation and magnetic and electric fields perpendicular to each other. It oscillates perpendicular to the direction of propagation of the light beam. The term polarization of an EM wave describes the behaviour of the electric field vector in the EM wave as it propagates in a medium. This propagating wave can be divided into unpolarized and polarized parts. The diffusion of unpolarized light, also called natural light, fluctuates arbitrarily around the direction of propagation, so that in average no direction is favored [60]. However for polarized light, all field components have a fixed phase difference to each other.

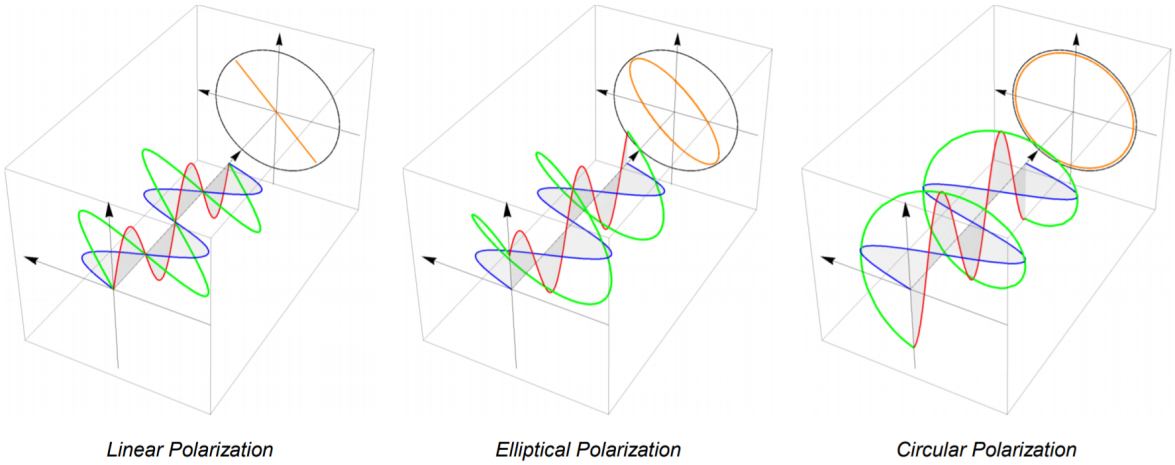

Figure 2.3. Basic states of polarization of light [60].

Each state of polarization (SOP), such as linear, elliptical and circular polarization, can be split into two orthogonal states as s(perpendicular) and p(parallel) shown in Figure 2.3. If the electric field is polarised in the plane of incidence, it is referred to as p-polarised light. Conversely, if the electric field is polarised perpendicular to the plane of incidence, then it is referred to as s-polarised light.

The phase difference between orthogonal states of linear polarized light is 0° or 180° and superposition results in a total electric field that is always oriented in the same direction when viewed in the transverse plane. For the elliptical polarization, the phase difference between the orthogonal states is $> 0°$ and $\leq 90°$. The projection results in an ellipse with a right or left direction of rotation. As a special case of elliptical polarization is circular polarization. For this, the phase difference in between the states is either -90°, which represents the clockwise rotation which corresponds to right-hand circular polarization, or 90° refers left-hand circular polarization state(Figure 2.4). Also, the amplitude of the rotating vector is constant over entire 360° rotation [61].

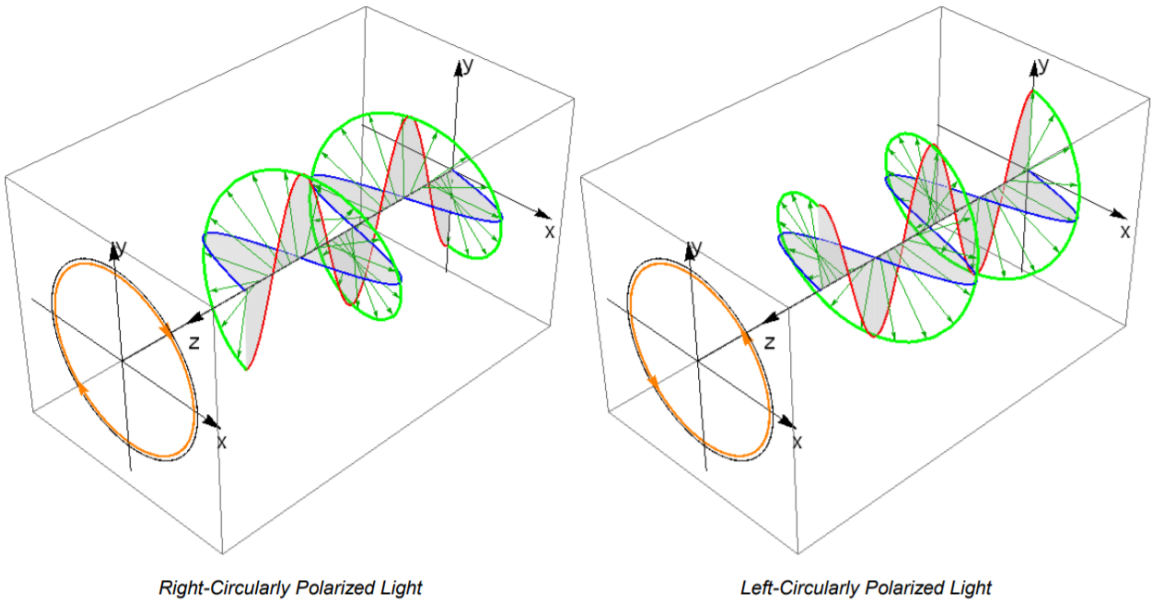

Figure 2.4. Circular polarization states of light [60].

The state of polarization also can be represented by an ellipse as shown in Figure 2.5 [62]. Here, the right hand rule is used to describe the handedness of the polarization state. The handedness of the elliptically polarized light describes the direction of rotation of the E field vector as seen by the observer looking along the -z direction towards the light source.

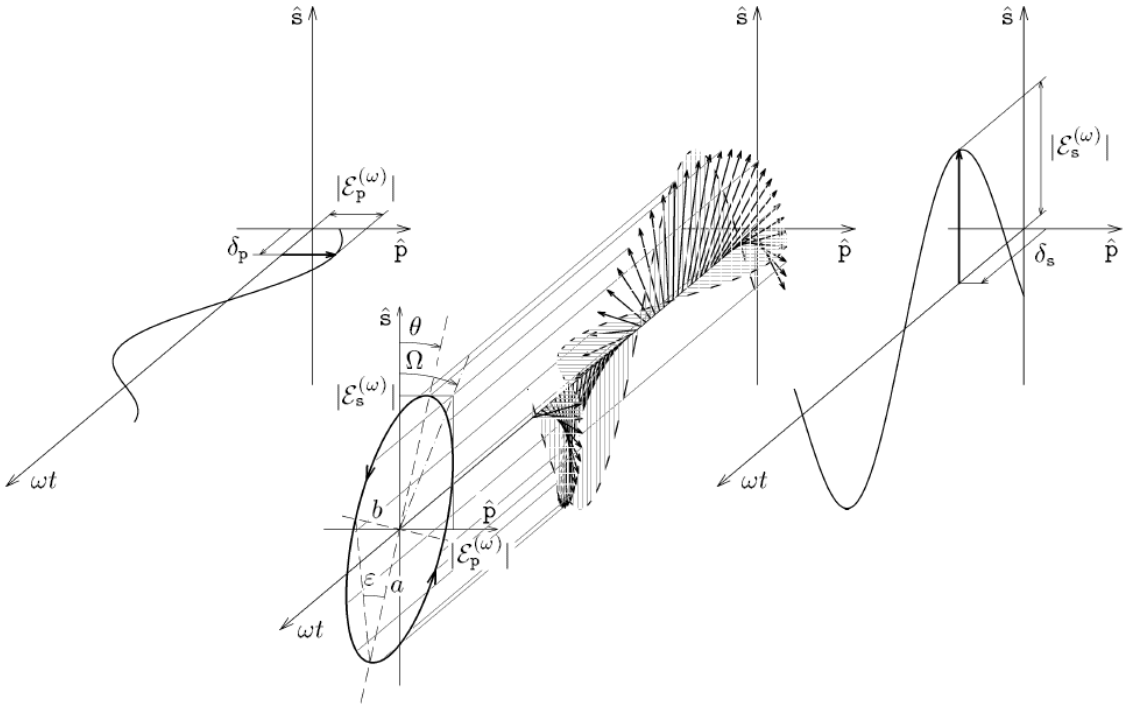

Figure 2.5. Polarization ellipse showing ellipticity (ε) and azimuth (θ) [62].

where $\varepsilon_s^{(w)}$ and $\varepsilon_p^{(w)}$ are modal amplitudes, δ_p and δ_s are phase retardations of s and p polarization states respectively. Here, the azimuth θ is the rotation angle between the principal axis of the polarization ellipse and the s direction. A positive azimuth is referred by counter clockwise rotation of the polarization ellipse. The ellipticity ε is related to the ratio in between minor and major axes of the ellipse as;

$$\varepsilon = \arctan \frac{b}{a} \tag{2.1}$$

Rather than the azimuth, positive ellipticity corresponds to a clock-wise rotation of ellipse.

2.4. Magneto Optical Kerr Effect (MOKE)

MOKE can be described as the change in the polarization state of light, induced by reflection on a sample under a magnetic field. Plane polarised light which is reflected from a metallic surface, is generally elliptically polarised. On the other hand, if the incident light is either p or s polarized, the reflected light still will be plane polarized upon reflection as p or s. This is because the reflecting surface is a plane of symmetry for the system [61]. This symmetry is destroyed when plane polarized light is reflected off a magnetized surface. When the s-polarized light reflected from a magnetic surface, the reflected light has a major s component but additionally a minor p-component. This is because the B field component of electro-magnetic wave is tilted by the effect of magnetic material and as the B and E field components of an EM wave are always orthogonal to each other, the E field component is rotated with a small degree. This causes the light to become elliptically polarised with its major axis rotated from its initial incident polarization plane as shown in Figure 2.6.

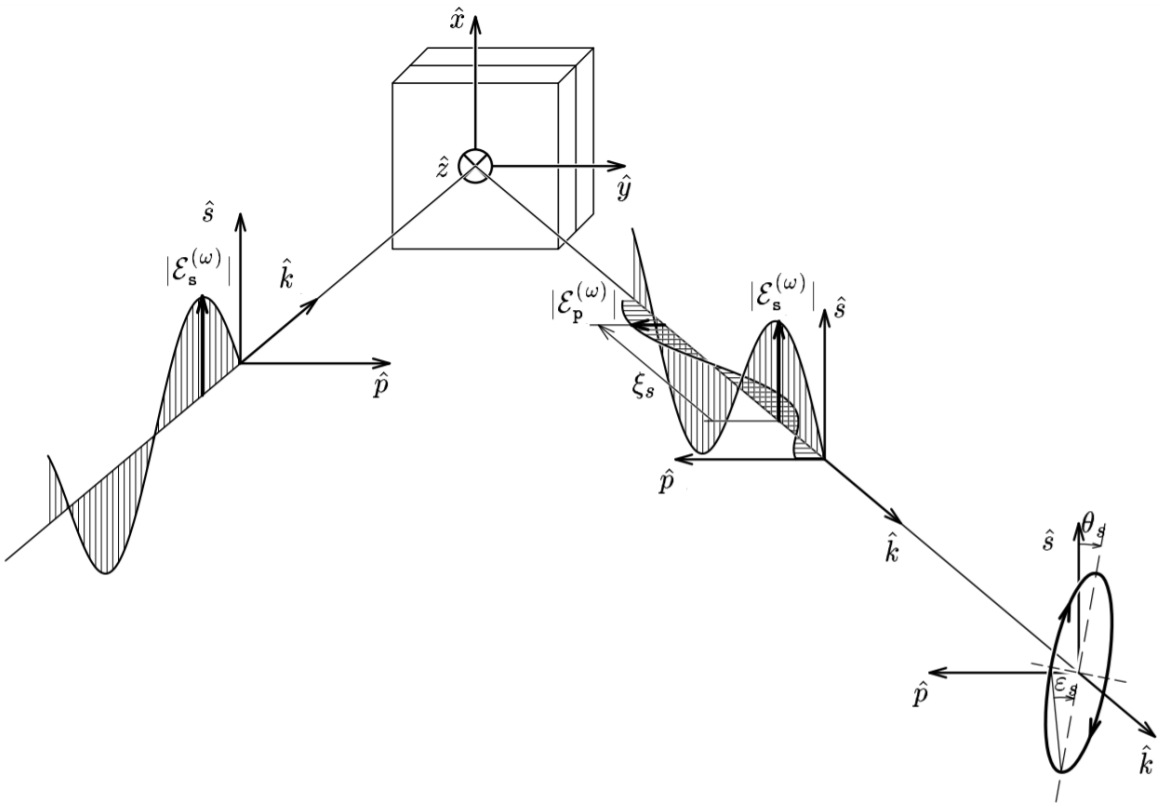

Figure 2.6. The polarization change with respect to MOKE [62].

Also, a similar effect can be observed for p-polarized light. The angular change of the polarized light are explained with two effects as Kerr ellipticity ε_k and Kerr rotation θ_k.

MOKE can be categorized as polar, longitudinal and transverse MOKE, depending on the magneto optical geometries of the sample(Figure2.7). The main determining factor here is the direction of magnetization vector with respect to surface.

2.4.1. Polar MOKE

The magnetization vector is applied perpendicular to the sample and parallel to the incident light as shown in Figure 2.7. The linearly polarized light becomes elliptical polarized after it reflects from magnetized surface proportional to the magnetization.

2.4.2. Longitudinal MOKE

The magnetization vector on the sample is parallel to both the reflection surface and the plane of incidence. The angle of the reflected light is not normal to incident light. As in the Polar MOKE, the linearly polarized incident light becomes elliptically polarized after reflection due to the Zeeman effect.

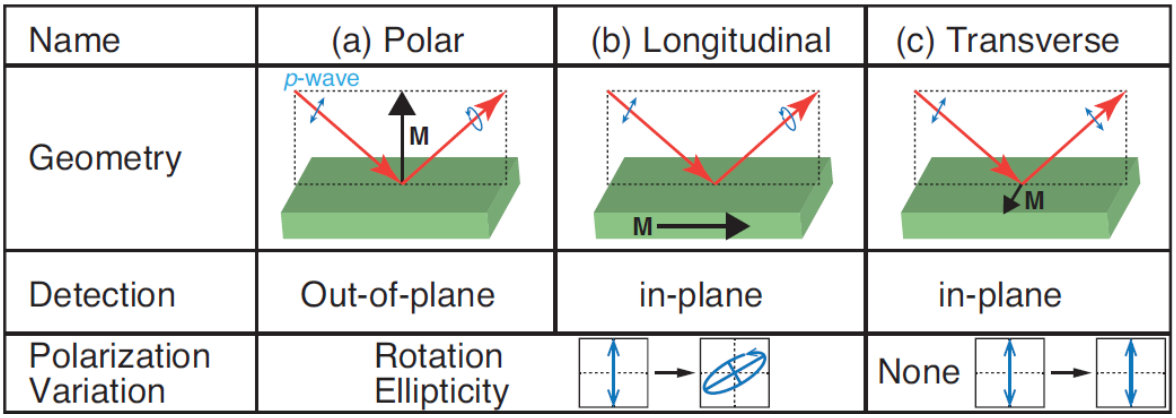

Figure 2.7. Demonstrations of magneto-optic interactions with different magnetization orientations [63].

2.4.3. Transverse MOKE

The magnetization is parallel to the surface but perpendicular to the plane of the incidence. Here, the incident light is also not normal to the reflection surface. In this particular effect, there is no change in the polarization of the incident light. Rather than this, the reflectivity is measured [63].

2.5. Measurement and Characterization of the System

In the light of the explained effect, MOKE is determined as a method to detect the location of the designed micro system. The proof of concept works are realized in air setup and SS430 stainless steel is used, which can be easily magnetized in the laboratory environment and has good reflectivity properties. The setup is customized considering our specifications and needs regarding MOKE setup. The parts used are listed below at Table2.1.

Table 2.1. Material List of MOKE Setup.

	Name	**Catalog Number**
1	Fiber Optical laser source FC/PC	Thorlabs-S1FC780PM
2	Fiber Optical Cable FC/PC	P1-780Y-FC-1
3	Plano Convex Lens Kit	Thorlabs-LSB08
4	Polarized Beam Splitter	Thorlabs-PBS122
5	Beam Splitter	Thorlabs-BS019
6	Rotating Polarizer	Thorlabs FBR-LPNIR
7	Polarimeter	Thorlabs-PAX1000IR1/M
8	Fiber-based polarization beam combiner	Thorlabs-PBC780PM-FC
9	Gaussmeter	Alpha-GM-2

Firstly, a 780nm polarization maintained(PM) laser light coupled with a collimated with two lenses and obtained a minimized beam size. This beam is passed through a linear polarizer. Linearly polarized collimated beam is projected on the

shiny surface of SS430 ferromagnetic material which is located in between two magnets. The reflected light from sample is reached to the polarimeter and polarization change signature with respect to applied magnetic field is measured as its Kerr rotation (azimuth angle) and Kerr ellipticity components.

During the measurement, it was observed that the metal sample, which is located in between magnets, was displaced from the point where it was first positioned, thus the focus point of the reflected light is misaligned. To prevent this, a holder was designed using SolidWorks design software, formed with a 3D printer with a polymer material, and the 1.21 cm^2 size sample is mounted on the handle produced with plastic screws. In addition, one of the magnets that create an electric field is nested on one surface of the holder, and the sensor part of the Gaussmeter is positioned in between the sample and the magnet as presented in Figure 2.8.

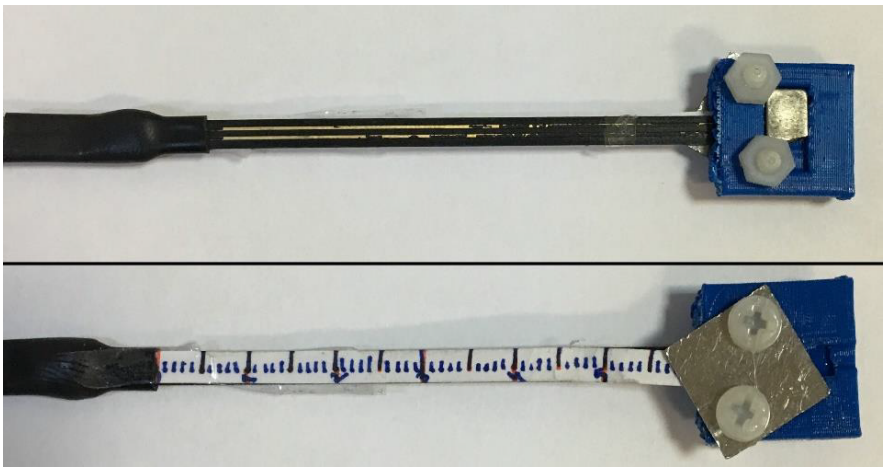

Figure 2.8. Designed holder to fix the sample under applied magnetic field.

Here, the laser beam should be positioned to the most magnetized spot on the sample to take clear measurements. The identification of the point, where the laser beam will be positioned on the magnetized surface, is determined by two measurements. The magnetic flux density created by magnetic field applied by magnets along the surface is mapped with Gaussmeter tip and a ruler is formed along the sensing end. Thus, the surface of the steel sample was profiled and the laser light dropped to the

point where the surface was exposed to the most magnetic field.

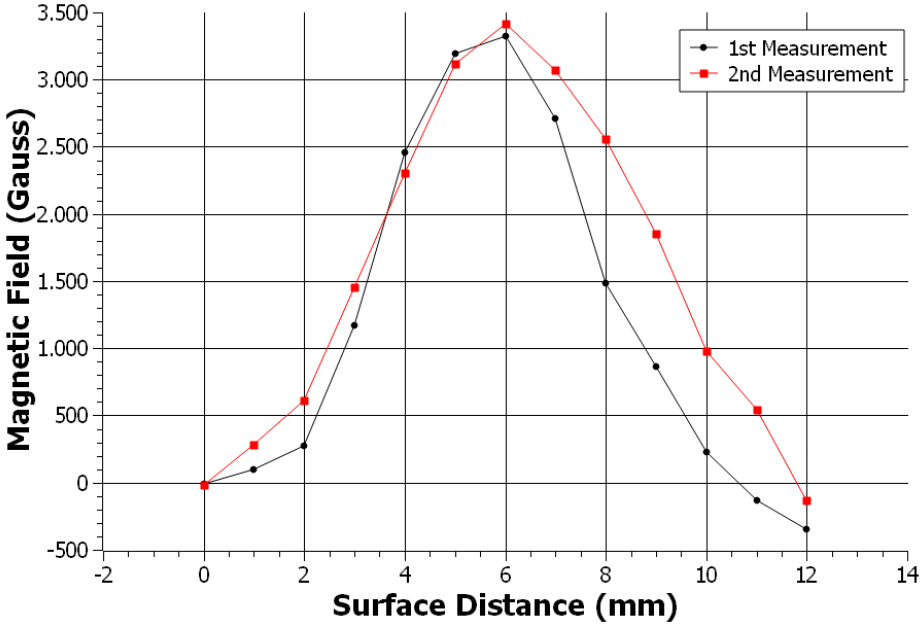

Figure 2.9. Magnetization profile of the SS430 sample with applied magnetic field.

As it can be seen from the graph shown in Figure 2.9, the point where the surface is mostly magnetized has been observed as 6mm away from the edge in both measurements. According to this result, the point where the interaction of the reflected light with the effect of the magnetic field can best be observed is determined. After the point determination, the second pole magnet, is brought closer to and removed from the fixed magnet in a controlled manner.

2.5.1. Calibration

Using the equipment listed in Table 2.1, the system was first calibrated according to the sample used. The main purpose of the calibration is to obtain the mass magnetization (M-H) curve created on the sample due to the effect of magnetic flux density change from samples B-H curve (APPENDIX C). To achieve this, used method and calculations are presented below.

As it is known, magnetic field strength H is proportional to magnetic flux density B. The main formulations to correspond the relation in these two parameters are:

$$B = \mu_0(H + M) \tag{2.2}$$

in SI units where M is magnetization, μ_0 is magnetic permeability and its value is $4\pi \times 10^{-7}$ V·s/(A·m) and both H and M has units of A/m. Secondly;

$$B = H + 4\pi M \tag{2.3}$$

in Gaussian Units where the unit of B is *Gauss*, unit of H is *Oersted* and unit of M is emu/cm^3.

Firstly, the sample was positioned in the middle of two magnets as Longitudinal MOKE configuration and DC magnetic field in the interval from 1.3 to 10 Gauss was applied on it. Due to this external field, a controlled variable magnetic field between 103 and 750 A/m applied on the sample. Thus, created longitudinal magnetization on the sample surface changes the flux density of the sample. On the other hand,

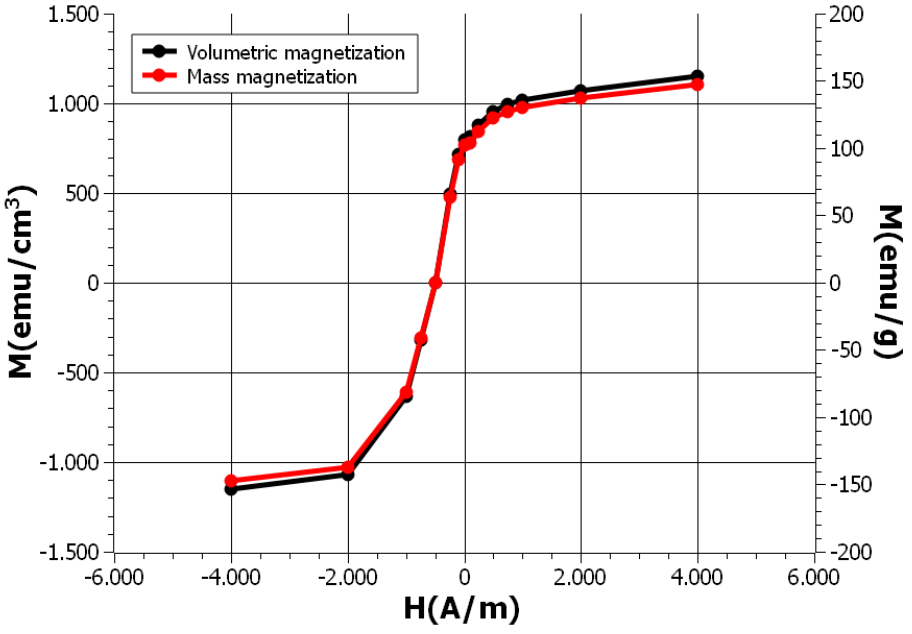

Figure 2.10. Volumetric magnetization curve of SS430 sample.

net magnetization M on the sample is calculated with using Equation 2.3. As a first step, the graph of M (emu/cm^3) - H (A/m) is obtained as Figure 2.10. In order to obtain the mass magnetization M (emu/g) - H (A/m) curve, the transformation of the magnetization unit from volume magnetization to mass magnetization is achieved. For this, it is sufficient to divide the unit emu/cm^3 by the bulk density of the sample (d=7.8 g/cm^3 for the SS430 steel sample). Thus, the M-H graph is obtained for the used sample is also presented in Figure 2.10.

Since the main aim of the tracking method will be in MRI, the controllable magnetization change will be obtained by MRI gradient field strength. Briefly, the gradient components create a linear variation in a magnetic field intensity of small values. In addition to the main magnetic field B_0 i.e 1.5 T, the gradient fields are also applying in a same direction but focalized to a small area generally as 30cm^3 and they are adding to B_0. The main function of the gradient fields are the spacial encoding of the MRI for imaging. However, due to the gradients can cause 30 mT/meter change on main field, the Kerr effect is used based on the changes in the gradient field strength to track the position of catheter. To calculate the external H magnetic field on the sample which is applying by the gradient' s magnetic flux intensity B, the fundamental Equation 2.2 should be used where M is zero, B is 30 mT/m for gradients and μ_0 for air is 1.256×10^{-6} H/m. Hence, the applied H field to the sample is calculated as 23931 A/m for meter, as such, 23.931 A/mm.

2.6. Experimental Setups

In this part of the thesis, there will be presented three different setups with different materials.

2.6.1. Air Optics Setup with SS430

Firstly, the light emitted from the fiber optic laser source is aligned to the sample with the use of a fiber cable. In order to reduce the attenuation of the light beam, a 35 mm focal length convex lens is used as collimator and the beam width of the light

is kept constant along the path.

The fixed beam is passed through the polarized beam splitter, and the polarization fixed light obtained. Light beam is then reflected from the most magnetized point considering Figure 2.9.

At this point, the reflection angle of light plays an important role since the longitudinal MOKE is used. According to literature research, it is determined that the Kerr effect can be observed most effectively by reflecting from sample with 55° angle [64] as shown in Figure 2.11.

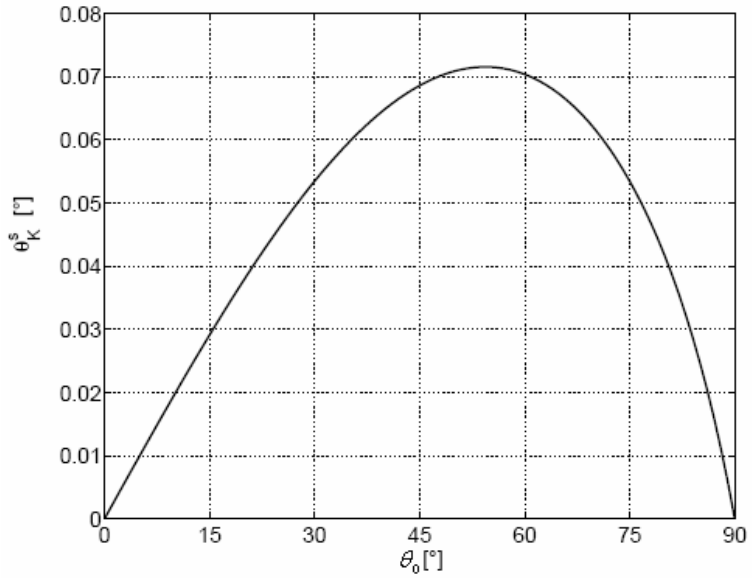

Figure 2.11. Graph of Kerr rotation as a function of incident angle θ_0 [64].

Accordingly, the angle in between the light and sample is aimed to be as close as possible to 55° in the experimental setup. Afterwards, the beam reflected on the sample is focused on the detector part of the polarimeter with a diameter of 200 μm with using 25.4 mm focal length convex lens (Figure 2.12).

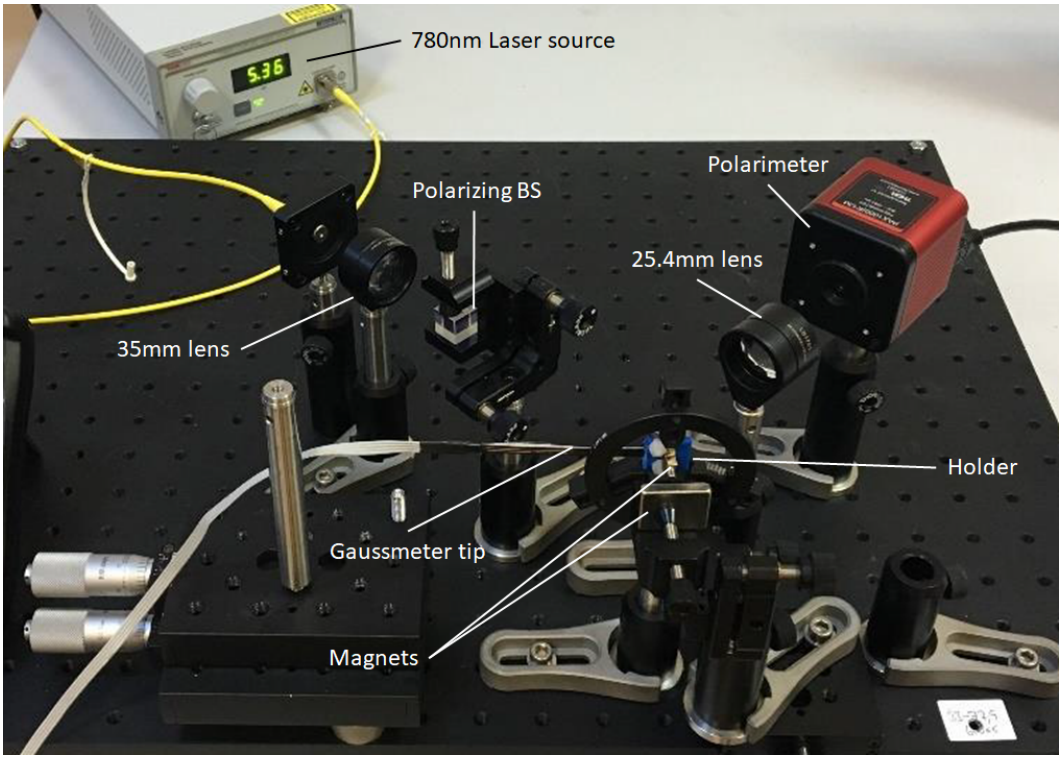

Figure 2.12. Air optics setup with SS430 sample.

At this step, the polarization state of the reflected light is measured with Thorlabs PAX1000IR1/M polarimeter. Among different methods, device uses the rotating $\lambda/4$ waveplate technique (Figure 2.13).

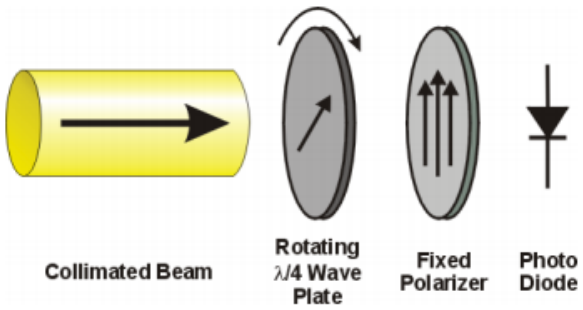

Figure 2.13. Rotating waveplate technique [60].

The measurement sensor consist of a rotating true zero order quarter waveplate (QWP), a fixed polarizer and a photodiode. The polarization of the incoming collimated beam is modulated by the rotating QWP as circular polarization state that enters the linear

polarizer depends on the actual rotation angle of the waveplate. The fixed linear polarizer, which is using as an analyzer, transforms the polarization modulation into an amplitude modulation of the light power that enters the photodiode. [60]. The modulated beam reflected on the photodiode is measured based on Malus' Law. It explains dependence of the intensity of polarized light with the initial intensity I_0 passing through the analyzer filter and the θ angle of rotation of the polarization and it can be calculated with the following equation:

$$I = I_0 \cos^2 \theta \tag{2.4}$$

In the setup shown above, it is assumed that the electric field of focused light on the polarimeter is E_0. As the intensity of light corresponds to the square of the electric field strength, the electrical field component of the light passed through the analyzer is as follows:

$$E = E_0 \cos \theta \tag{2.5}$$

which gives the amount of electrical field that can pass through the analyzer.

In the light of these information, the experimental setup shows that an external magnetic field, applied on an electromagnetic wave, can change the direction of electrical field and accordingly, the polarization of the wave. With the usage of the N and S pole magnets, the steel sample on which the beam is reflected, is magnetized. Due to the external magnetic field effects in between 103 A/m and 750 A/m, the mass magnetization of the sample is changed in between 104.5 emu/g and 127.44 emu/g. This change in magnetization caused the change in azimuth degree and correspondingly, the power of the light beam reached to the photodiode. The changes of the azimuth degree and power are measured with polarimeter in 50Hz sample rate and 1 (1024 pts FFT) operating mode which means the data for calculation are collected per 1 revolution of the waveplate (number of basic periods=1) and the FFT is carried out on 1024 points within this half turn. Measurement results of change in degree and power are presented in Figure 2.14 and Figure 2.15 respectively.

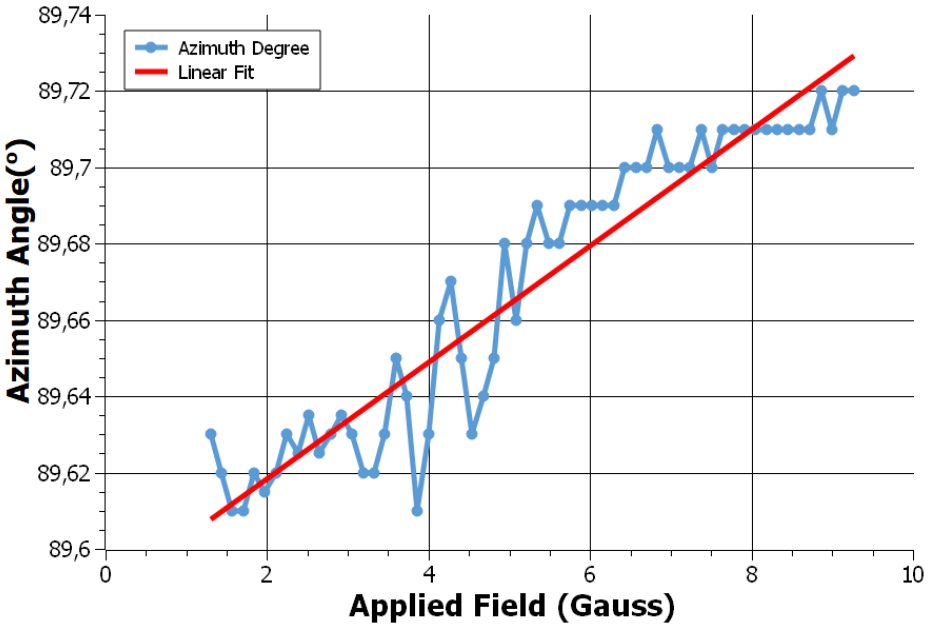

Figure 2.14. Azimuth angle change with respect to external magnetic field.

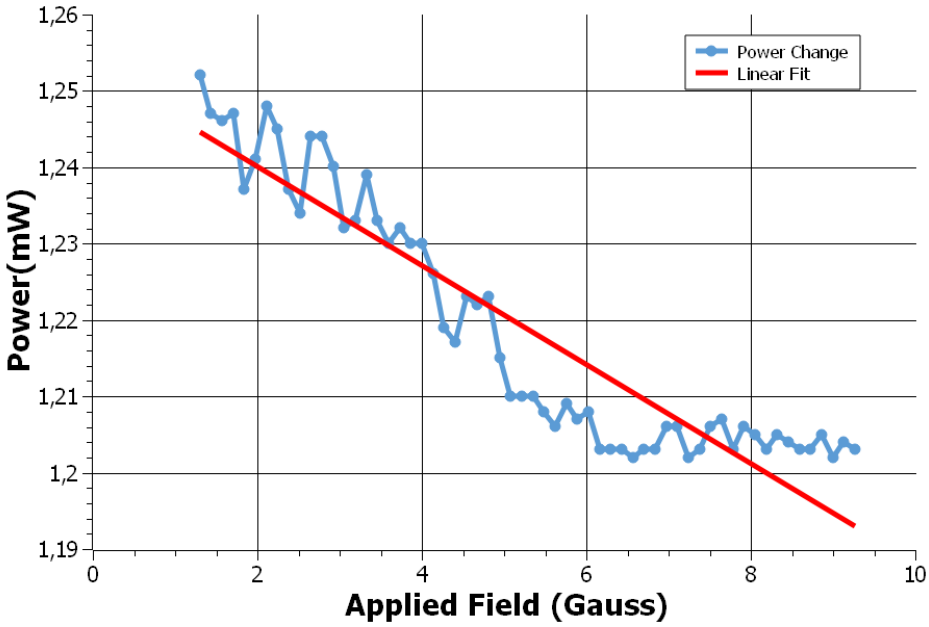

Figure 2.15. Power change with respect to external magnetic field.

As it can be seen in figures, the external magnetic field has an effect on the power of the reflected light from the magnetized ferromagnetic sample and accordingly polarization state change has been observed. From the Figure 2.14, the change in azimuthal degree is 0.12° depending on the change in H field for 647 A/m (from 1.3 Gauss to 9.4 Gauss). As the minimum detectable degree change by detector is 0.01°, the minimum detectable H field change (ΔH) corresponds to 54 A/m H field change from this setup. Thus, as the gradient values change in 23.931 A/m per mm, it can be said that, the change can be detectable in 2.25mm precision with this optical air setup's azimuthal degree. In parallel with this, from the Figure 2.15, it can be seen that the change in power is 0.05 mW. As the power change sensitivity of the device is 0.001 mW, the minimum ΔH is calculated as 12.94 A/m which corresponds 0.54 mm precision.

2.6.2. Fiber Optic Setup with SS430

Following the observation of the Magneto Optical Kerr Effect above and the calibration mechanism created with the equipment used, the observed effect is transferred to the wired system in order to make the system suitable for use in intravascular operations as predicted. Accordingly, the most important feature of the equipment listed in Table 2.1 that they are designed to prevent the change of polarization statement from external effects. In this context, the fiber optic cable and the light source is chosen as polarization maintaining components. In the setup, the light coming from the laser source, whose slow axis is fixed as vertically, and Thorlabs PBC780PM-FC, fixed polarized beam combiner / splitter cable is used.

Since the laser source rays p-polarized light, only the first and third ports of the cable are used. Firstly, the beam transmitted by the cable is collected with a 25.4mm focal length convex lens. Then a mirror is used to reflect this beam onto the SS430 sample at 55°, which is the angle value at which Kerr effect can be observed most effectively.

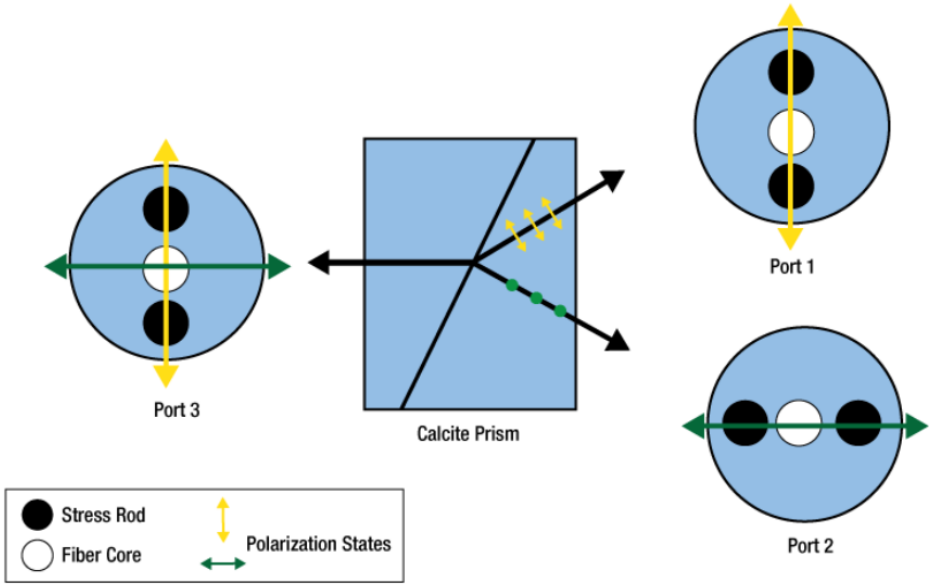

Figure 2.16. Working principle of polarization maintainig cable.

The reflected beam from SS430 sample is reached to the second mirror and from there, light beam reached to the polarimeter as shown in Figure 2.17. Measured azimuth and power change data in 1 (1024 pts FFT) operating mode are presented in Figure 2.18 and Figure 2.19 respectively.

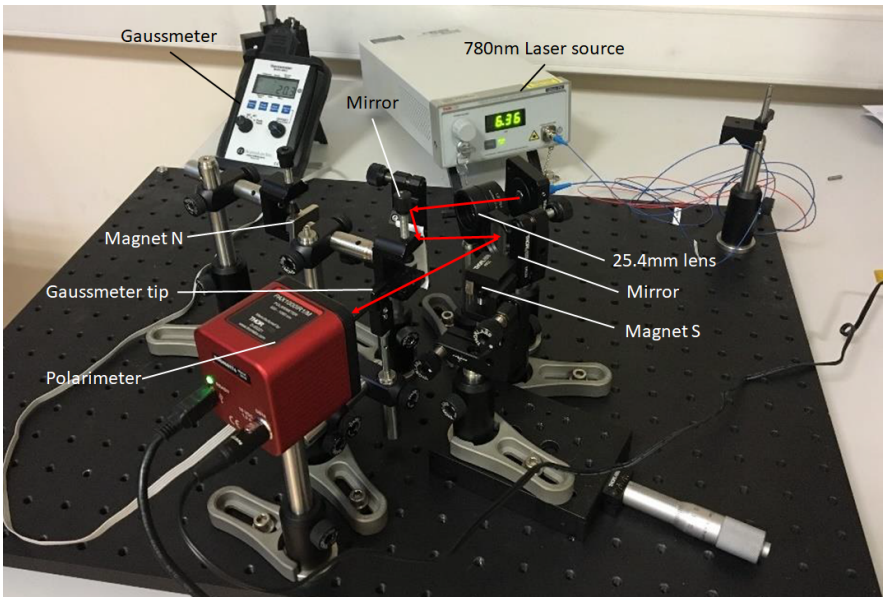

Figure 2.17. Magneto Optical Kerr Effect measurement setup with PM cable.

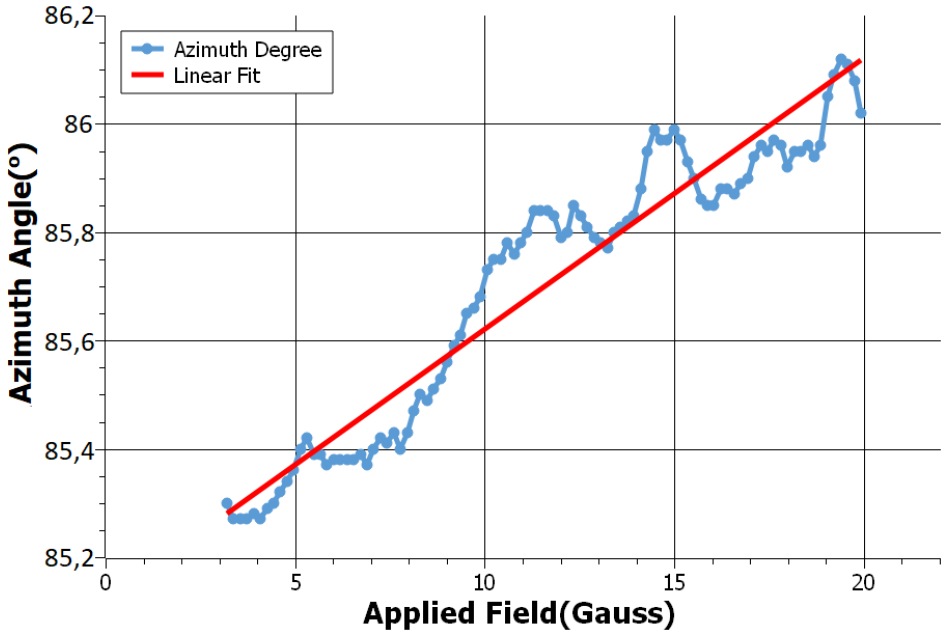

Figure 2.18. Azimuth angle change caused by external magnetic field effect.

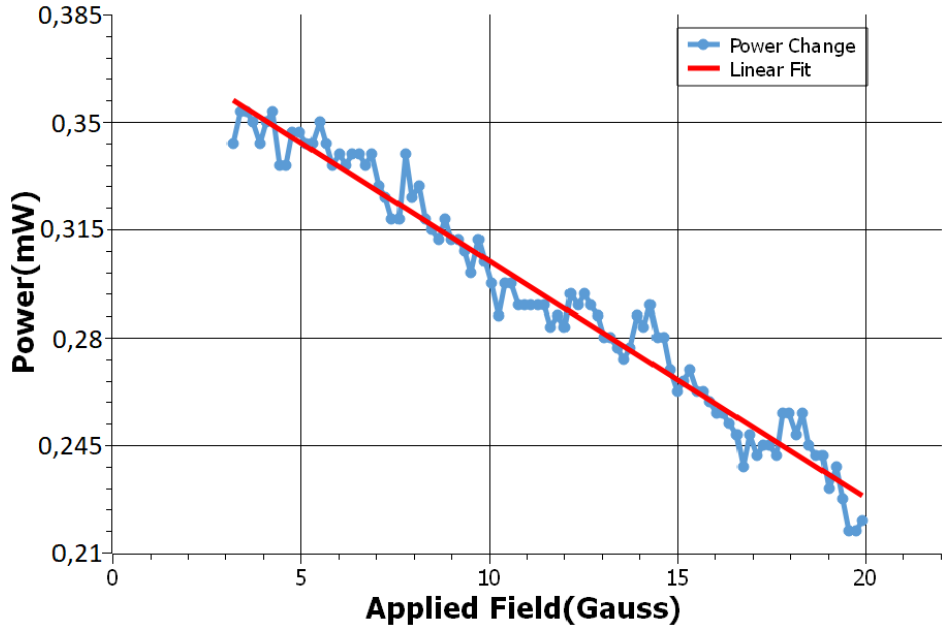

Figure 2.19. Power change measured by the polarimeter as a result of the applied magnetic field.

As it is presented in figures, Polar MOKE configuration is installed for the cable setup. The azimuth degree and power ratio changes are observed. According to Figure 2.18 and Figure 2.19, the external B field creates 1619 A/m H field change on the steel sample. With the effect of this change, the azimuth degree changed for 0.8°. From here, the minimum detectable ΔH is calculated as 23.13 A/m. According to this, the catheter tracking is able to do for 0.967 mm precision with azimuth degree change of fiber optical setup. Also, the power change is observed as 0.142 mW in this interval of H field change. As the minimum detectable power change is 0.001 mW by the polarimeter, the minimum detectable ΔH is calculated as 11.4 A/m by the system. Correspondingly, from the power change graph, it is observed that the precision of catheter tracking is calculated as 0.475 mm. As a result, it can be said that the polarization state is affected by the external magnetic field as Kerr effect.

2.6.3. Air Setup with Fe_2O_3

As the main purpose of the system is to track the localization data of the sensors in MRI, the use of materials with higher saturation coefficients as a sample becomes more compatible. For this reason, a paramagnetic material is determined to meet the system requirements. Therefore, iron(III)oxide (Fe_2O_3), one of the available materials in our clean room, is chosen due to the advantages of being convenient to work in MRI with their high saturation magnetization value up to ±1.5 T, quickly obtainable, inexpensive and easy to use. For this reason, thin film Fe_2O_3 is coated on a borosilicate glass via sputtering method.

After the proof of concept setups and calibration works are done with SS430 sample, the air setup is installed with (Fe_2O_3).Firstly, a light beam is collimated as 200μm with a 50mm convex lens. Then light beam passed through Thorlabs FBR-LPNIR rotating linear polarizer module. Obtained linearly polarized light is reflected from the sample, which is magnetized as Longitudinal MOKE configuration, and reached to the polarimeter as shown in Figure 2.20. At that point, the external magnetic field is applied in between 0 and 285 Gauss. This interval corresponds the magnetization change in between 0 to 15 emu/g on M-H hysteresis curve.

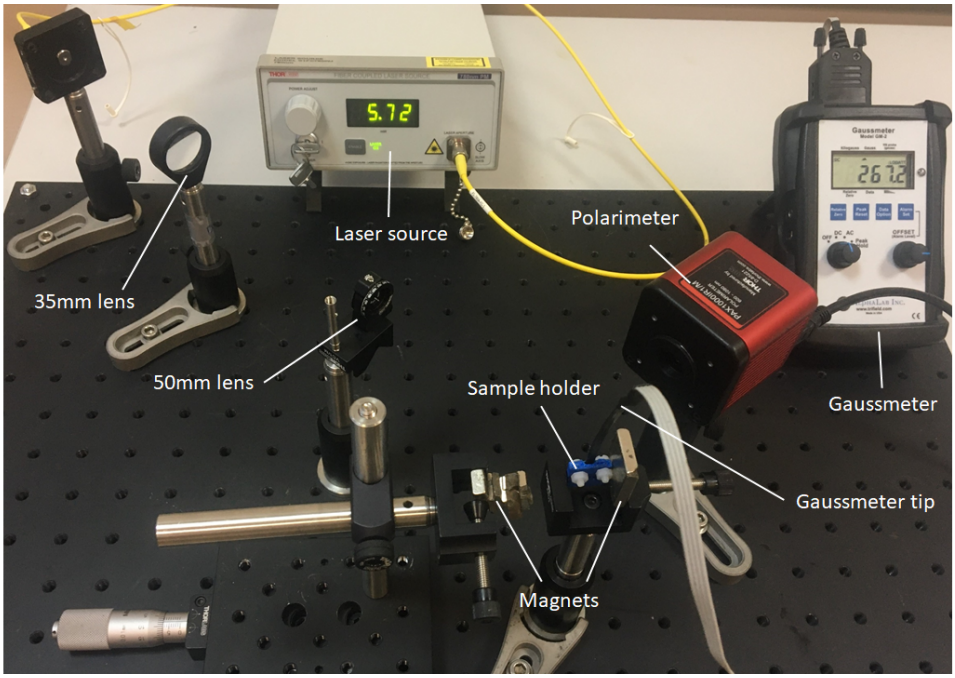

Figure 2.20. The air setup to observe the MOKE with Fe_2O_3 sample.

Besides azimuth and power change data, the ellipticity change is observed for Fe_2O_3 sample with using PAX1000IR/M in 1 (1024 pts FFT) operating mode and these datasets are presented in Figure 2.21, Figure 2.22, and Figure 2.23 below.

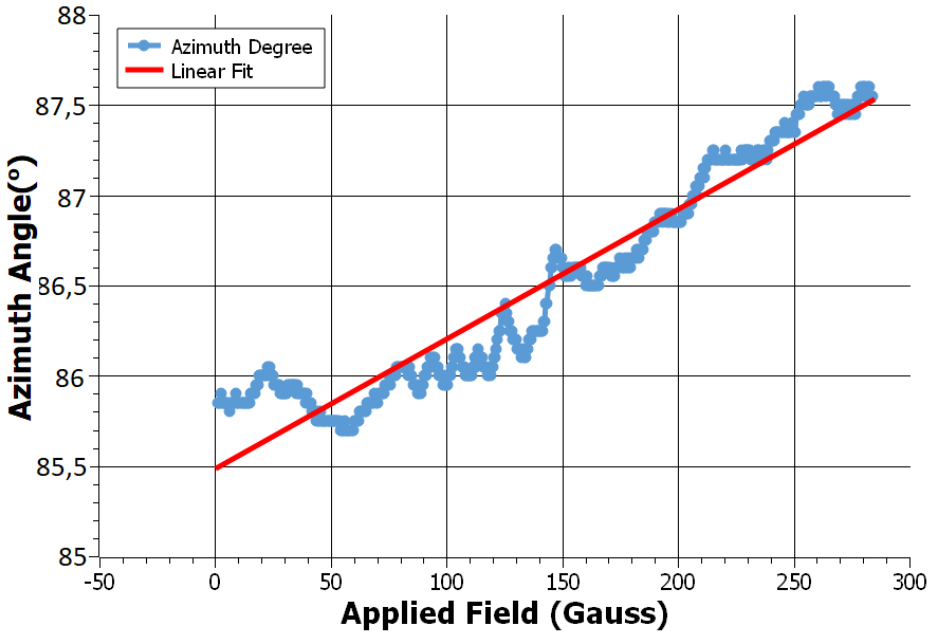

Figure 2.21. The azimuth angle change of the light with Fe_2O_3 sample.

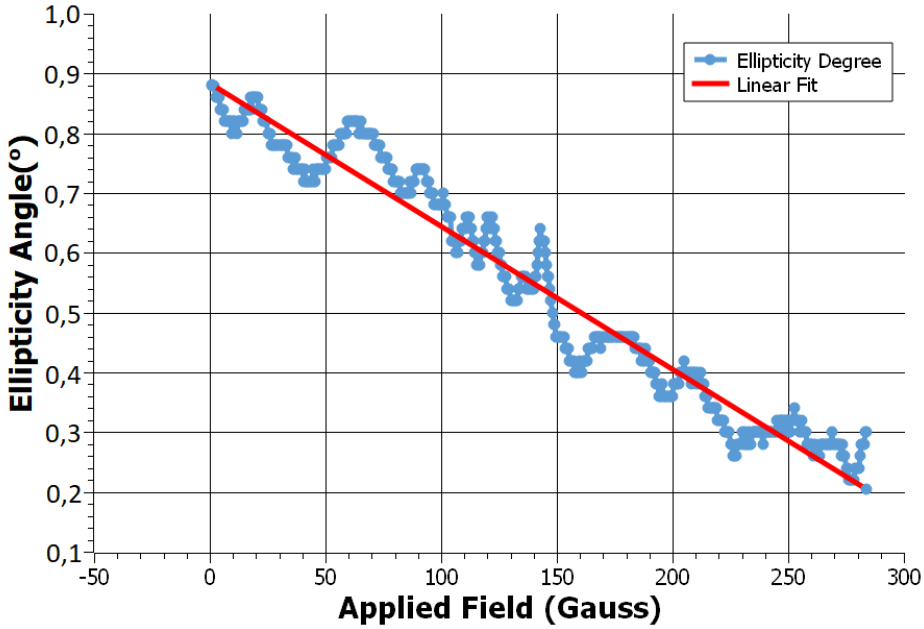

Figure 2.22. The ellipticity angle change of the light with Fe_2O_3 sample.

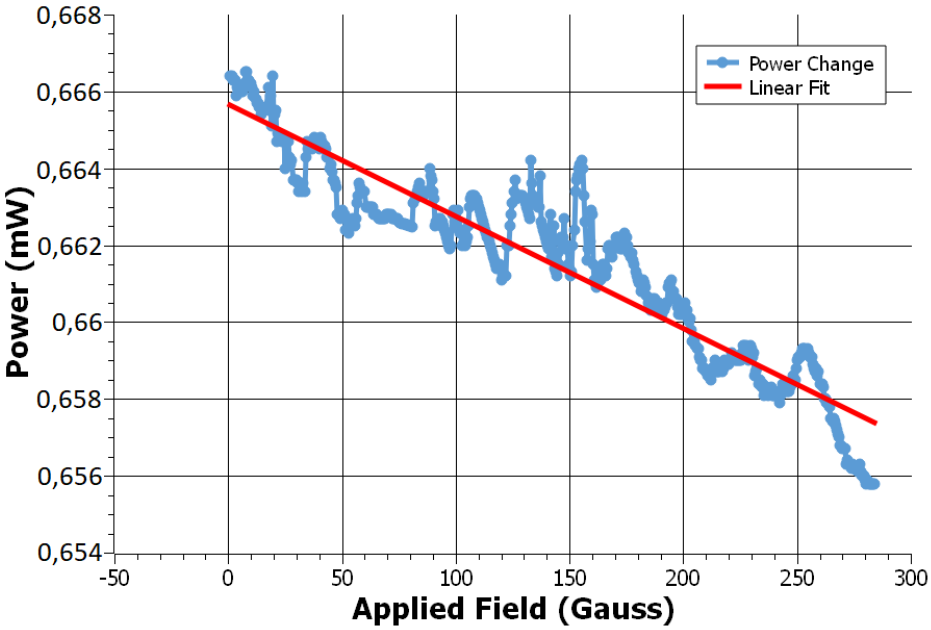

Figure 2.23. The power change of the light with Fe_2O_3 sample.

According to the figures shown above, it can be seen that Kerr effect caused on azimuth and elliptical degree changes of the light polarization and also on the power of the beam. The change in the external magnetic field from 0 to 285 Gauss creates 22335.6 A/m H field change on the sample. From Figure 2.21, this change created 2.1° change on azimuth degree in total which corresponds to minimum detectable H field change ΔH as 106.36 A/m. So that, the precision of the catheter tracking is calculated as 4.44 mm with measured azimuth degree change.

On the other hand, rather than the SS430 setups, an ellipticity change is observed for Fe_2O_3 sample. From figure 2.22, it is observed that the same external H field change caused 0.87° change on the ellipticity degree. As the minimum detectable degree change for ellipticity is 0.01°, the minimum detectable ΔH is obtained as 254.86 A/m which corresponds 10.65 mm precision while the tracking the catheter.

However, unlike the SS430 setup results, a detectable sensitivity value could not be observed in Fe_2O_3 air optics setup as the observed power change occurs in a very small range.

As a result, different setups are realized with different configurations. First two setups are the way of conceptual works to observe the magneto optical Kerr effect with a ferromagnetic material SS430, and then, a more suitable paramagnetic material Fe_2O_3 is used to test the observation of the Magneto Optical Kerr Effect for the higher order external magnetic fields. Based on the graphs shown above, the light beam, reflected from the magnetized material with special angle, shows some alterations in polarization state according to magnetization of the sample. These obtained data sets can be positioned on a linear fit curve and it is possible to observe the change of Kerr effect parameters.

According to taken measurements with different configurations, it can be seen that the minimum detectable localization change is 0.475 mm by observing the power change of fiber optical setup. The azimuth degree change is also gives better result than the air optical setups graphs. Also, although the applied magnetic field could go

further for Fe_2O_3 coated sample, the ratio of the precision and minimum detectable ΔH are reducing. For this setup, the elliptical degree change is observed on the contrary of the first two setups, however, the observed power change does presents meaningful results to track the localization precisely.

Thus, the effect of the Magneto-Optical Kerr Effect on the polarization change has been demonstrated, depending on the change of the azimuth angle, ellipticity angle and power change.

As future work, considering that the light will send to tip of the catheter and reflected back from the same line on fiber, and there should be some specific angle in between the incident and reflected light to observe Kerr effect, this part of the system will use two triangles which are coated with Fe_2O_3 thin film. As a demonstration, it is planned that incoming light beam is going to reflect from the first triangles hypotenuse and in the same way, beam is gonna reflect from the second triangles hypotenuse and it is going to couple with fiber again. Coupled light will reach to the polarimeter via PM fiber cable and according to magnetic field change in MRI, the optical position tracking will be possible.

3. TEMPERATURE SENSING

Conventional temperature measuring devices are available in different types, such as thermistors, thermocouples or resistance temperature detectors, according to their applications. However, because of their requirement of electrically conducting connections, they cause MRI signal interferences and signal voids. To overcome this problem, the fiber-optical temperature sensors are preferred, as they are nonmagnetic and they do not lead RF interferences and heating during MR imaging. Fiber optical temperature sensors (FOPS) are also based on different measurement methods. They can be mainly listed as microfiber loop resonance, Brillouin scattering, fluorescence lifetime measurements, Fabry-Perot interferometry, Fiber Bragg grating and optical translucence of semiconductor measurement methods [65, 66]. In this project, semiconductor based method is chosen because of its high temperature sensitivity and thermal stability as well as very good broad temperature linearity.

3.1. Operation Principle of Semiconductor Based Temperature Sensor

Semiconductor based fiber optical temperature sensor systems are consist of two major branches as interrogator and sensor parts as shown in Figure 3.1 [67]. A light from interrogator part is guided to the semiconductor via fiber cable and impinges on crystal. The reflected light is collected and exposured on a spectrometer by fiber.

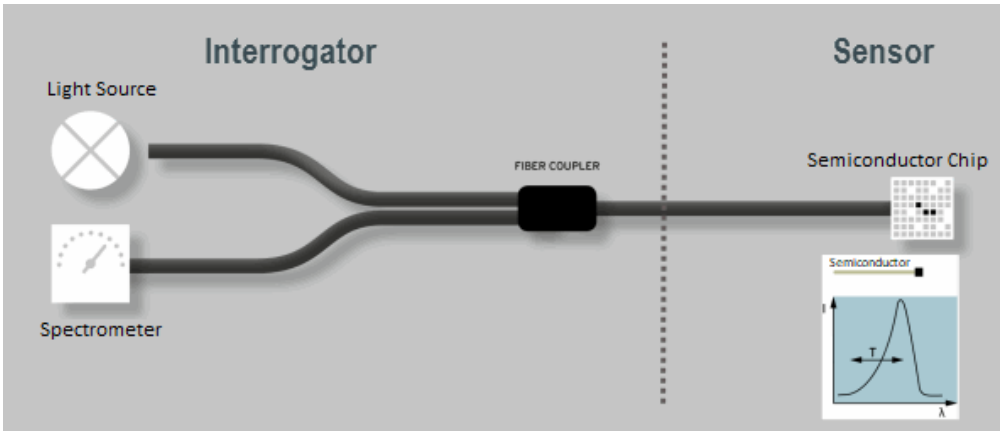

Figure 3.1. Temperature sensing system [67].

At sensing part, the working principle depends on absorption property of semiconductor. The absortion coefficient of a material explains that how far a light of a particular wavelength can penetrate before it is absorbed. This coefficient depends on the material [68] and also on the wavelength of the exposured light on crystal. The reason why semiconductors are using mainly to see this effect is, they have a sharp edge in their absorption coefficient as shown in Figure 3.2 for different semiconductors. Accordingly, gallium arsenide (GaAs) is chosen as a semiconductor in the sensing part.

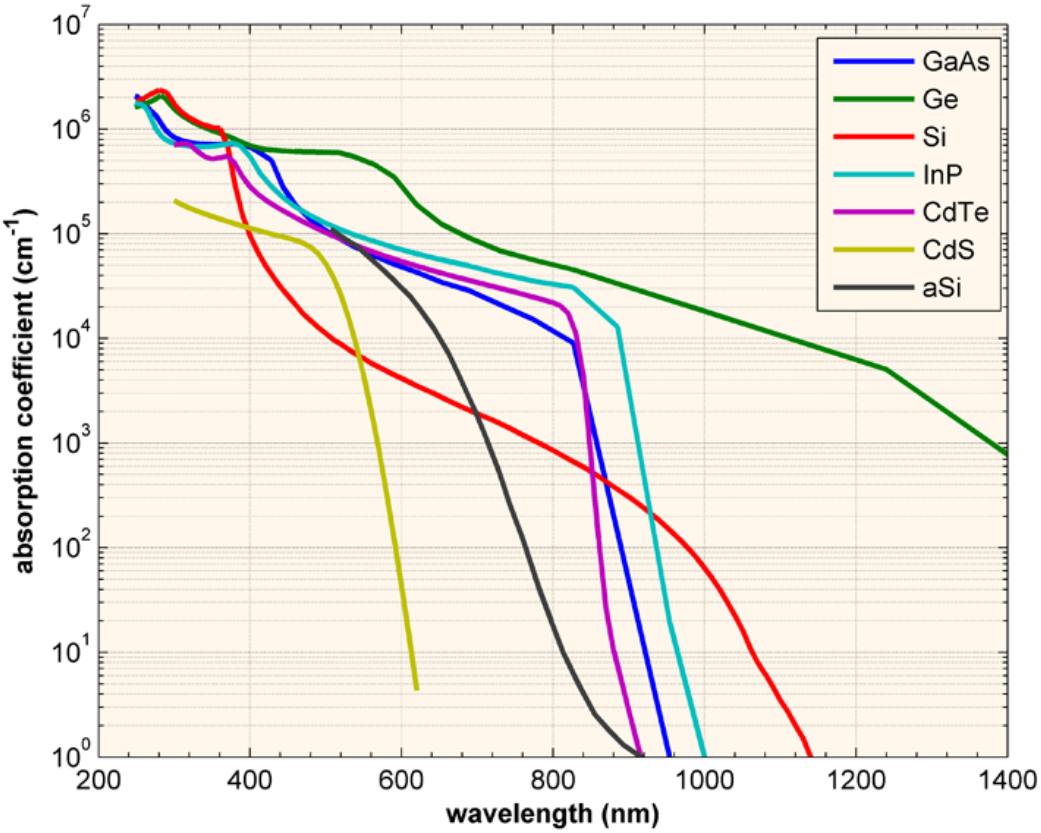

Figure 3.2. Absorption coefficient of different semiconductors [68].

The temperature change in the medium effects on the GaAs crystal in very predictable and well known ways. Mainly, as the crystal's temperature varies according to environment, its transmission spectrum shifts to higher or lower wavelengths. At any temperature value and specific wavelength of the light, crystal's transmission spectrum jumps from 0% to 100%. This jump is named as absorption shift as in Figure 3.3 [69].

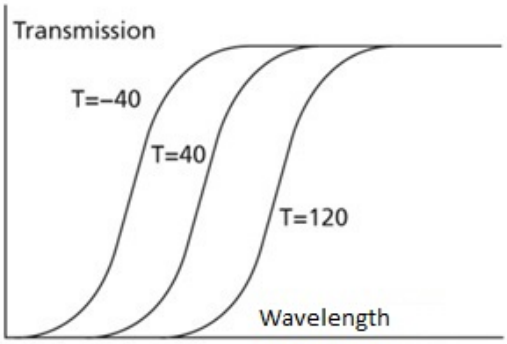

Figure 3.3. Temperature sensing transmission shift [69].

To understand how the absorption shift occurs, it is necessary to explain the variation in the semiconductor's energy band gap. The shift is the result of the impact of changes in the semiconductor's energy band gap. Electrons in isolated atoms have their own energy values at certain point. Putting isolated atoms together in a crystal creates different ranges of energy levels as bands for electrons, rather than restricted ones. These bands are called as valance and conduction bands as seen in Figure 3.4 [70].

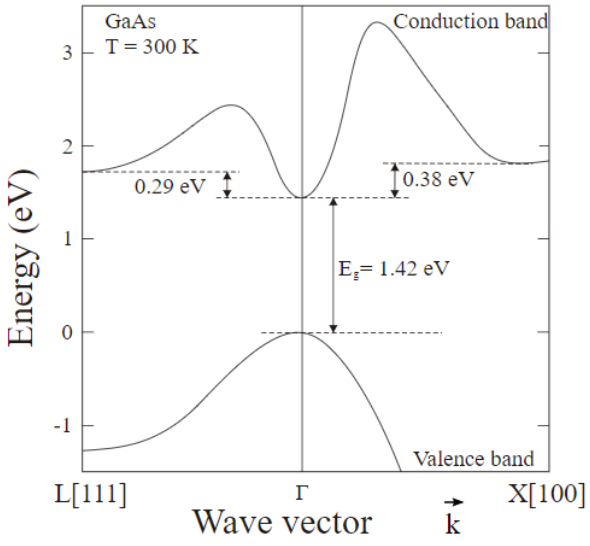

Figure 3.4. Band structure of GaAs semiconductor [70].

The band gap refers to the energy required to bump the electrons in the material from a relaxed, steady state into an excited state. As more energy enters the crystal

in the form of heat, the band gap narrows, and less additional energy is required to activate an electron. Photons entering the crystal actually carry the energy that drives the electrons. If a photon carries enough energy to pass an electron to the upper energy level through the gap, that photon is absorbed. Otherwise, photon will be transmitted or reflected.

At some specific wavelength of incident light, the semiconductor acts as a transparent material and transmits the light. In this wavelength, which is known as optical absorption edge wavelength or also called as optical cut-off wavelength (λ_c), depends on the band gap energy of the semiconductor material. At room temperature, the unique cut-off wavelength can be calculated as;

$$\lambda_c = \frac{\hbar c}{E_g} \tag{3.1}$$

where E_g implies the band gap of the semiconductor equals 1.421 eV at room temperature as seen in Figure 3.4, $\hbar$ is the plank constant equals 6.62×10^{-34} J·s, c is the speed of the light in vacuum as 3×10^8 m/s and also 1 eV is 1.6×10^{-19} J as a conversion factor gives cut-off wavelength as 873 nm for undoped GaAs which is in the near infrared (NIR) region of the spectrum.

The shorter the photon wavelength, the more energy it carries. Since the band gap narrows as the temperature of the semiconductor crystal increases, the photon needs less energy to bypass the gap, the longer wavelength photons with less energy are absorbed by the band. At this point, since the absorption rate of the semiconductor, whose temperature increases, will increase, the amount of light transmitted on the crystal will also decrease. As a result, observing the wavelength depended on absorption shift gives the change of the crystalline temperature. The temperature dependence of semiconductor band gap formula is given in Equation 3.2 as follows:

$$E_g(T) = E_g(0) - \frac{\alpha T^2}{T + \beta} \tag{3.2}$$

where $E_g(0)$ is band gap energy at 0 °K is 1.519 eV, direct energy gap fitting constants α is 5.41 $\times$ 10^{-4} eV/°K , and Debye temperature β is 204 °K for GaAs. The plotted graph of the resulting bandgap versus temperature is shown in the Figure 3.5.

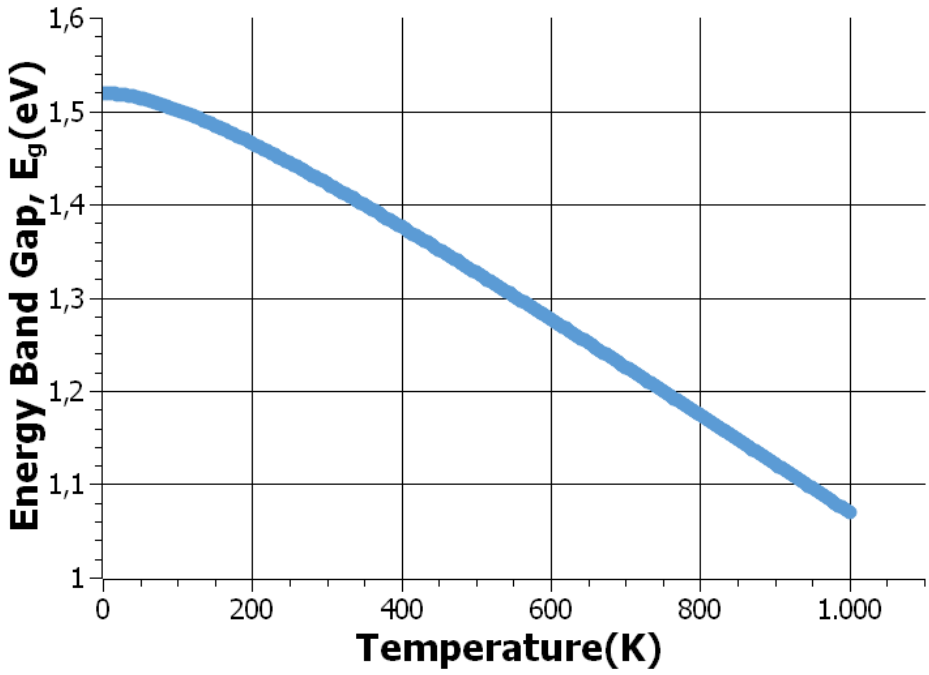

Figure 3.5. Temperature dependence of the energy bandgap of GaAs.

According to calculations of this dataset, the energy band gap values show an alteration in between 1.426 eV and 1.413 eV aimed temperature range, which is the range of 19 °C - 48 °C. Implying this band gap values to the Equation 3.1 gives the change of cut-off wavelength from 869.5 nm to 877.5 nm.

3.2. Optical Characterization Theory

To obtain equations for absorption and transmission, it is necessary to analyze the basis light properties and concepts. The interaction of light with semiconductor basically can be examined as four base components: an incident, a reflected, a transmitted and an absorbed. As the law of conversation of energy,

$$R + T + A = 1 \tag{3.3}$$

where R is reflectance, T is transmittance and A is absorbance. On the right hand side of the equation, the incident light energy is shown as 1.

To begin with, reflectance is defined in terms of the index of refraction of the media. If the media, surrounded by air, has an index of n, then the reflectance can be written as,

$$R = \left| \frac{n - n_{air}}{n + n_{air}} \right|^2 \tag{3.4}$$

where the refraction index $n_{air} \approx 1$.

According to Beer's Law, after some of the incident light reflected from the surface, light propagates through z direction with respect to thickness of the GaAs sample material as,

$$I(z) = I_0 e^{-\alpha z} \tag{3.5}$$

where α is the absorption coefficient and I_0 is the intensity at the incident surface. The attenuation of the incident light on this path is shown in Figure 3.6.

Here, the absorption coefficient can be defined as the function of the absorbed intensity during length in the material as,

$$\alpha = -\frac{1}{I(z)} \frac{dI}{dz}. \tag{3.6}$$

In order to expand these equations for transmission, it is necessary to address the situation where there is no absorption. At the exit surface of the material, another reflection occurs. Therefore, the transmitted intensity can be written as a function of incident intensity as,

$$I_T = (1 - R)^2 I_0 \tag{3.7}$$

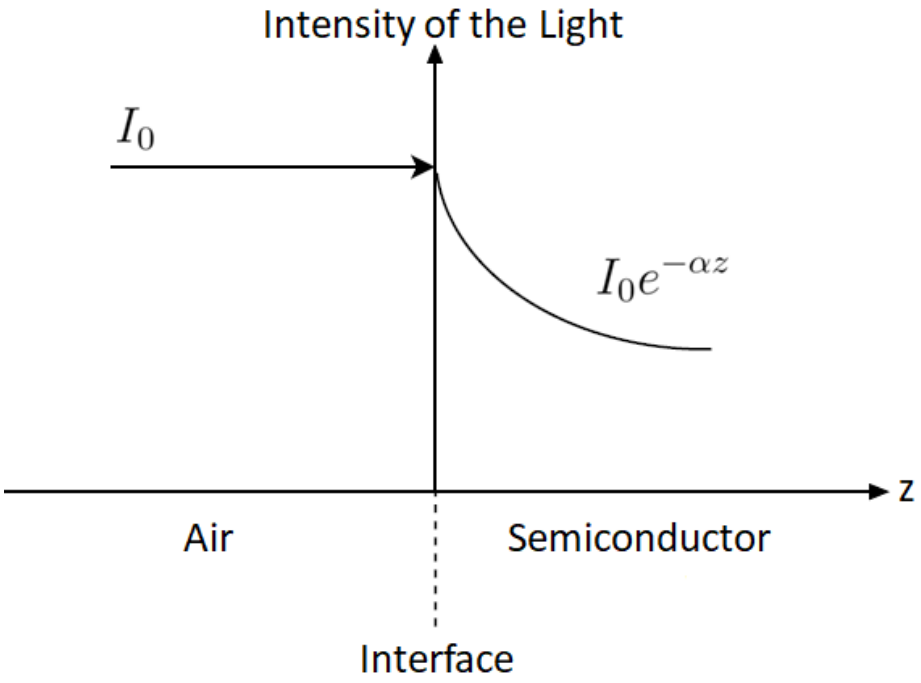

Figure 3.6. Attenuation of the incident light.

where squared term is obtained from the fact that the two reflections from two interfaces of material. At this point, the basic formula of transmittance which is the ratio of the transmitted intensity and incident intensity becomes,

$$T = \frac{I_T}{I_0} = (1 - R)^2 \cdot \tag{3.8}$$

With multiple reflections taken into account, the transmission can be written as [71],

$$T = \frac{(1 - R)^2}{(1 - R^2)} \cdot \tag{3.9}$$

Adding absorption parameter into equation gives the final form of transmission:

$$T = \frac{(1 - R)^2 e^{-\alpha t}}{1 - R^2\, e^{-2\alpha t}} \tag{3.10}$$

where t is the thickness of the material.

Since reflectance is a parameter in terms of refractive index n as shown in equation 3.4 and n is directly related to the wavelength, the reflectance becomes a function of wavelength. In this regard, it is clear that transmission is a function of wavelength. Solving this equation gives absorption coefficient α as a function of λ.

To express the functional form of transmission, the reflectance parameter should be described in respect to attenuation effect. This can be conveniently taken into account by defining a complex refractive index as,

$$\overline{n} = n + i\kappa \tag{3.11}$$

where κ refers extinction coefficient and related to the absorption coefficient as,

$$\kappa = \frac{\alpha\lambda}{4\pi} \tag{3.12}$$

where λ is the incident light wavelength. Substituting this into equation3.4 gives,

$$R = \left|\frac{\overline{n}-1}{\overline{n}+1}\right|^2 = \frac{(n-1)^2-\kappa^2}{(n+1)^2-\kappa^2}. \tag{3.13}$$

Moreover, writing κ in terms of α results reflectance as a function of n, α and λ as,

$$R = \frac{(n-1)^2-\left(\frac{\alpha\lambda}{4\pi}\right)^2}{(n+1)^2-\left(\frac{\alpha\lambda}{4\pi}\right)^2}. \tag{3.14}$$

Thus, implying equation 3.14 into 3.10 gives,

$$T = \frac{\left[1-\frac{(n-1)^2-\left(\frac{\alpha\lambda}{4\pi}\right)^2}{(n+1)^2-\left(\frac{\alpha\lambda}{4\pi}\right)^2}\right]^2 e^{-\alpha t}}{1-\left[\frac{(n-1)^2-\left(\frac{\alpha\lambda}{4\pi}\right)^2}{(n+1)^2-\left(\frac{\alpha\lambda}{4\pi}\right)^2}\right]^2 e^{-2\alpha t}}. \tag{3.15}$$

Simplifying this equation gives transmission as a function of α, λ, n and t as,

$$T(\alpha,\lambda,n,t) = \frac{4096\, e^{\alpha t}\, n^2\, \pi^4}{-\left[16(-1+n)^2\, \pi^2\, \alpha^2\, \lambda^2\right]^2 \; + e^{2\alpha t}\; \left[16(1+n)^2\, \pi^2\, \alpha^2\, \lambda^2\right]^2}. \tag{3.16}$$

Numerical calculations are done for transmittance with an algorithm in MATLAB, with respect to different wavelengths, and accordingly different absorption coefficient values. One more simplification can be made under consideration of the working range of wavelengths. As the infrared light wavelength λ is the order of 1×10^{-6}, it can be said that $\alpha < 10^6\, m^{-1}$. Thus, the $\alpha\lambda$ parameters at the denominator will be smaller than 1 or at most 1. Accordingly $(\alpha^2\lambda^2)^2$ becomes much smaller than 1 and simplified transmittance can be written as follows [72],

$$T = \frac{16\, e^{\alpha t}\, n^2}{-(-1+n)^4 \; + e^{2\alpha t}\, (1+n)^4}. \tag{3.17}$$

In consequence of the assumption for simplification, it can be said that $\alpha{<}1\times10^4 cm^{-1}$. Herein, it would be coherent to make a calculation for reflectance and transmittance according to available GaAs parameters. As the refractive index is a wavelength dependent parameter, to obtain the refractive index of GaAs sample, Sellmeier Equation (3.18) is used.

$$n(\lambda) = \sqrt{A + \frac{B}{1 - C^2\, /\, \lambda^2}} \tag{3.18}$$

where λ is the wavelength in μm, A=8.950, B=2.054 and C^2=0.390 are empirical Sellmeier coefficients for GaAs. According to this equation, the refractive index n for different wavelengths is plotted as a graph and shown in Figure 3.7.

Implying calculated n values according to equation 3.18, into equation 3.4 and equation 3.17 gives reflectance and transmittance values for pure GaAs sample and are shown in Figure 3.8 and Figure 3.9 respectively.

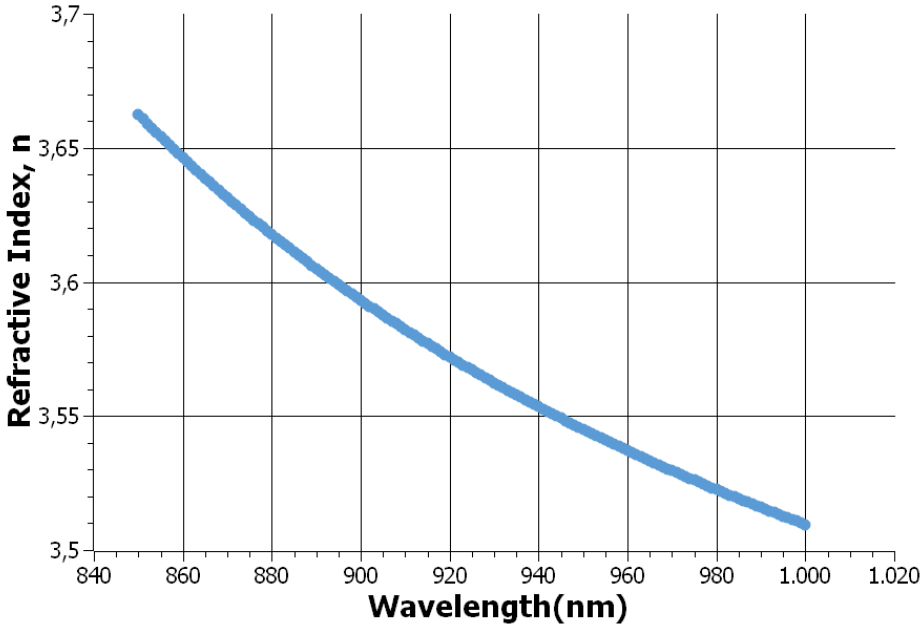

Figure 3.7. Refractive index change of GaAs for different wavelengths.

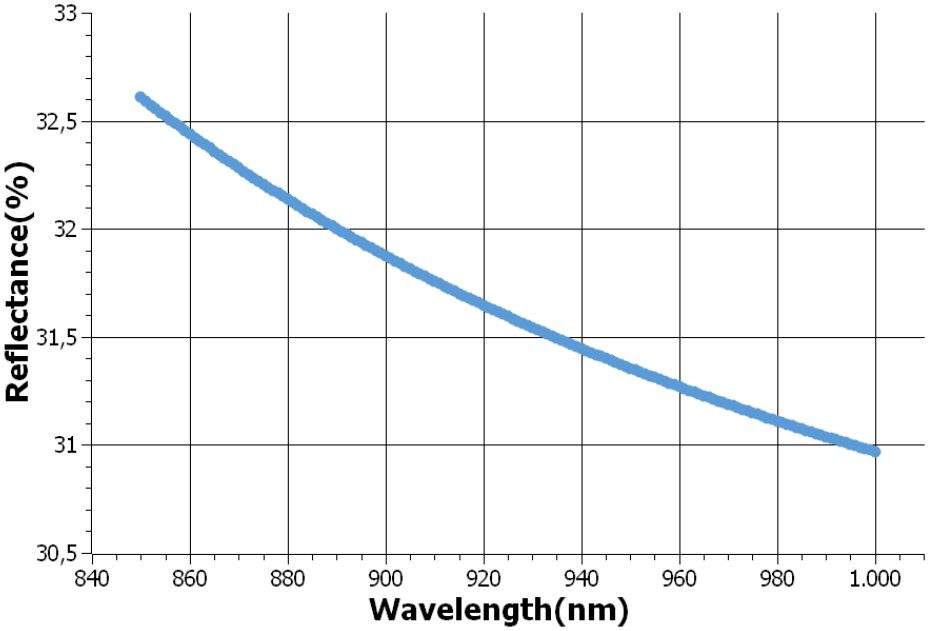

Figure 3.8. Calculated reflectance data of pure GaAs for different wavelengths.

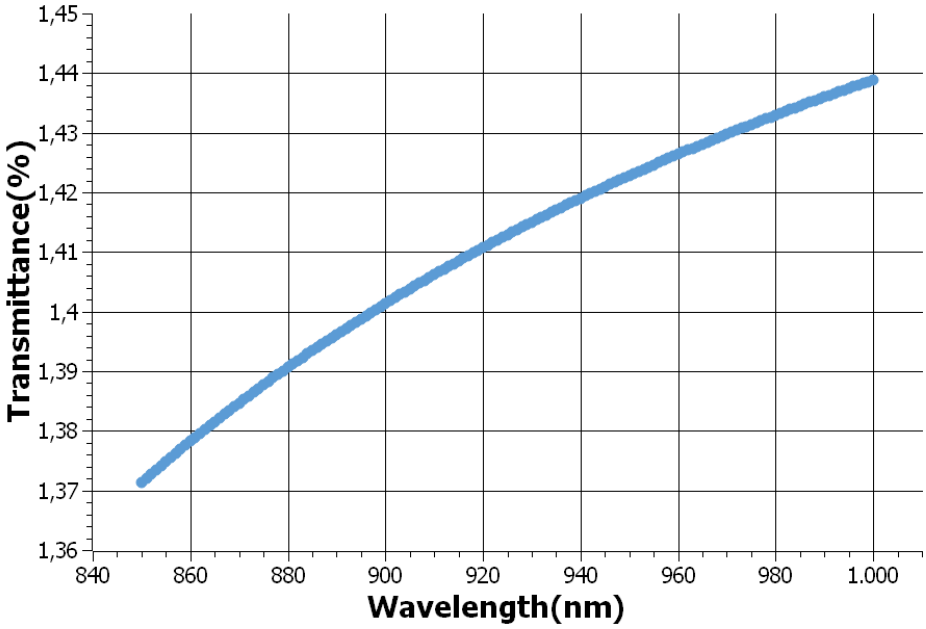

Figure 3.9. Calculated transmittance data of pure GaAs for different wavelengths.

Correspondingly, putting obtained reflectance and transmittance data sets into equation 3.3 gives absorption as shown in Figure 3.10.

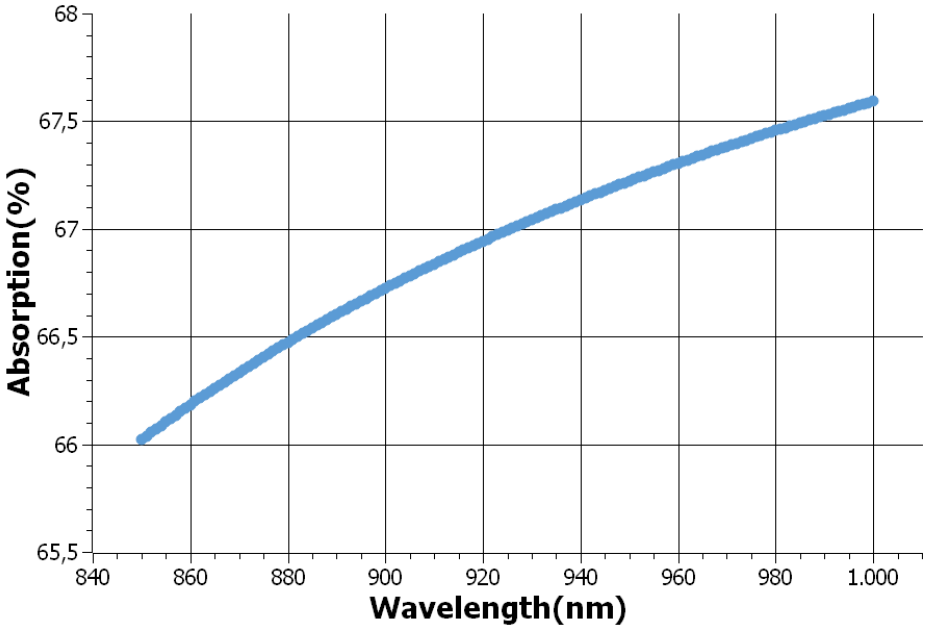

Figure 3.10. Calculated absorption data of pure GaAs for different wavelengths.

3.3. Experimental Setup

The optical characterization calculations in section 3.2 are made for pure (undoped) GaAs. However, available sample in our lab is a single side polished and 350 μm thick P-type GaAs which has similar properties with pure one. The technical properties are given in Appendix A. To measure optical transmission of the sample, a Thorlabs CCS200 compact CCD spectrometer is used. Mainly, there are experienced two setups, one of them is heating the sample directly with heat source, and another one is heating the sample which is mounted into the water filled chamber with known temperature. For both setups, there are used four light sources as:

- 875 nm Everlight SIR333/H19/F51-R11 LED.
- 880 nm Thorlabs LP880-SF3 laser source.
- 940 nm Everlight IR8353-14C LED.
- 980 nm Roithner-laser RLDH980-70-3 laser source.

It is observed that, for each experiment with 880 nm and 980 nm laser sources, P type GaAs does not transmit any light. Therefore, the LED sources are used which has wider bandwidth spectrum as shown in Appendix B.

3.3.1. Setup-1 Sample heated directly

To obtain the transmittance change of the sample, installed setups include a mounted LED, two collimating lenses, sample and Optical Spectrum Analyzer (OSA). Both LEDs are driven 1.4 volts and 95 mA. Radiated light from the source is adjusted and collimated with two plano convex lenses. For 875 nm LED, lenses have 50 mm focal length. However for 940 nm LED, used lenses had 35mm and 25.4 mm focal lengths respectively. Beam size is minimized around 700 μm and it is reached to the polished side of GaAs sample as shown in Figure 3.11. After the light beam traveled 350 μm along in the sample, transmitted light was measured with OSA tip fixed on the other side of the sample.

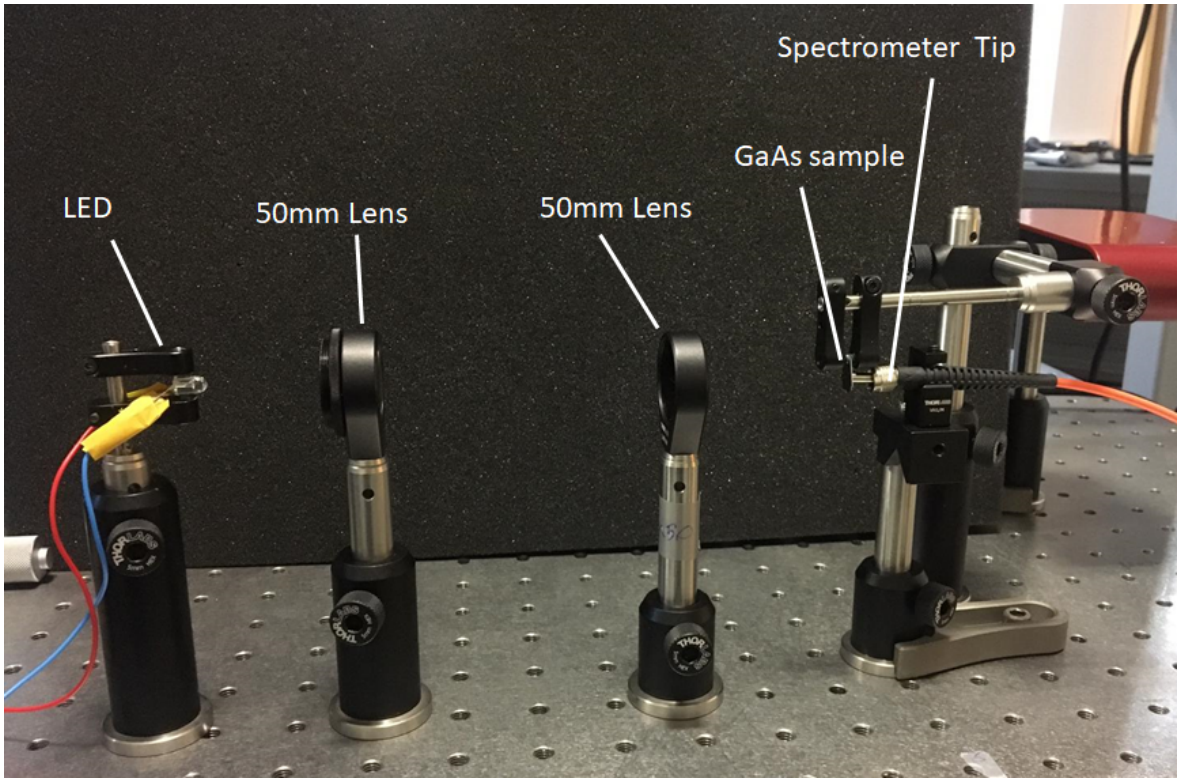

Figure 3.11. Experimental setup of system with directly heat source.

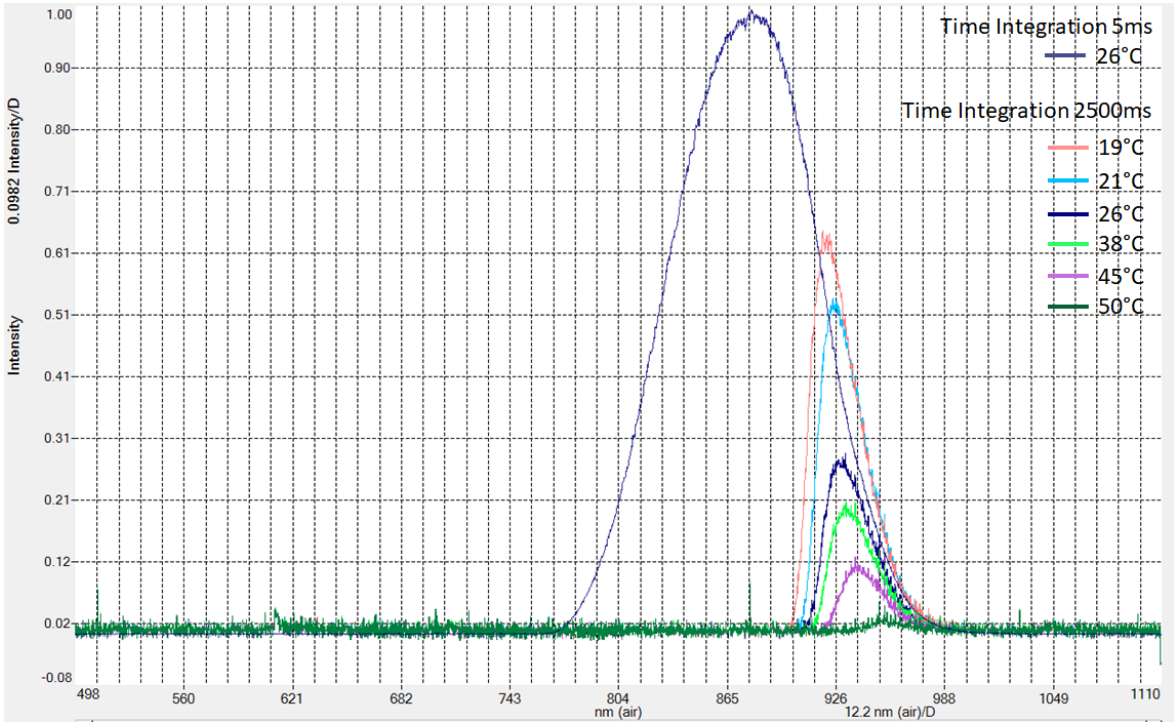

Figure 3.12. Transmitted intensity graph of 875 nm light on directly heated sample.

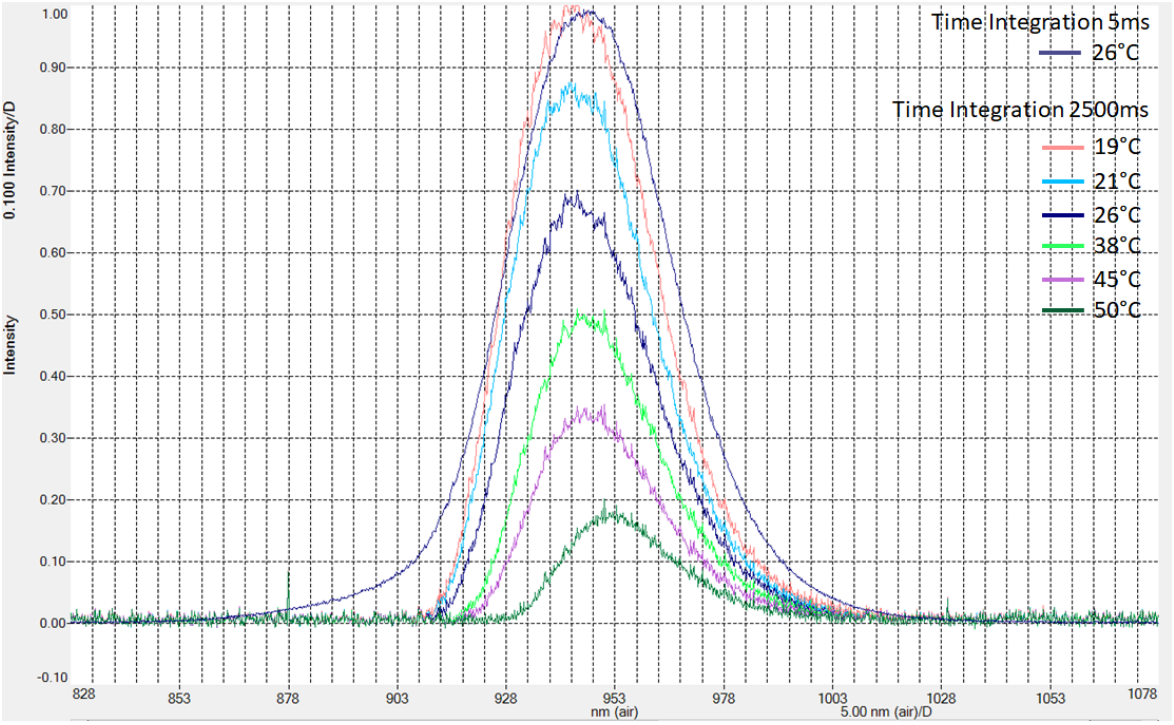

Figure 3.13. Transmitted intensity graph of 940 nm light on directly heated sample.

Also,the power of the light here measured as 8 mW for 875 nm LED and 5.5 mW for 940 nm LED. The sample is heated with a hot well and the temperature value on the sample surface is measured with an IR thermometer. According to this setup, obtained intensity and spectrum change graphs are shown in Figure 3.12 and Figure 3.13.

3.3.2. Setup-2 Sample heated with water

To be able to simulate the blood temperature and acquire more controllable data sets, sample is mounted in a chamber full of water as shown in Figure 3.14.

Same setups are installed for both LED light sources but GaAs sample is mounted in a water filled chamber. During measurements, the water in the chamber is heated to 45 °C and it is cooled until 20 °C. A W1209 thermostat is used as a reference sensor. The intensity change and spectrum shifts are presented in the Figure 3.15 and Figure 3.16.

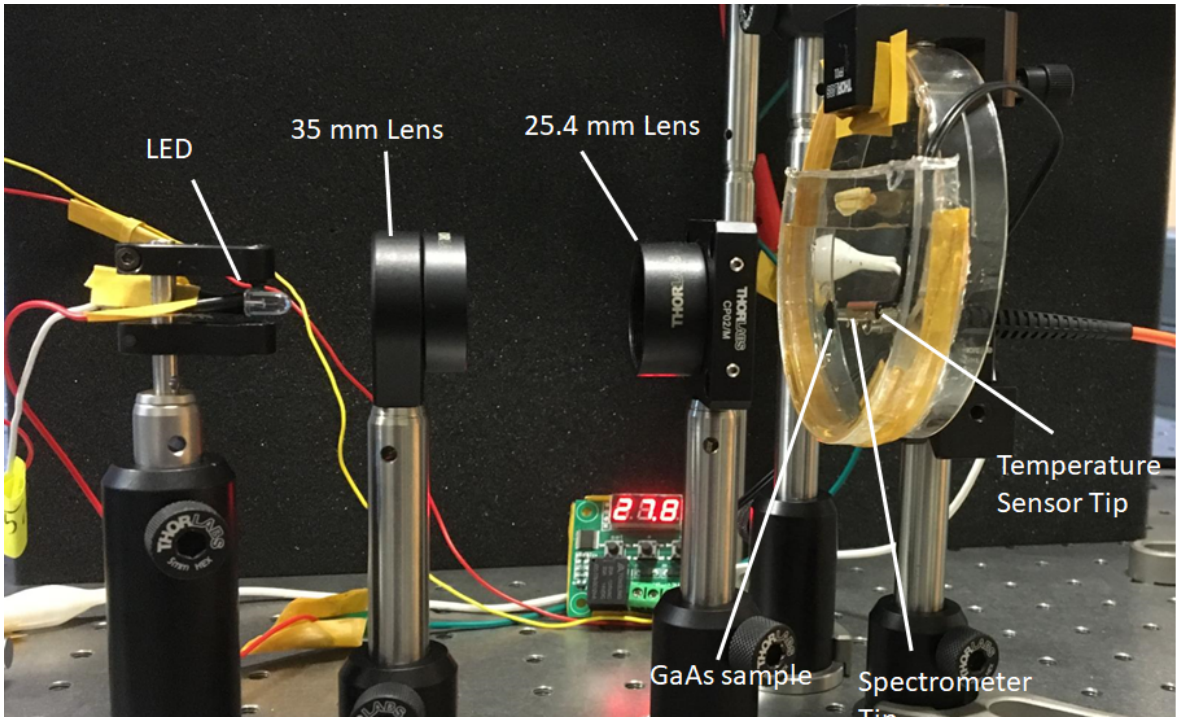

Figure 3.14. Experimental setup of system heated with water.

Thus, it can be said that temperature dependent transmission data shows some band gap changes. This change causes the spectrum shifts of transmitted light, intensity changes and accordingly transmittance of the GaAs sample. It should be noted that plotted intensity values on the graphs are taken in 2500 ms time integration, whereas the direct light intensity was measured in 5 ms time integration which means our sample transmits the light in 1/500 amount.

According to plotted graphs, for 875 nm LED light source, P type GaAs sample has its cut-off wavelength at 932 nm, which means its E_g is 1.334 eV and its intensity is 0.230/1 at room temperature. Decreasing the temperature of the sample to the 20 °C causes shift in peak wavelength to 925 nm, where E_g is 1.344 eV and its intensity is 0.340/1. Heating sample to 45 °C shifts spectrum to 937nm where E_g becomes 1.327 eV and the intensity of the light is 0.140/1 in arbitrary units.

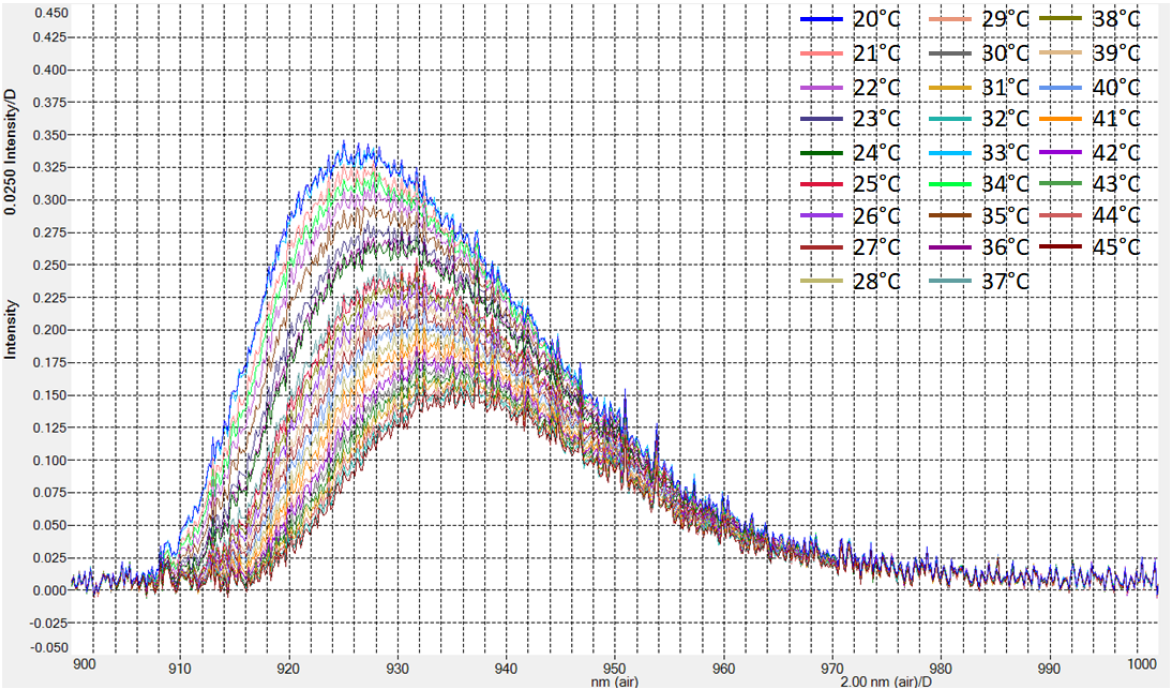

Figure 3.15. Transmitted intensity graph of 875 nm light in heated water chamber.

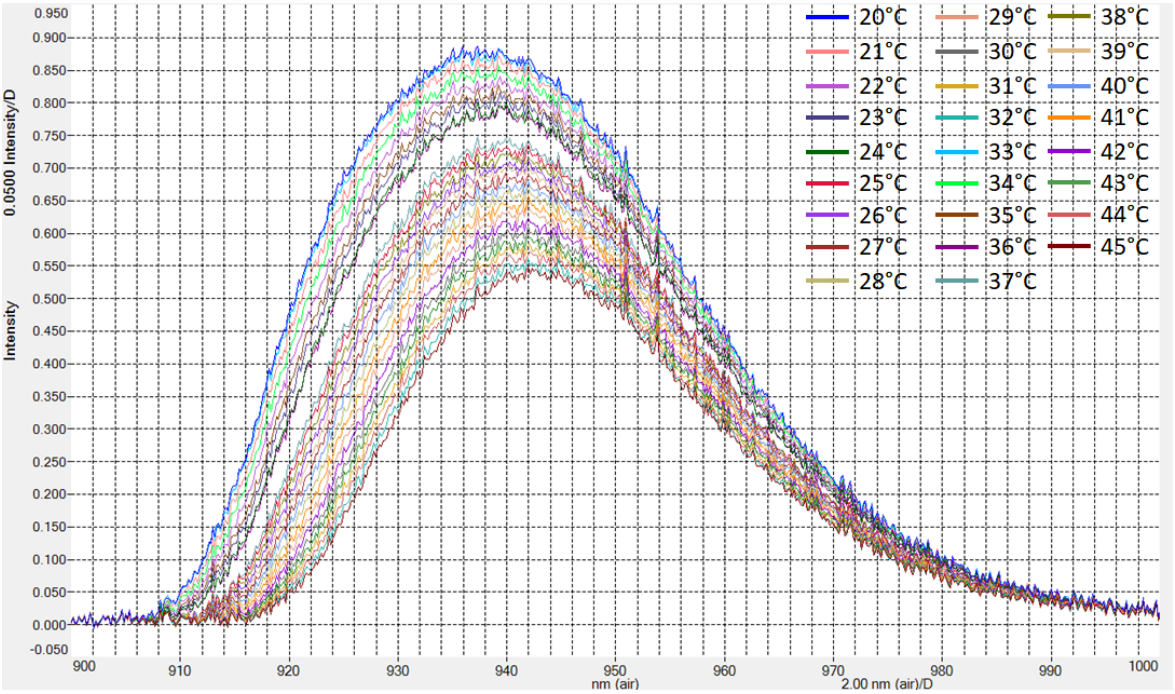

Figure 3.16. Transmitted intensity graph of 940 nm light in heated water chamber.

Similarly, for 940 nm LED light source, transmitted light from the sample shows peak wavelength at 940 nm, with 1.323 eV E_g value and its intensity is 0.725/1 in

arbitrary units at room temperature. Decreasing the temperature to 20 °C shits the peak to the 936 nm where E_g is 1.329 eV and intensity is 0.875/1 and heating the sample to the 45 °C causes spectrum shift to the 945 nm and E_g to the 1.316 eV where its intensity in first setup is 0.250/1 and in second setup is 0.540/1 in arbitrary units.

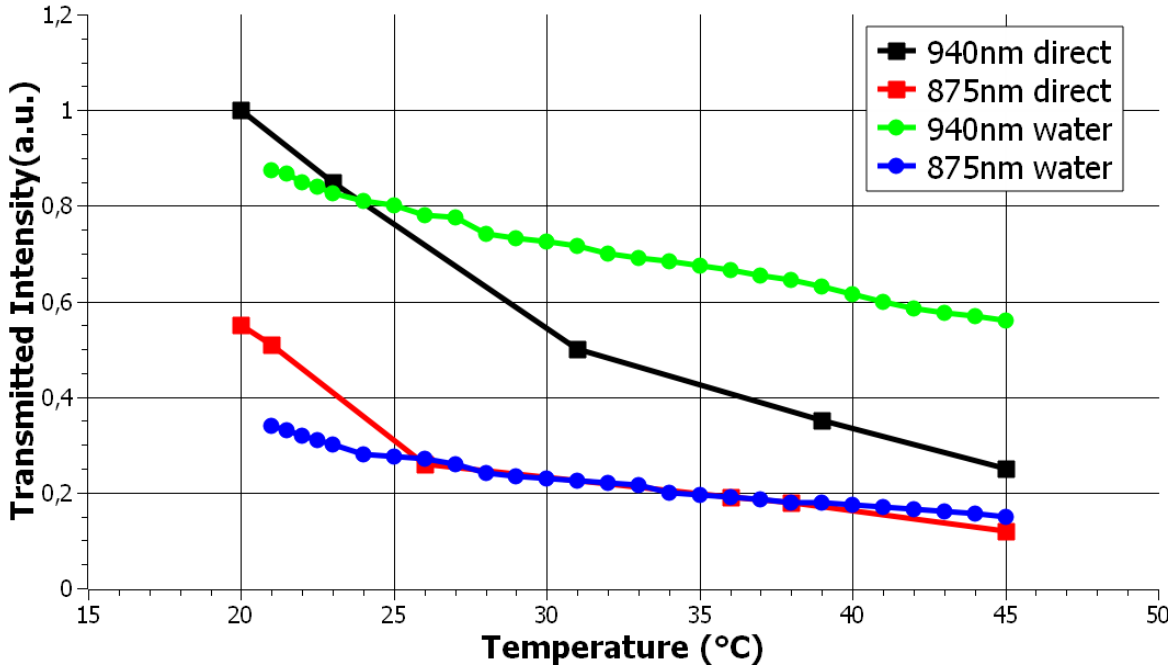

Figure 3.17. Intensity values of the transmitted light for four cases.

As a result, it is observed that GaAs sample acts as a band-pass filter . At some specific wavelength of the light, material generates direct interband recombination of electron and holes, where no phonon interaction is necessary. Hence, some of the light is transmitted, while some is absorbed. At this point, increasing the temperature of the sample shrinks the gap in between valance and conduction bands which enhances the absorption ratio of the sample. Correspondingly, the transmitted intensity of the light on the other side of the sample diminishes as shown in Figure 3.17.

As the minimum detectable spectrum change of the OSA is 0.6 nm, and changing the temperature from 21 °C to 46 °C corresponds to change in the spectrum from 925.04 nm to 937.39 nm, the minimum detectable temperature change is reported as 1.215 °C and the sensitivity of the sensor is calculated as 0.494 nm/°C.

4. PRESSURE SENSING

High precision pressure measurement is extremely important in many areas, especially in medical applications. Since one of the primary determinants of blood flow in regional vascular beds is perfusion pressure, it should be tracked during the operation. There are many pressure sensors are investigated to measure the blood pressure which are self-contained devices. However, they have to provide their own power supply with batteries or transcutaneous energy transfer and data read-out circuits [73]. As the presented system is aimed to work with MRI, the sensor should be without electrical components because of heating and interferences on the signal. Also, as the total size of the system will have 2.2 mm diameter to be implementable for vessel, sensor structure should be as small as possible. For this reason, the pressure sensor to be integrated with the intravenous medical device is realized with MEMS technology using optical reading methods.

This sensor architecture is based on a micro-membrane structure that separates its environment from a reference cavity. Pressure differences in body environment and the reference cavity cause bending on the micro-membrane. This bending can be measured with nanometer precision with interferometer structure via fiber optical connections. The designed pressure sensor is completely passive and it is not necessary to transfer power to the sensor that travels through the body or to return the sensor information as an electrical signal.

4.1. Optical Readout of the System

As the system does not have any electrical components, the deflection of the membrane is determined by optical methods. For that reason, diffraction gratings are designed under the membranes to serve as reference reflectors for read-out as shown in Figure 4.1 . The reflected light from the gratings and the membrane create interference pattern on the observer plane. The distance in between membrane and gratings are modulated with the external pressure caused by the change of environment pressure.

Correspondingly, the displacement of the membrane causes the intensity change at observer plane and in this way, signal becomes modulated. Therefore, the pressure change on the membrane can be easily observed to the intensity of the reflected light.

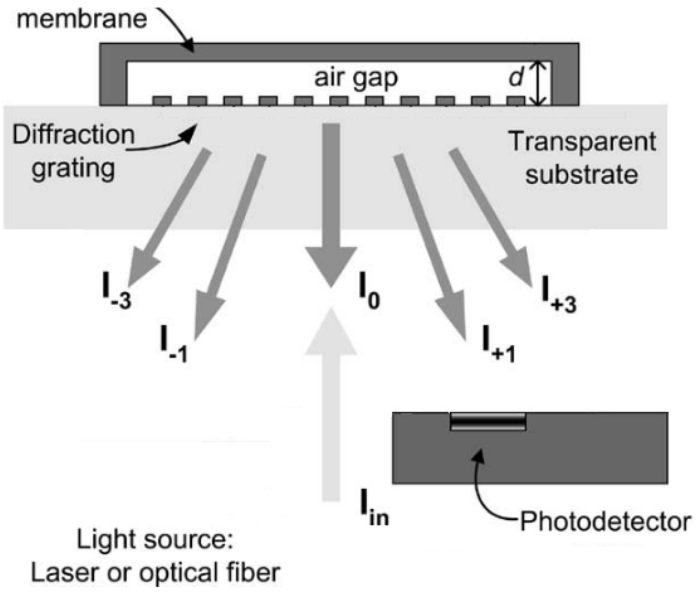

Figure 4.1. The micro-interferometer with diffraction grating for readout optics.

4.2. Diffraction Grating Interferometer Theory

To begin with, interferometry is a measurement method which using the superposition principle of EM waves. They are called interferometers because they work by merging two or more sources of light to create an interference pattern, which can be measured and analyzed. Interferometers are generally using to detect the small displacements or surface irregularities in many disciplines.

As the principle of interference, two or more waves are interact. Because of the superposition, photons pass through to the same location in space and they are added together as they interact. The resulting wave named as the interference pattern. The Figure 4.2 shows two different cases of interference. Total constructive interference happens when the peaks of waves perfectly match up in phase, they are adding together and constructing a larger wave as a sum of the merged waves where they are physically

interacting. On the other hand, destructive interference occurs at the opposite case of constructive case. The positive and negative peaks of waves meet and match through the wave out of phase, and they get absorbed, or in some cases, totally destroy each other [74].

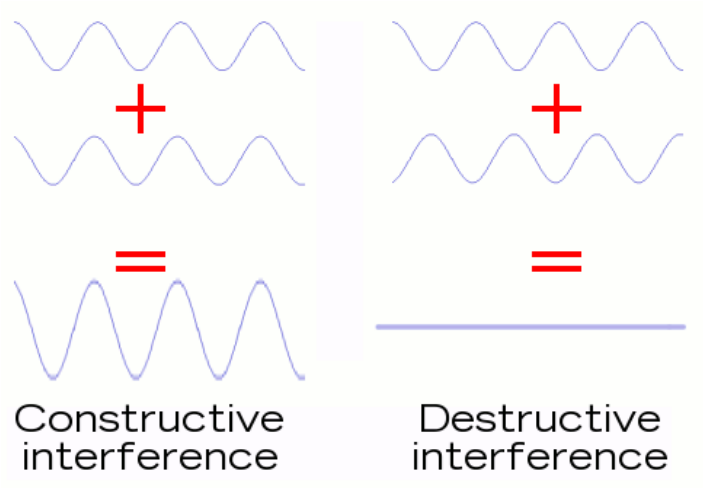

Figure 4.2. Constructive and destructive interferences of waves [74].

In addition to interference, waves also exhibit a diffraction property, which can be explained as the bending of waves as they pass through an aperture. According to Huygens principle, when light waves are passing through a slit, they will spread out and exhibit an interference pattern in the region beyond as shown in Figure 4.3. Here, the central maxima is the larger than the either side patterns or minimas, and accordingly, the intensity decreases rapidly on the sides [75].

In the proposed sensor, for the analysis of the intensity of the light at the observer plane, calculations can be simplified by seperately computing the components. Instead of computing the amplitude of the light, it is more advantageous to deal with the intensity of the light transmitted through a diffraction gratings [76]. Here, as the system has gratings and membrane, the reflected light intensity propagates with an optical path difference (OPD) of δ as shown in Figure 4.4. When this path difference is equal to an integral multiple of wavelengths, all the slits will constructively interfere with each other and a bright spot will appear on the screen at an angle θ [77]. Thus,

the condition for the principal maxima becomes;

$$\delta = d_s \sin\theta = m\lambda, \quad m = \pm 1, \pm 2, \pm 3, ... \tag{4.1}$$

where d_s is the slit width, λ is the incident light's wavelength, θ is the angle relative to the original direction of the light and m is the order of the minimum.

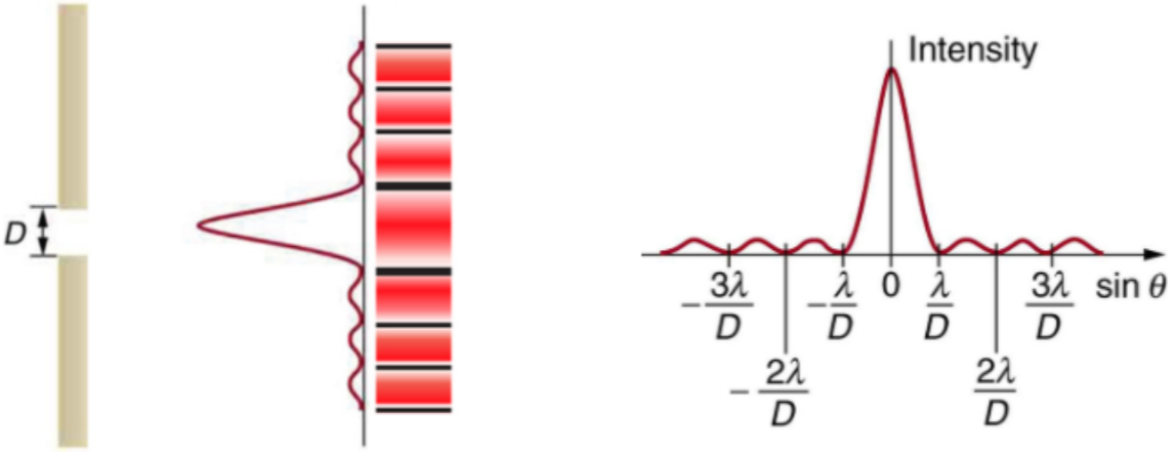

(a) Diffraction pattern. (b) Diffraction intensity.

Figure 4.3. Single slit interference [75].

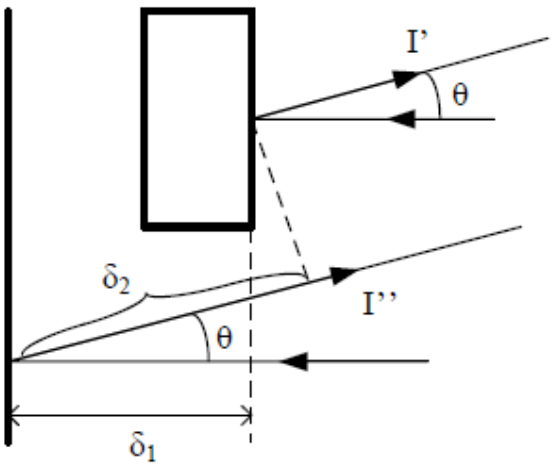

Figure 4.4. Schematic of optical path difference [76].

On the other hand, diffraction grating may consists of a large number of slits with same widths and separated from the next one by a distance d_s. In the case that the incident light is planar and diffraction spreads the light from each slit over a wide-angle, the light rays from each slit are merged and interfere with each other. Similarly, the path difference between slits becomes again $\delta = d_s \sin\theta$. If the path difference in between the slits are equal to an integral multiple of wavelengths, all the slits are merged and interfere with each other as shown in Figure 4.5. Thus, bright spots will appear on the screen at angle θ [77]. The equation for the principal maxima will be the same as Equation 4.1 as the system works with same fundamental. Also, the location of the maximas does not depend on the slit number. However, increasing the number of slits causes the sharper maximas. According to presented theory, optical interfero-

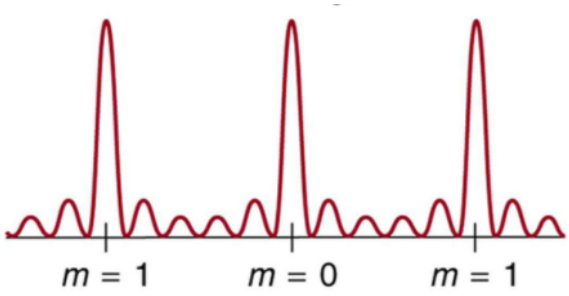

Figure 4.5. Light passing through a diffraction grating [75].

metric displacement detection capability is integrated into the probe by patterning the membrane and the substrate as diffraction grating. Here, diffraction grating enables to measure the displacement with its phase sensitivity ability. When a light beam illuminates the membrane from the back side, the reflected light is separated into different diffraction orders. At that point, some of the light is reflecting form gratings and some of them is passing through and reflecting from the membrane [78]. Therefore, the intensity of the light at the diffraction orders changes sinusoidally, result different oscillations as a function of the gap in between the membrane and grating substrate. The intensity of the reflected light of for 0^{th} and 1^{st} orders can be formulated as [79]:

$$I_0 = I_{in} \cos^2\left[\frac{2\pi d}{\lambda}\right], \qquad I_{\pm 1} = \frac{4I_{in}}{\pi^2} \sin^2\left[\frac{2\pi d}{\lambda}\right] \tag{4.2}$$

where I_{in} and λ are the intensity and the wavelength of incident light respectively and d is the gap height. As it can be seen from the formulas, there is a 180° phase difference in between the 0^{th} order and other orders. Based on the Equation 4.2, the intensities of 0^{th} and 1^{st} orders can be plotted as a function of the gap and wavelength as shown in Figure 4.6.

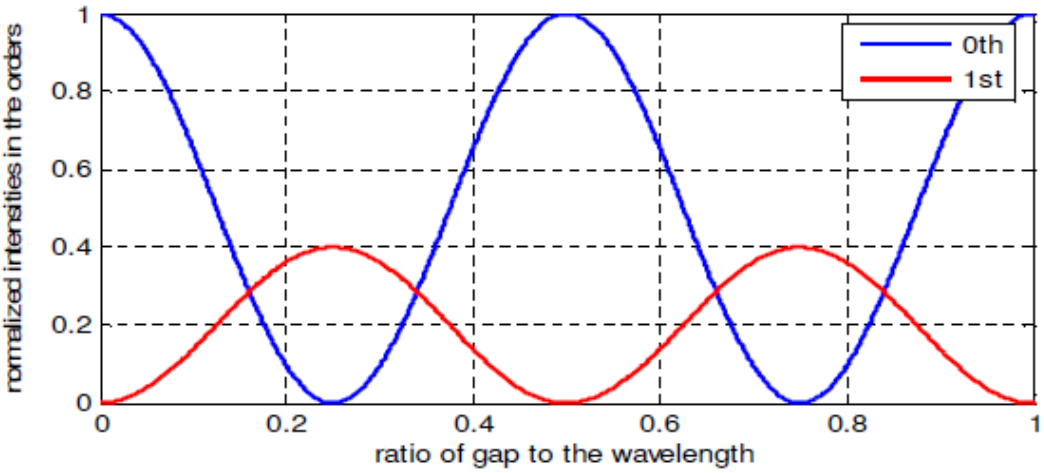

Figure 4.6. Intensity of the light in the orders as a function of distance in between membrane and gratings [76].

4.3. Design and Simulations

The membrane structure to be used for pressure sensing is manufactured by microprocessing methods to create a reference pressure. Thanks to this process, it is ensured that a micro-sized chamber that is tightly kept at a certain pressure is formed. As the shape of the membrane, the advantage of the symmetrical bending of the disc has led to the preference of these structures rather than the squared shape.

The pressure sensor design studies focused on disc-shaped Parylene-C (chemical vapor deposited poly p-xylylene polymer) based structures. Different metal layers of different thicknesses are placed on the top and bottom of the structural material Parylene in the simulation environment, thus it is aimed to minimize the sensitivity of the pressure sensor to temperature.

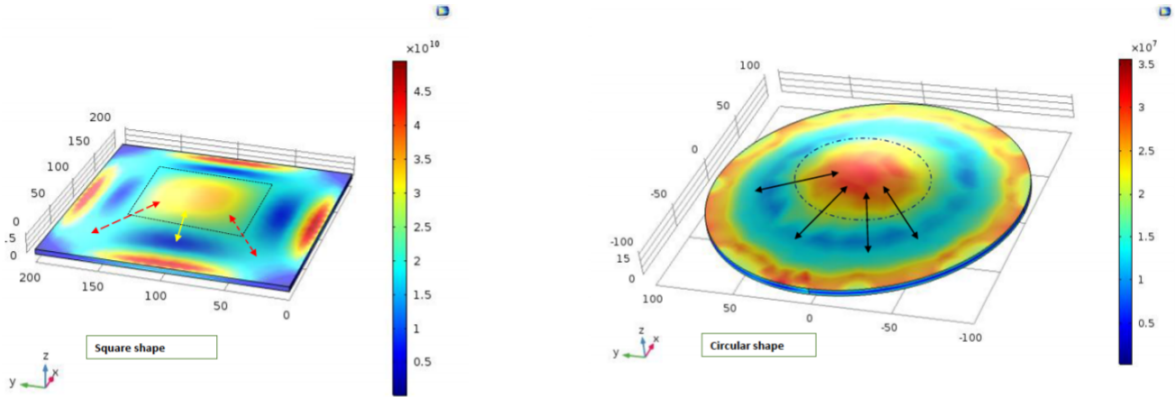

Figure 4.7. Bending simulations for square and circular shape membranes.

The following criteria have been observed in the design of the pressure sensor:

- The nominal pressure value at the upper part of the sensing membrane is 60-140 mmHg (typical pressure range measured from blood).
- The membrane should move 100-150 nm for 80 mmHg pressure change within the range of 60-140 mmHg which is intended to be measured.
- This amount of movement corresponds to a quarter of the red light wavelength to be used. In case the pressure range to be measured coincides with a range of motion that corresponds to a quarter wavelength, the minimum and maximum amount of light will be obtained from the interferometer to be created.
- Parylene structural layer is sandwiched in between two metal layers which have approximately 100 and 300 nm thicknesses to decrease the thermal effects of the environment.

Based on the listed criteria, COMSOL simulations on the micro membranes are performed. According to Figure 4.7, the movement of the pressure detector is taken into consideration by the average of 100 μm x 100 μm area, that deflects with the applied pressure. First of all, according to the data obtained from the area in the middle of the sensor, the bending amounts and profiles of the pressure sensors designed with different sizes, materials, and material thicknesses are observed with the finite element method according to 60-140 mm-Hg pressure. As the device expands sideways, even

with the same thickness of the metal layers placed above and below the structural layer, eventually a bending of around a few nm is observed per temperature variation in °C.

To set the boundaries of the sensor, the simulated structure's metal layers are chosen according to availability in the cleanroom. As aluminum and titanium are the most reflective metals among the available ones, simulations are planned for realization with these materials. In the simulation results presented below, the amount of the membrane movement according to applied pressure and temperature data for different metal layer thicknesses (100 - 300 nm range) and different disc radius are shared.

Presented cases are for the different parylene layer structures as 1 μm, 3 μm and 5 μm thickness values. Accordingly in the below graphs, the y-axis shows the membrane radius and the x-axis shows the metal layer thickness for each Parylene-C thickness. The contour lines demonstrate the difference in movement of the 60 and 140 mm-Hg pressure amounts where the average of displacement in nm for ΔT=0 °C, ΔP=80 mmHg in present of 760 mmHg for 100 μm^2. Areas painted in gray indicate places where there is more than the desired amount of movement (150 nm bending). The simulation results with aluminum layers are shown in Figure 4.8, 4.9, 4.10. Also, the simulation results with titanium layers are shown in Figure 4.11, 4.12, 4.13.

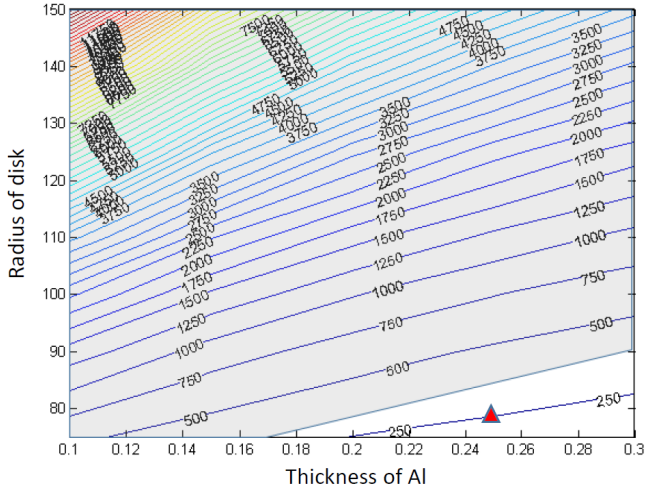

(a) Deflection change for ΔT=0 °C, ΔP=80 mmHg.

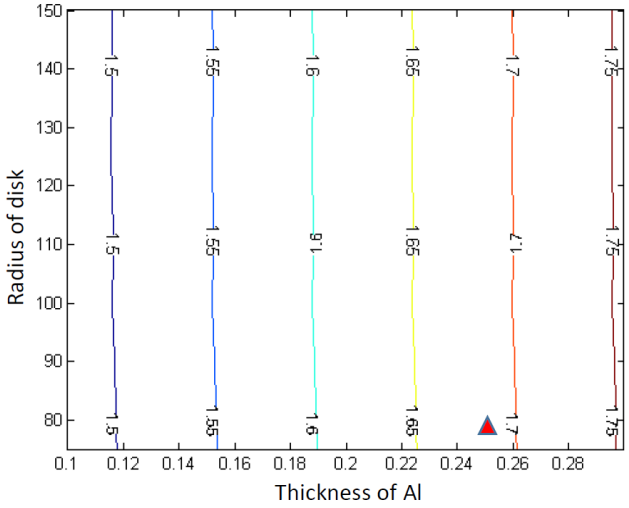

(b) Deflection change related to bottom metal thickness.

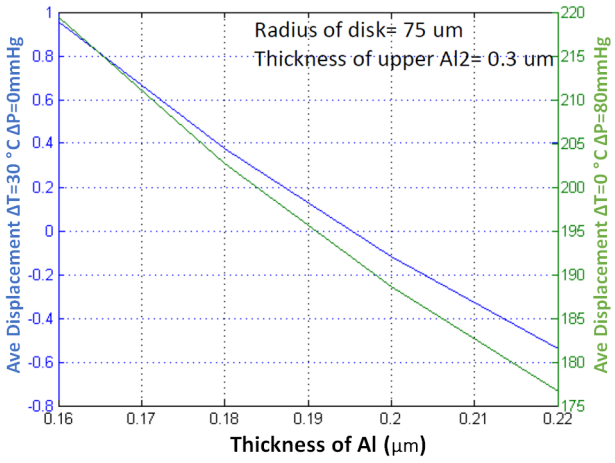

(c) Deflection change related to top metal thickness.

Figure 4.8. Simulation results for aluminum metal layers for parylene = 1 μm.

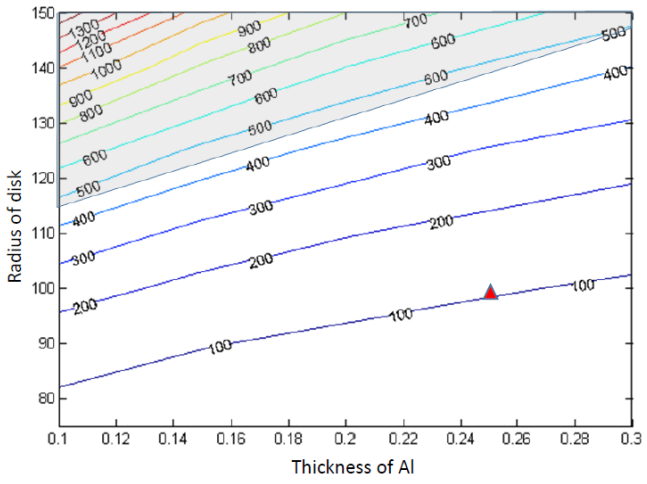

(a) Deflection change for ΔT=0 °C, ΔP=80 mmHg.

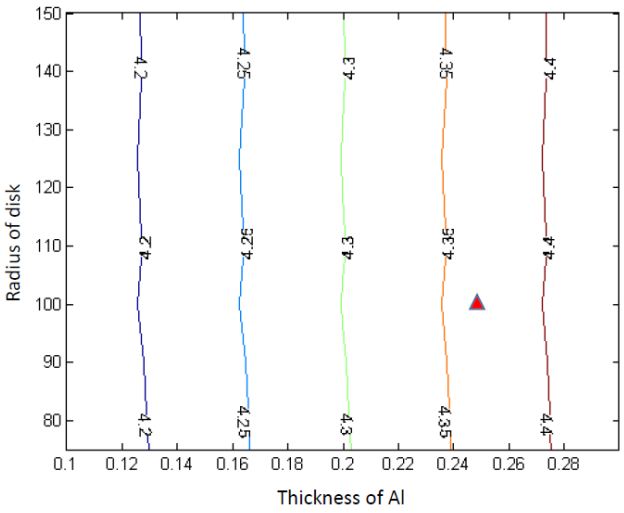

(b) Deflection change related to bottom metal thickness.

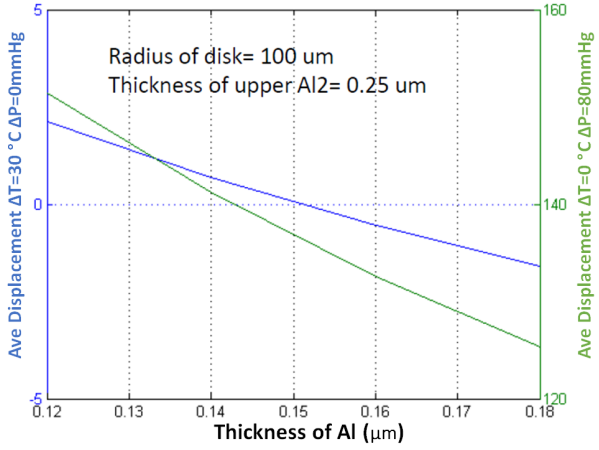

(c) Deflection change related to top metal thickness.

Figure 4.9. Simulation results for aluminum metal layers for parylene = 3 μm.

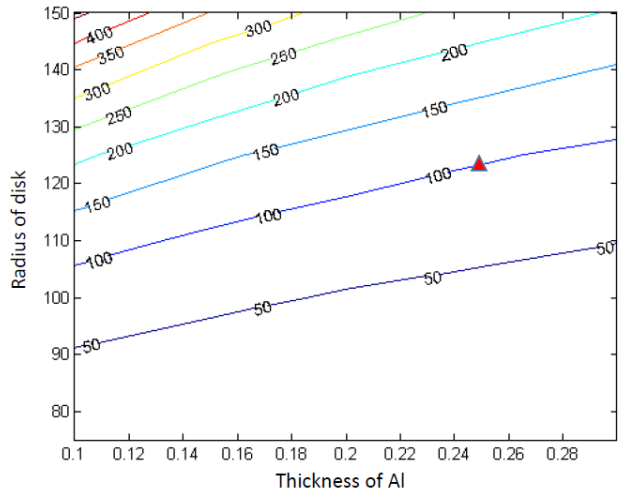

(a) Deflection change for ΔT=0 °C, ΔP=80 mmHg.

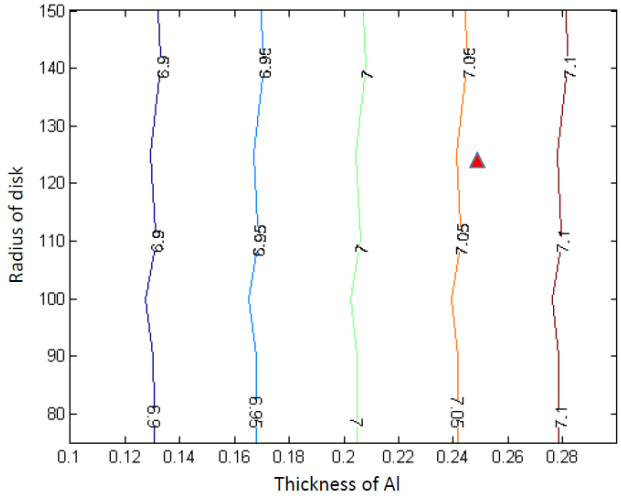

(b) Deflection change related to bottom metal thickness.

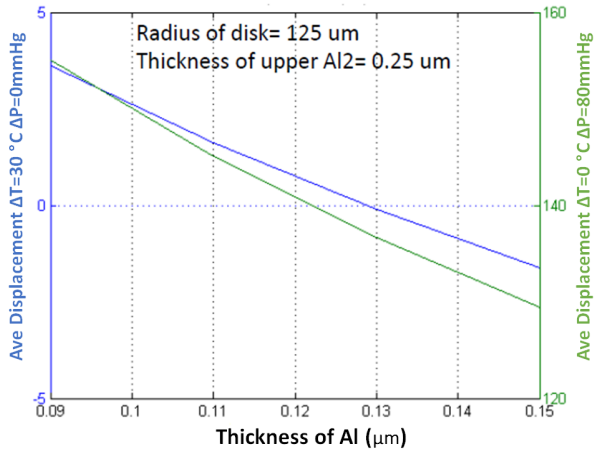

(c) Deflection change related to top metal thickness.

Figure 4.10. Simulation results for aluminum metal layers for parylene = 5 μm.

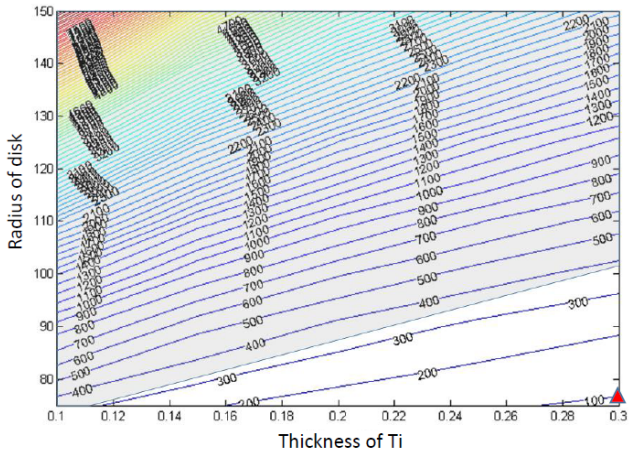

(a) Deflection change for ΔT=0 °C, ΔP=80 mmHg.

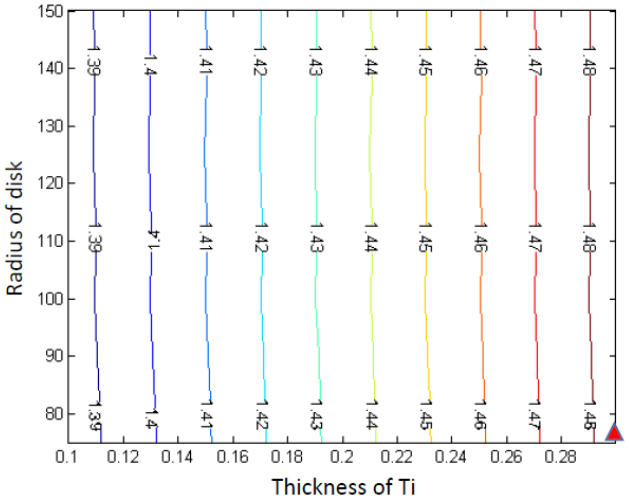

(b) Deflection change related to bottom metal thickness.

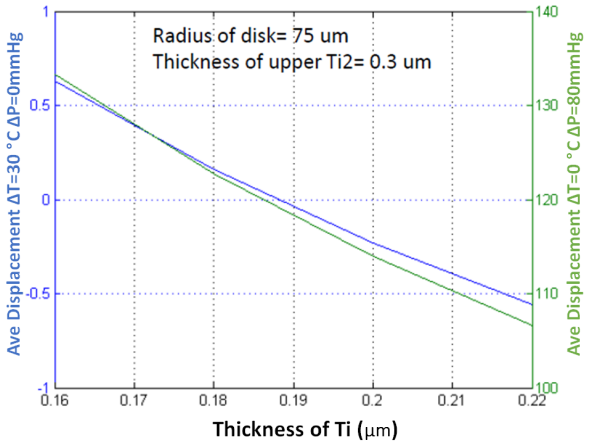

(c) Deflection change related to top metal thickness.

Figure 4.11. Simulation results for titanium metal layers for parylene = 1 μm.

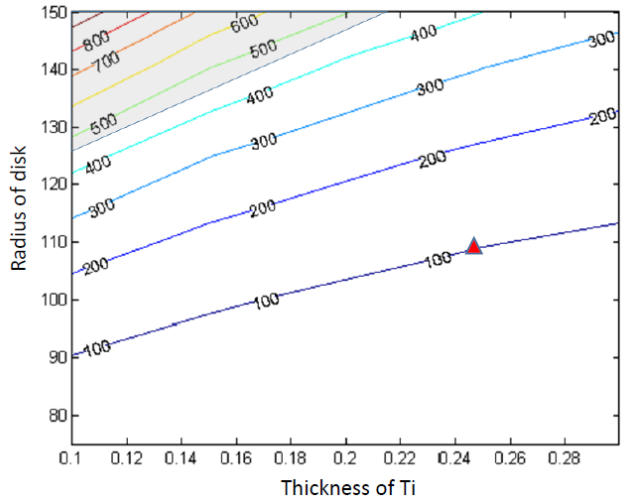

(a) Deflection change for ΔT=0 °C, ΔP=80 mmHg.

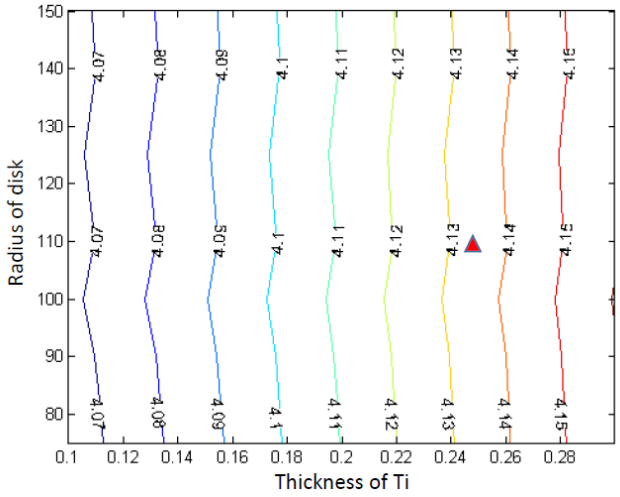

(b) Deflection change related to bottom metal thickness.

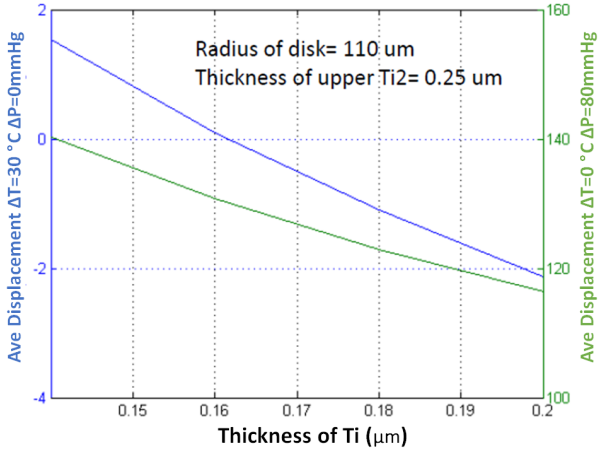

(c) Deflection change related to top metal thickness.

Figure 4.12. Simulation results for titanium metal layers for parylene = 3 μm.

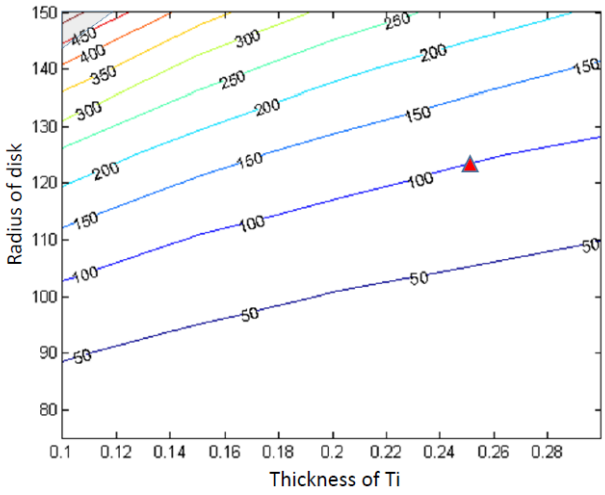

(a) Deflection change for ΔT=0 °C, ΔP=80 mmHg.

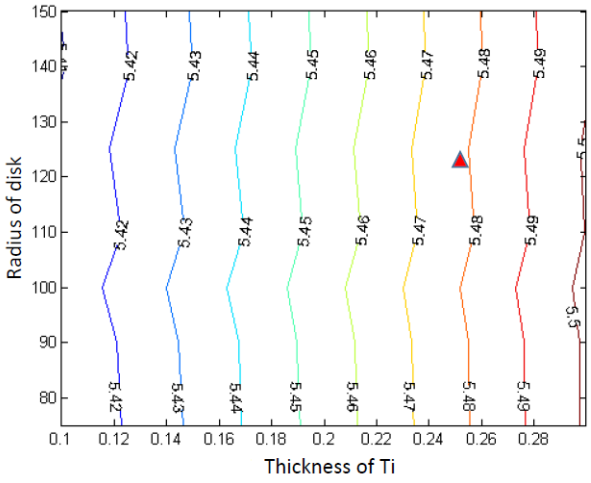

(b) Deflection change related to bottom metal thickness.

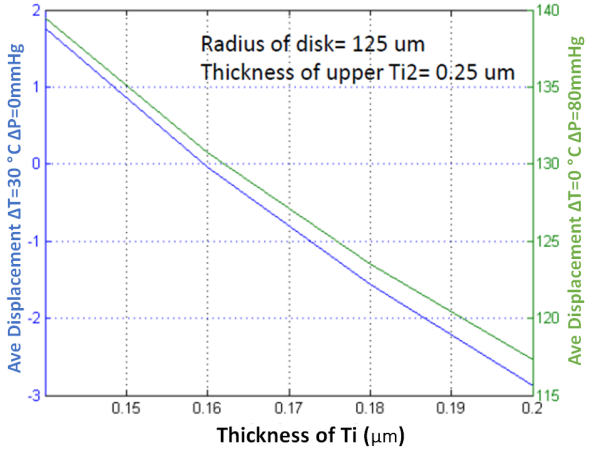

(c) Deflection change related to top metal thickness.

Figure 4.13. Simulation results for titanium metal layers for parylene = 5 μm.

The above figures show the simulation results of the temperature sensitivity obtained for aimed disc diameter and metal thickness. The desired amount of movement (150 nm) where the average of displacement in nm for ΔT=30 °C, ΔP=0 mmHg in present of 0 mmHg for 100 μm^2. Also, it is also shown that the temperature sensitivity for different thicknesses of the bottom metal layer as average displacement in nm. To get rid of the thermal occasioned deflections of the structure, some metal thicknesses are changed. The blue lines describe the average displacement change for ΔT=30 °C and ΔP=0 mmHg, on the other hand, the green lines identify the average displacement change for ΔT=0 °C and ΔP=80 mmHg.

In summary, the design of parylene structural layer 100-300 μm diameter sandwich model membranes are simulated using the finite element method (FEM) in the COMSOL software environment. To identify the thickness of the main structure parylene, three different simulations are realized for both aluminum and titanium metals.

As it can be seen in the figures on top left, as the radius increased, the membrane deflected more. In the case that the thickness of the parylene is 1 μm, the membrane deflection is more than desired which can cause some unwanted bends.

Although for 3 μm thick parylene based metal coated membranes giving better results for average displacement depending on the radius of the disk, there are undesired bendings on membrane for the size above 125 μm.

On the other hand, the simulation which are performed with 5 μm parylene thickness, gave results in desired values. According to Figure 4.10 and 4.13, the membranes can deflect smoothly up to 250 μm radius size. Also, it is observed the thickness of bottom metal layers are giving good results for thermal expansion in the required thickness for reflecting the light. Lastly, increasing the top metal layers thickness up to 350 μm range gains good athermal ability to the structure.

Based on the results obtained, it can be understood that the 5 μm thick membrane which has the diameter size in the range of 100 - 200 μm with any metal combination

using appropriate thickness, gives result in desired pressure change (80 - 140 mmHg). In this context, mask drawing studies for microfabrication, focus on membranes with the diameter size in the range of 200 - 400 micrometers, which are likely to yield desired results.

4.4. Microfabrication of the Sensor

The fabrication process of the pressure sensor and the substrate of other sensors are realized with three masks and performed in the clean room located in Boğaziçi University, Center for Life Sciences and Technologies (LifeSci). The steps of the microfabrication process are shown in Figure 4.14

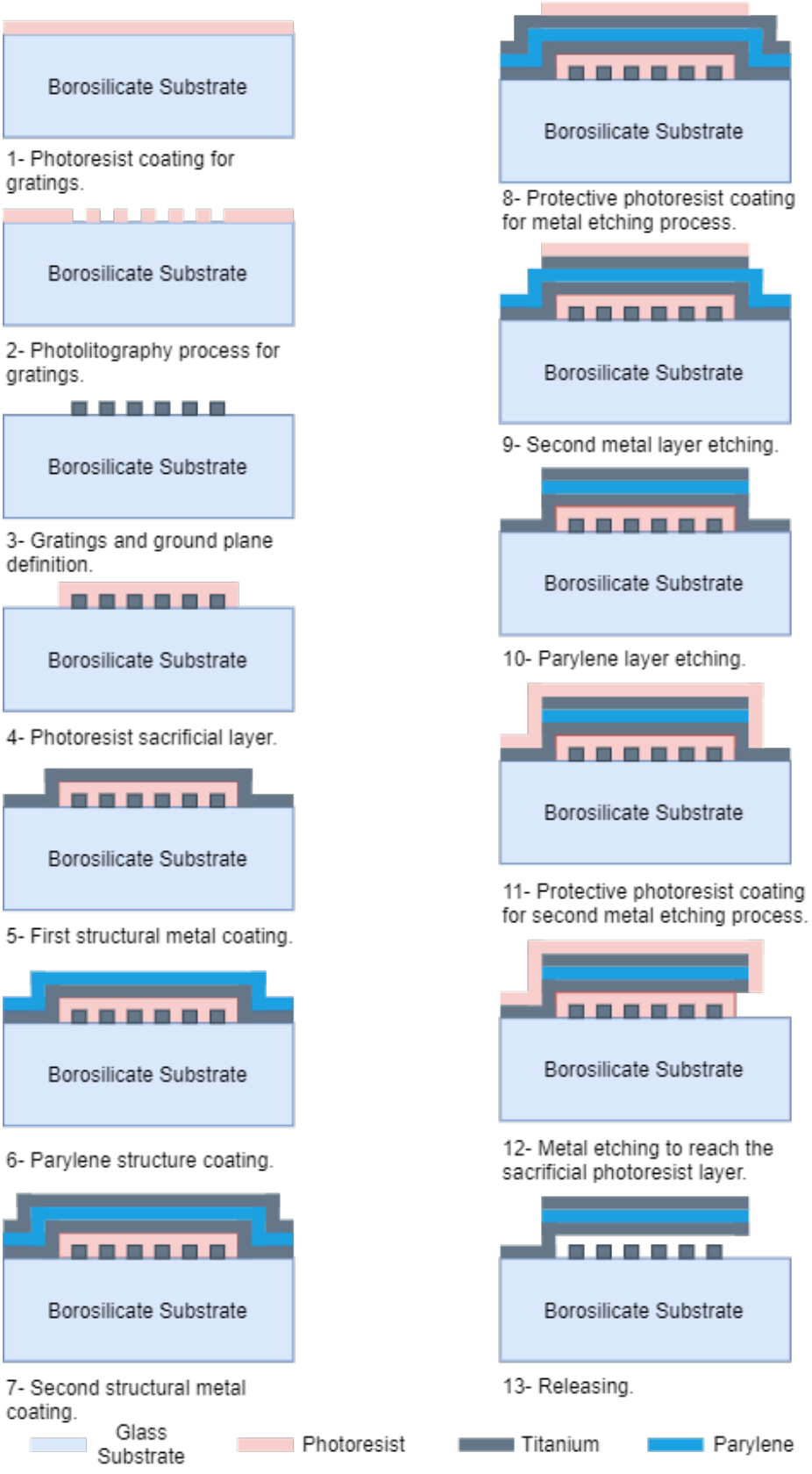

Figure 4.14. Process sequence of the microfabrication.

4.4.1. Mask Layout Design

Based on the design studies of pressure sensor with FEM software and obtained process sequence, 3 masks are drawn for microfabriaction of 100, 125, 150, 175 and 200 micrometer radius disc structures. Each chip is addressed with numbers and letters.

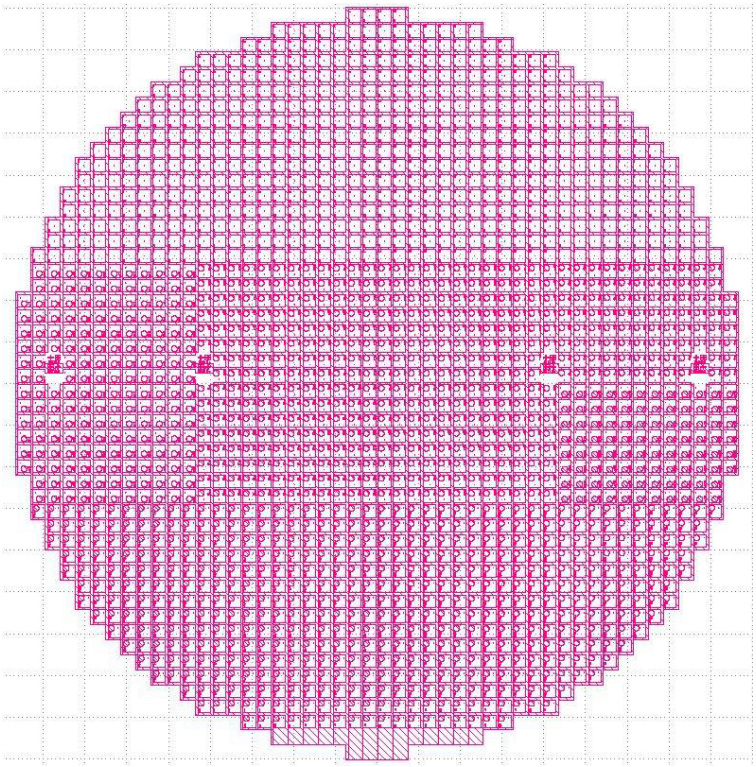

(a) Entire wafer.

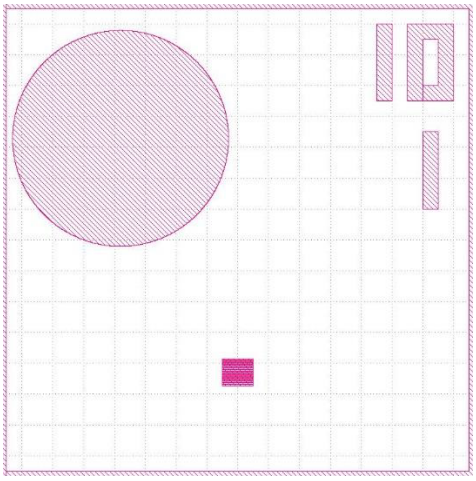

(b) Single chip.

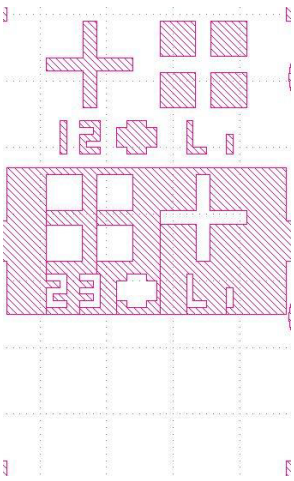

(c) Alignment markers.

Figure 4.15. Diffraction grating mask (Mask-1).

In the following step, structure of diffraction grating, which is going to be used in optical reading, is shaped with physical vapour deposition (PVD) method by using first photo mask (Mask-1). As it is shown in Figure 4.15, appropriate space for GaAs sample is shaped for temperature sensing in the same substrate.

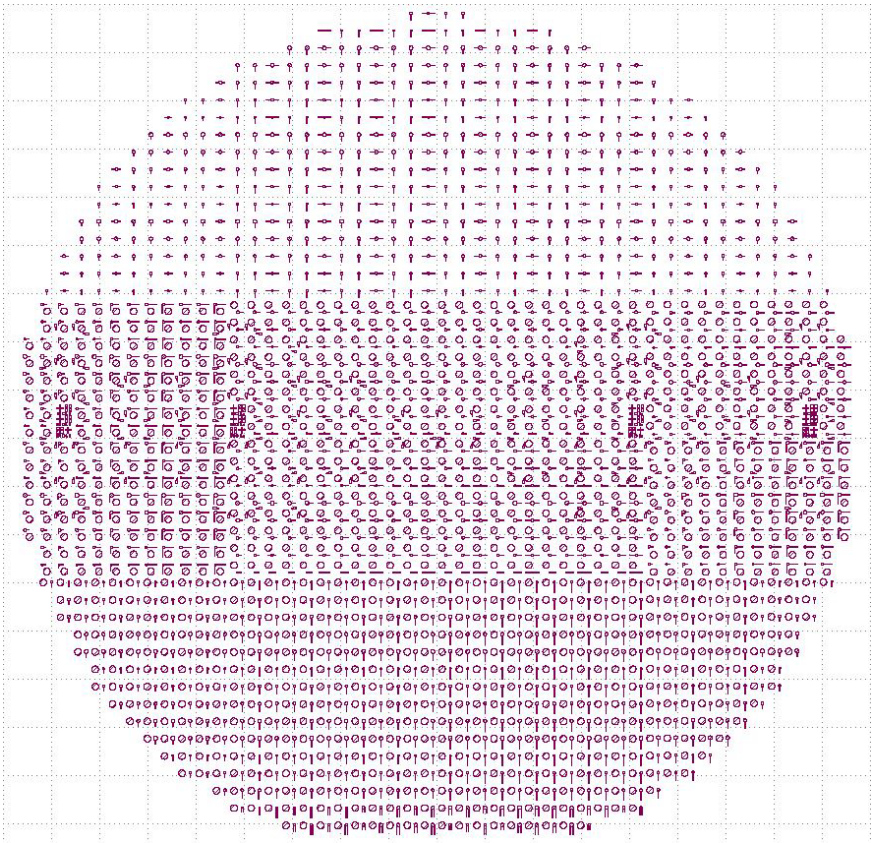

(a) Entire wafer.

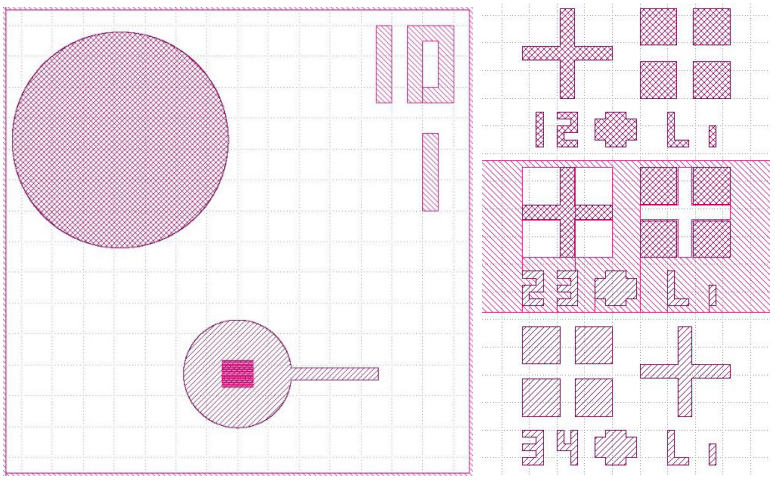

(b) Single chip. (c) Alignment markers.

Figure 4.16. Sacrificial layer mask (Mask-2).

In the next step, the photoresist sacrificial layer is shaped with Mask-2 (Figure 4.16). In this step, the first metal, then parylene and again metal layers are coated by physical and chemical vapor deposition (CVD). In this way, the sandwich structure is going to be shaped on sacrificial layer.

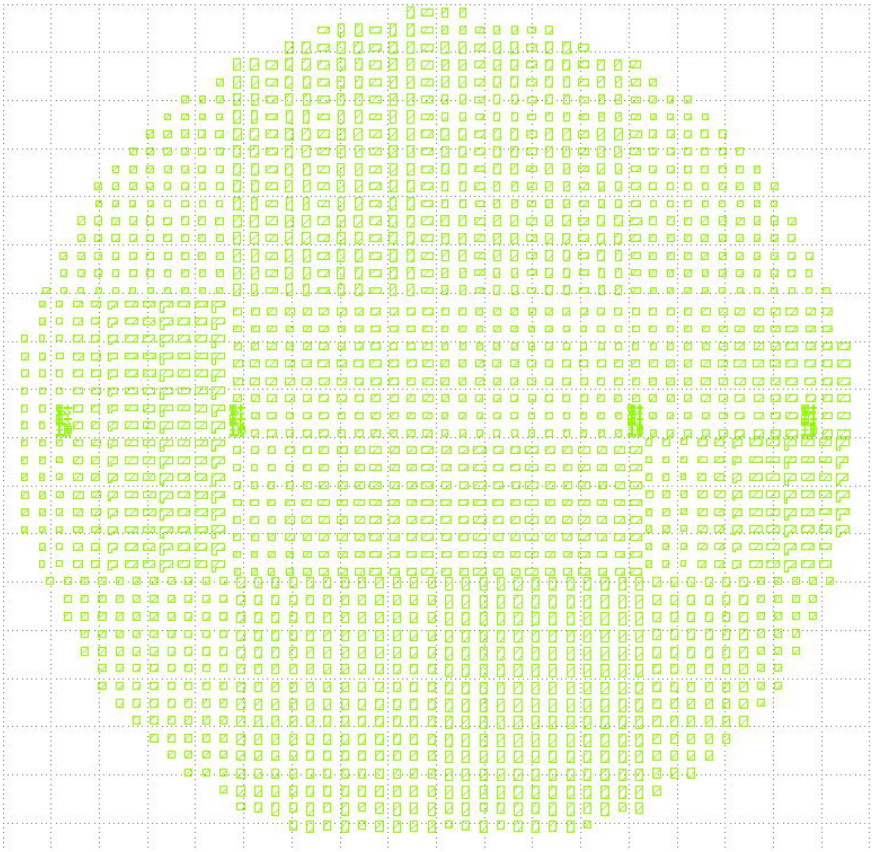

(a) Entire wafer.

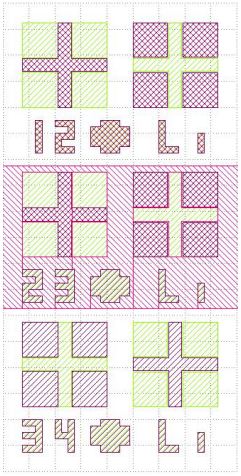

(b) Markers.

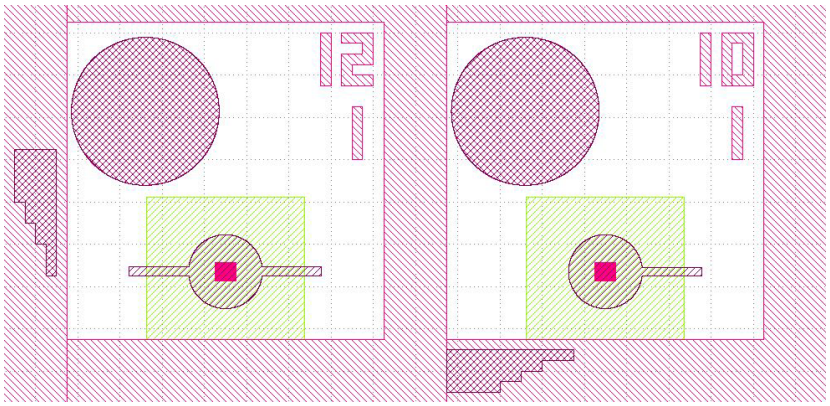

(c) Shape after process.

Figure 4.17. Protector mask for etching processes (Mask-3).

In the last stage, a small hole is vented into the pressure chamber by using Mask-3 (Figure 4.17). This hole is used in the sacrificial layer etching process. Finally, the chamber is sealed by dropping epoxy on the hole opened to create atmospheric pressure difference. To fabricate the targeted structures, mask designs are realized with L-Edit Layout Editor software and produced in the facilities of The Scientific and Technological Research Council of Turkey (TÜBİTAK) Informatics and Information Security Research Center (BİLGEM). Produced masks are shown in Figure 4.18.

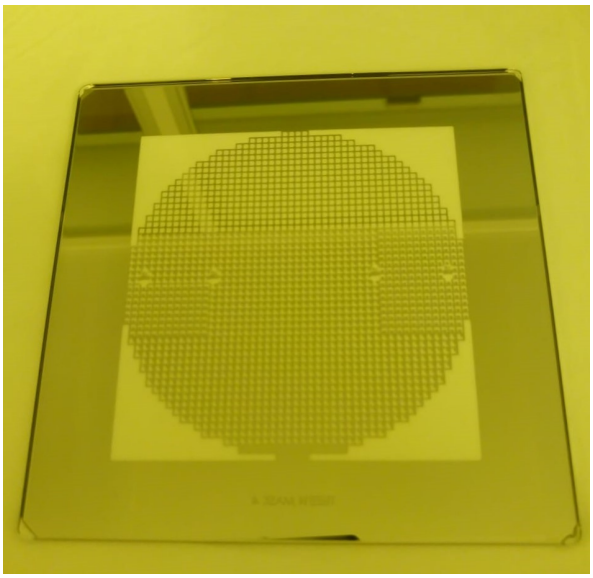

(a) Mask 1.

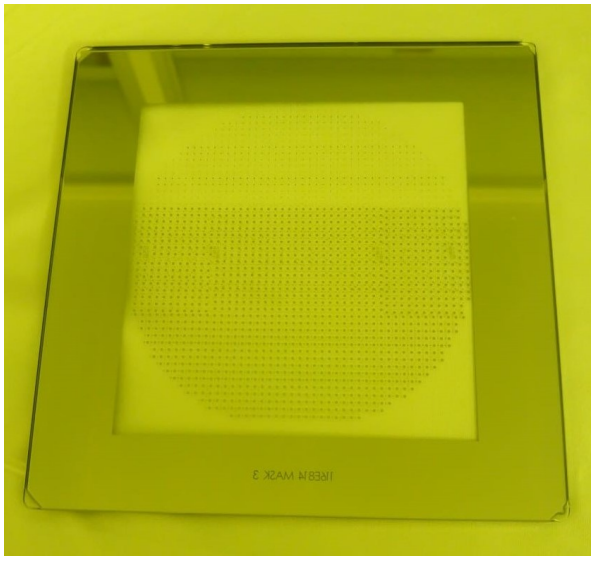

(b) Mask 2.

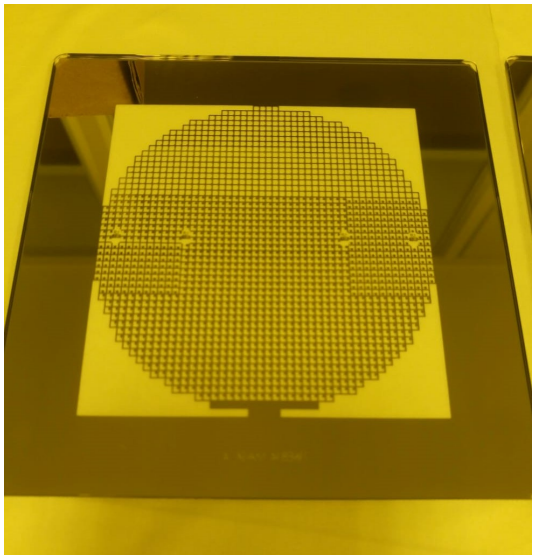

(c) Mask 3.

Figure 4.18. Printed masks.

4.4.2. Fabrication Process

The membrane being formed is built on a glass wafer since it will transmit data with light. As the way to obtain the relevant pressure value will be an interferometric method, process starts with shaping the diffraction grating on the glass wafer. The fabrication process starts with lithography. Firstly, to activate the surface, wafer is cleaned with a 1:20 diluted sulphuric acid (H_2SO_4) - water solution for 8-10 seconds. Cleaned wafer is diluted wit distilled (DI) water and dried with nitrogen gas (N). Then, by spin coating method, the wafer is coated with 1ml hexamethyldisilicate (HMDS) for 60 seconds at 6000 cycle/min, and surface activation is performed for photoresist coating. Subsequently, the surface is coated with 5ml of AZ5214E photoresist for 60 seconds at 3700 cycle/min. Coated wafer is heated on hot plate at 110 °C for 50 seconds, thus, a 1.8 micrometer thick layer is formed.

The photoresist-coated wafer is exposed to ultraviolet(UV) light using the EVG 620 Automated Mask Alignment System device and Mask-1. At this point, ultraviolet light is applied at the dosages of 40 mJ/cm^2, 60 mJ/cm^2 and 120 mJ/cm^2. It is observed that 120 mJ/cm^2 is the most appropriate amount for this step. Abraded structures after UV exposure are dissolved in 1:4 AZ400K developer - water solution for 50 seconds. Thus, the surface formed is become ready for metal coating for the diffraction grating to be used in the pressure sensor as shown in Figure 4.19.

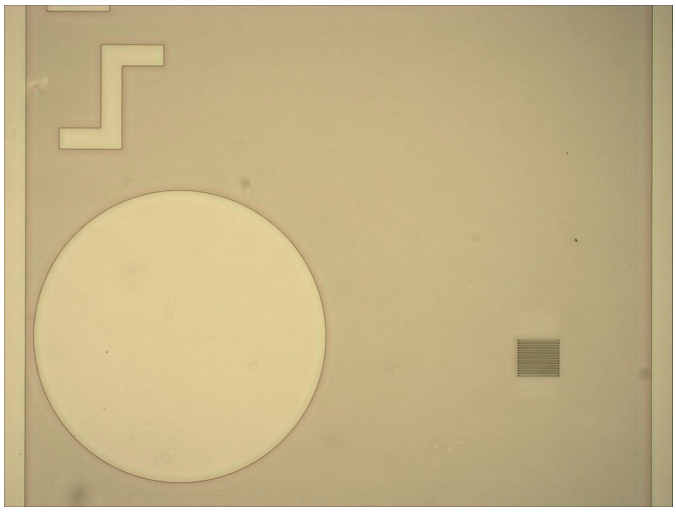

Figure 4.19. 5x magnified view of the unit chip.

As shown in the figure, an area with diameter of 700 μm is coated with photoresist to protect the place for the bonding of GaAs material to be used in the temperature sensing system. In addition, a 3 μm thick, 100 μm long photoresist diffraction gratings are created as a mask for metal coating (Figure 4.20).

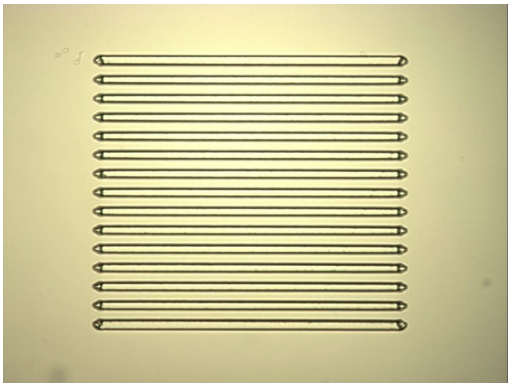

Figure 4.20. 25x magnified view of the photoresist diffraction grating.

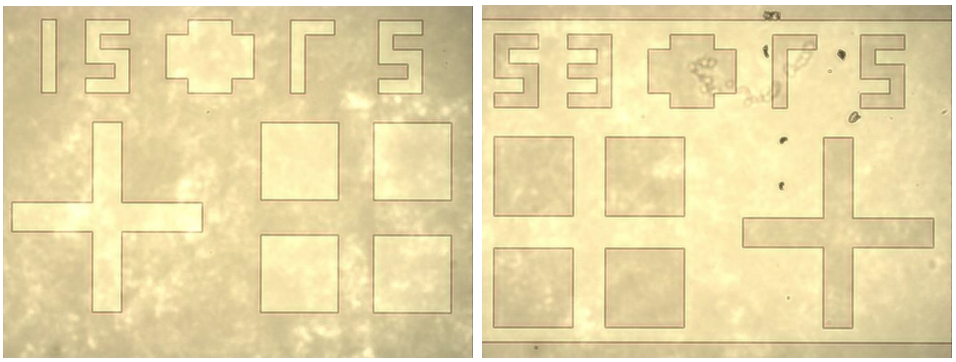

(a) Markers for 1st and 2nd masks. (b) Markers for 2nd and 3rd masks.

Figure 4.21. Alignment marks after 1st lithography.

The depths of the coated photoresist were measured by Bruker Dektak XT surface measurement microscope and the results are shown in Figure 4.22.

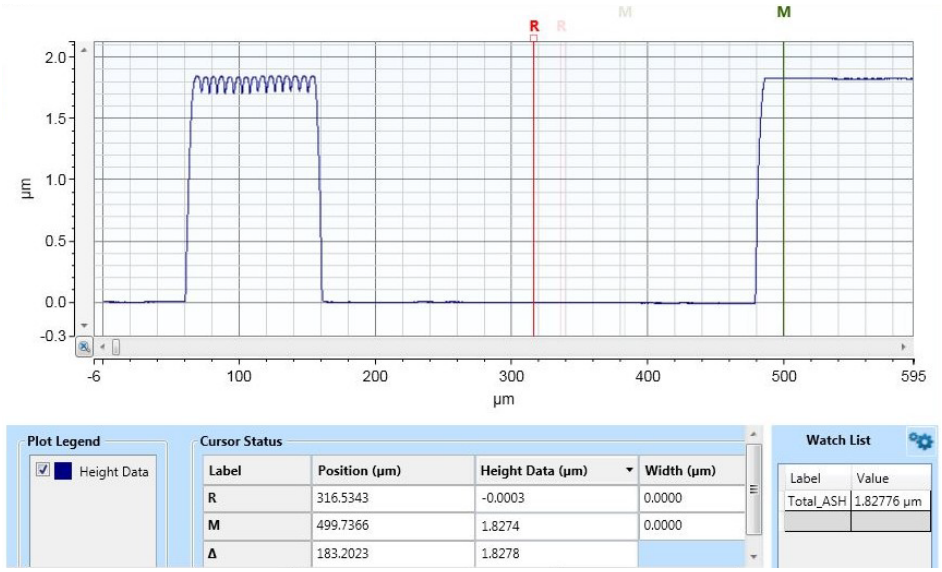

(a)

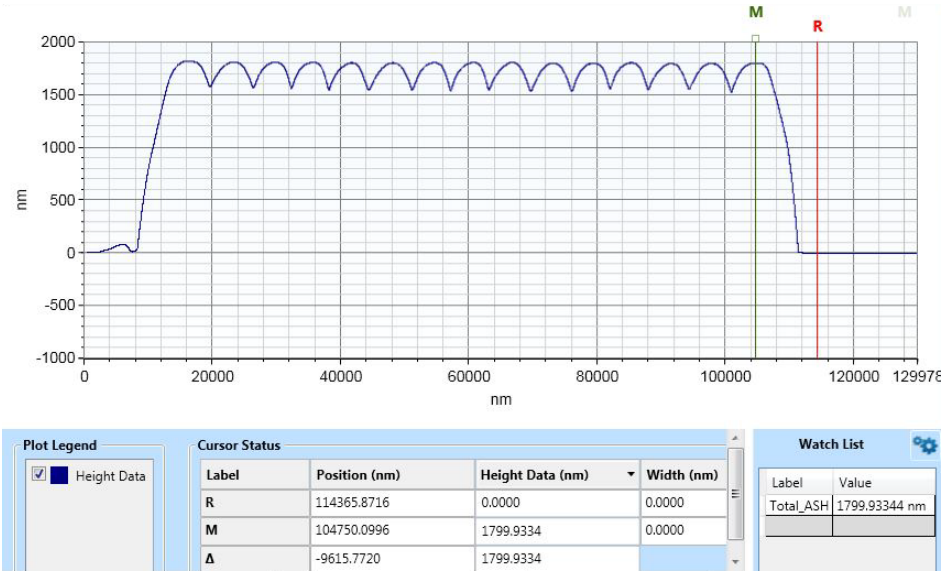

(b)

Figure 4.22. The depth of field where the materials to be used for (a) temperature sensor and (b) diffraction grating are protected.

As the second phase of fabrication, aluminum and titanium metal layers are coated trials on the photoresist structures. At this step, the Vaksis Angora Sputtering System device is used for metal coating. The process is carried out vacuuming the chamber for 24 hours and continued by applying 100 watt DC power to the target in the chamber. In this way, structures on the wafer are coated by 120 nanometer and

150 nanometer thick aluminium and titanium metals respectively in approximately 15 minutes. Coating thicknesses are presented in Figure 4.23

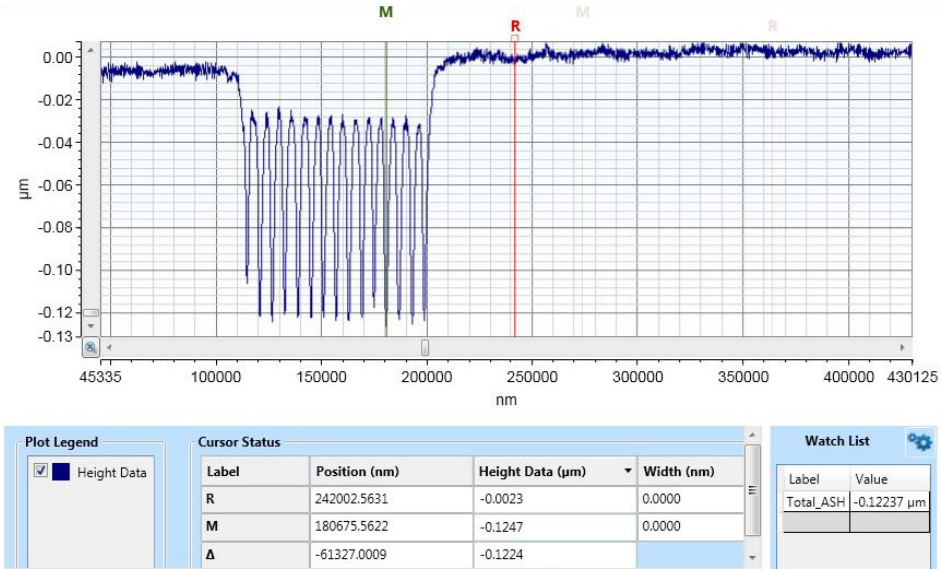

(a) Thickness of coated Aluminium on gratings.

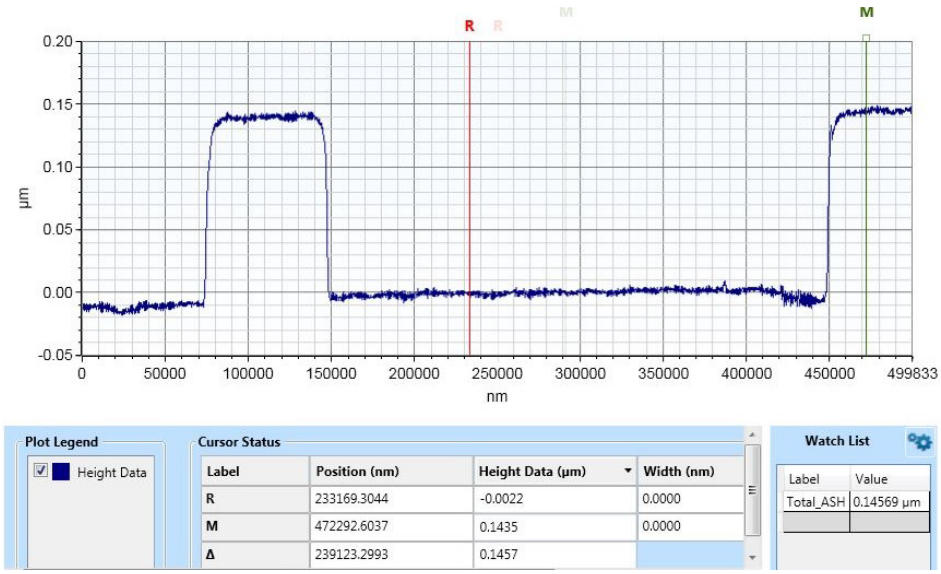

(b) Thickness of coated Titanium on gratings.

Figure 4.23. Thickness of the coated metal layers.

After the metal deposition, process continued with photoresist removal. At this stage, photoresist removed by keeping the wafer inside the acetone at 45 °C for 10 minutes. Thus, the unwanted metal coating on the surface is removed from the wafer by removing the photoresist layer underneath. Microscopic images of the unit chip

and diffraction gratings are shown in Figure 4.24 and Figure 4.25. Thus, the first lithography stage and metal coating trials in forming the diffraction gratings were successfully completed.

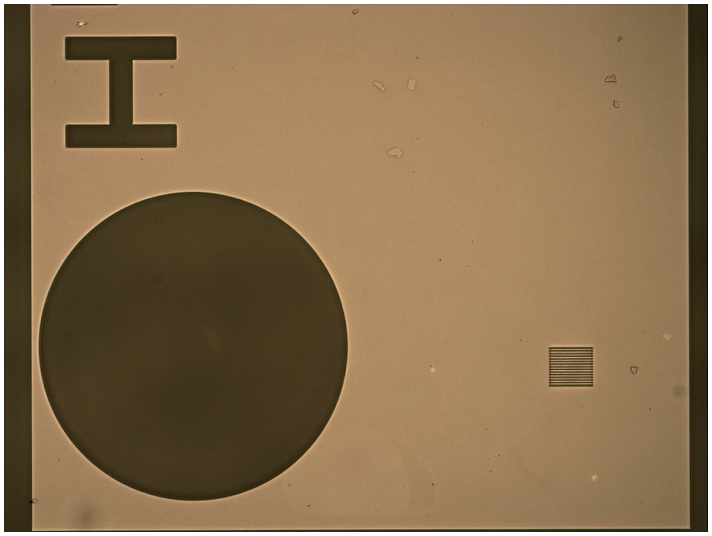

Figure 4.24. 5x magnified view of the metal coated unit chip.

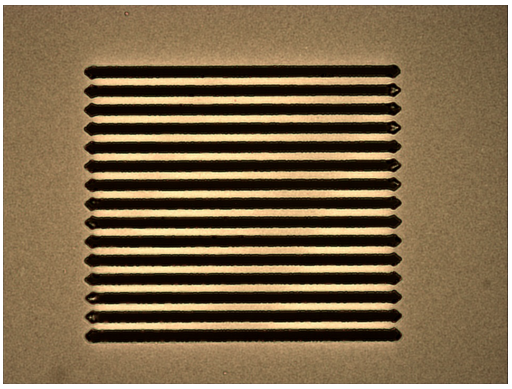

Figure 4.25. 25x magnified view of the metal coated diffraction gratings.

The next step is the fabrication phase of the chamber required for the pressure sensor to be formed to act as a membrane. The method to be followed in this direction is to create the sacrificial layer, which will be abraded later, by coating photoresist with the necessary lithography process. At this point, once again, 1 ml of HMDS is coated with 6000 min/cycle for 60 seconds by spin coating method on the wafer, and surface activation is performed for photoresist coating. The surface is then coated

with AZ5214E photoresist for 60 seconds at 1100 revolutions per minute (rpm) to form a sacrificial layer of approximately 3.7 micrometers. The plate is then placed on 110°C heating plate for 60 seconds. Thus, photoresist is hardened o nthe surface. The photoresist-coated chip is exposed to ultraviolet light using Mask 2 with the EVG620 Mask Alignment device. The dosage of 120mJ/cm^2 UV light is applied on the wafer. After UV exposure, eroded photoresist layer is dissolved in 1:4 AZ400K developer - water solution for 50 seconds. Thus, the chamber to be used in the pressure sensor has been made ready as shown in Figure 4.26.

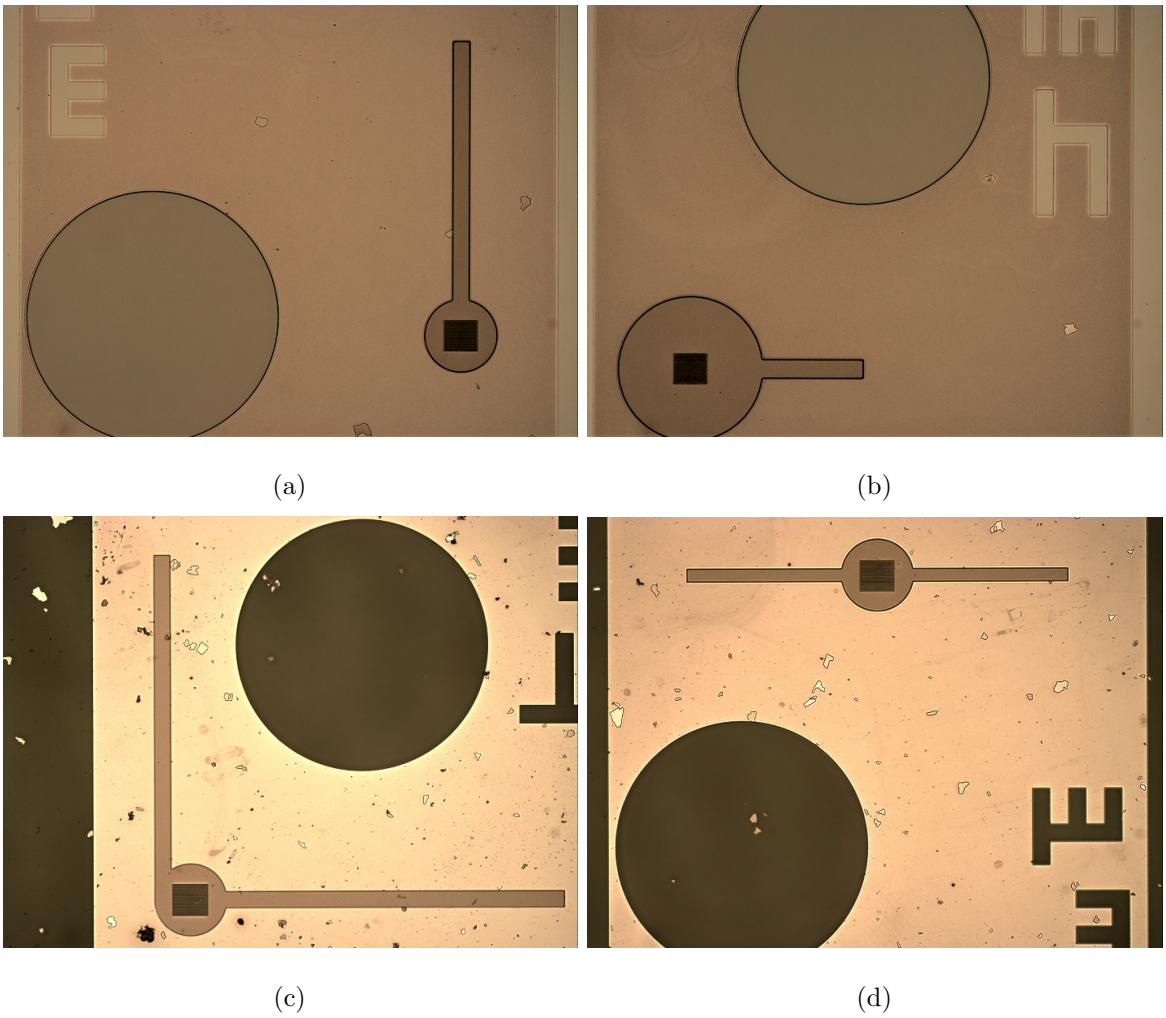

(a) (b)

(c) (d)

Figure 4.26. 5x magnified different sample views of the sacrificial layer coated unit chips.

Based on the simulations performed, the lengths of the paths, which are used to reach the sacrificial layer during the etching process, are designed in different values.

At the same time, the sensor circle membrane structures designed as 200 micrometers, 250 micrometers, 300 micrometers, 350 micrometers and 400 micrometers in diameters are shown in Figure 4.27 and Figure 4.28. Also, the thickness of the coated photoresist is shown in Figure 4.29

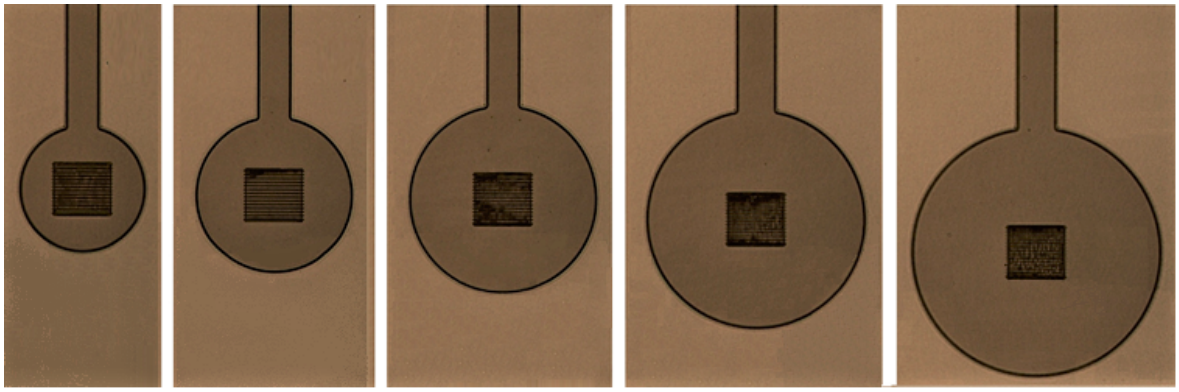

Figure 4.27. Sacrificial photoresist layer views for different membranes. (a)200 μm, (b)250 μm, (c)300 μm, (d)350 μm, (e)400 μm.

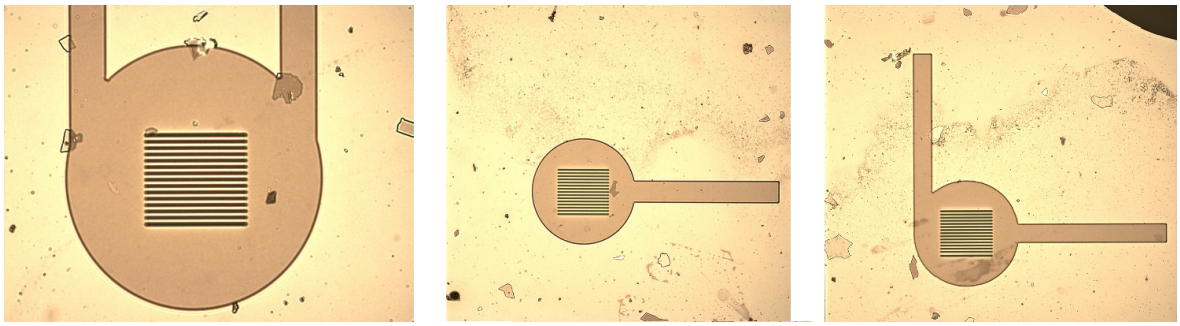

Figure 4.28. Designed paths to reach the sacrificial photoresist layer.

Thus, necessary preparations have been completed for the void area where the required bending movement will take place after the etching process of the membrane structure to be formed.

The next step is the fabrication of the pressure sensing membrane structure whose motion is desired. The way to follow in this direction is the multi-layer coating method. On the sacrificial layer, firstly, thin film metal coating process is carried out to reflect

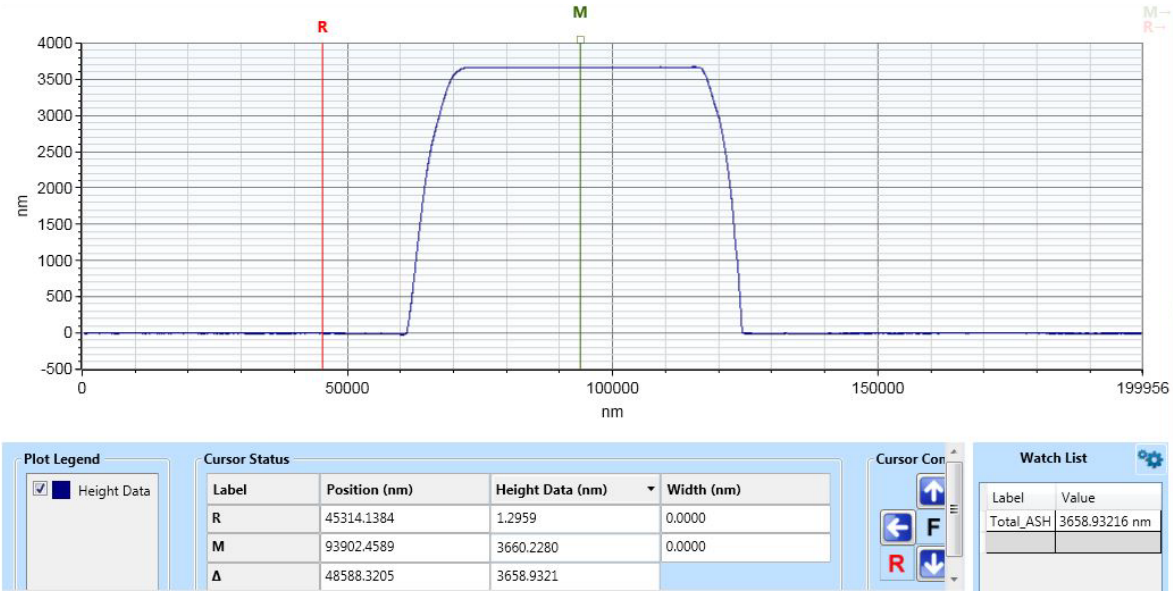

Figure 4.29. Thickness of the sacrificial layer photoresist.

the light from which data transfer will be made. This process is realized with PVD sputter device. The process is carried out by keeping the chamber, which contains wafer inside, in vacuum for 24 hours. Afterwards, wafer coated with applying 100 W DC power to the target for 75 minutes. As a result, different wafer surfaces are coated approximately 300 nanometers and 350 nanometers of aluminium and titanium respectively as a lower metal layer. Microscope images of the wafers after coating are shown in Figure 4.30.

Thus, the first stage of the multilayer coating process of the membrane structure has been completed. The next step is to adapt the flexibility of the desired membrane structure to the desired pressure values, ie blood pressure values. Based on the data obtained from the simulation studies, the coating of Parylene-C polymer material as 5 μm shows that the structure has reached the optimized value. This process starts with loading the desired amount of polymer material to the loading boat in the parylene-C coating device according to the desired thickness. The powder form Parylene-C is heated until it is brought to 150 °C temperature value. The steam formed here is drawn into the furnace under a certain pressure value, where it is heated up to a temperature of 690 °C and sublimation of the material causes its molecules to separate into its

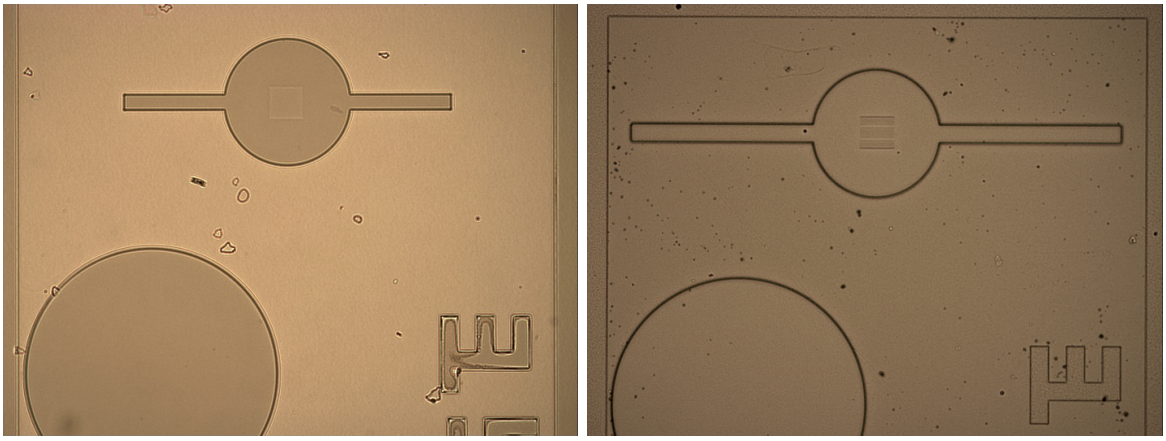

(a) Aluminium coating. (b) Titanium coating.

Figure 4.30. Lower metal coating of the membrane structure.

monomers. This gas, which contains monomers, is drawn into the chamber where the coating is to be made. As the last step, a sudden cooling process is performed and the monomers are polymerized again in the coating chamber. At this stage, the Parylene-C layer become coated on the wafer in a controlled and homogeneous manner. In the coating trials carried out for the targeted thickness of 5 μm, it is determined that 7.25 mg of Parylene-C dimer material is sufficient. In order to make optimization studies, 4.75 μm and 5.25 μm thick polymer coating studies were also carried out. The images of the Parylene-C coated surfaces are shown in Figure 4.31.

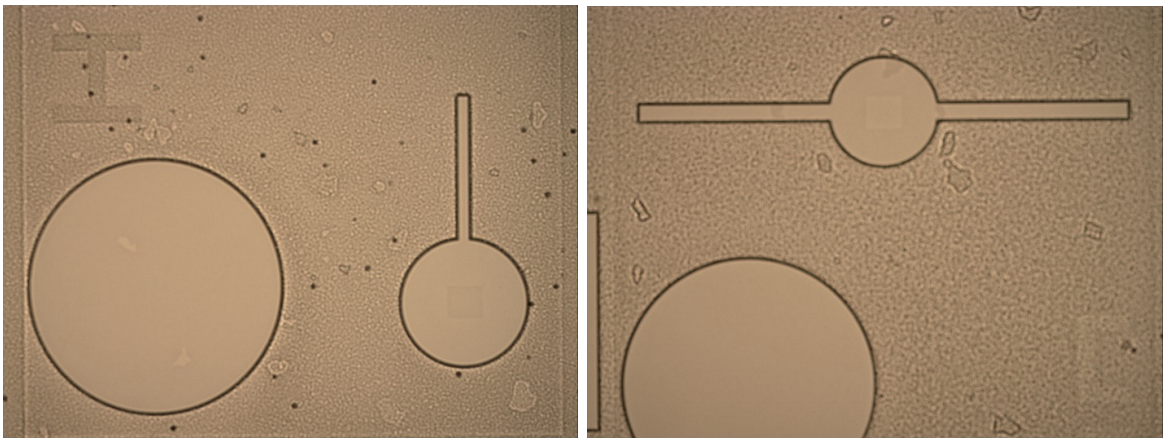

Figure 4.31. Microscope image of the surface coated with Parylene-C material.

The coated polymer layer was measured by Bruker Dektak XT surface measurement microscope and the results are shown in Figure 4.32.

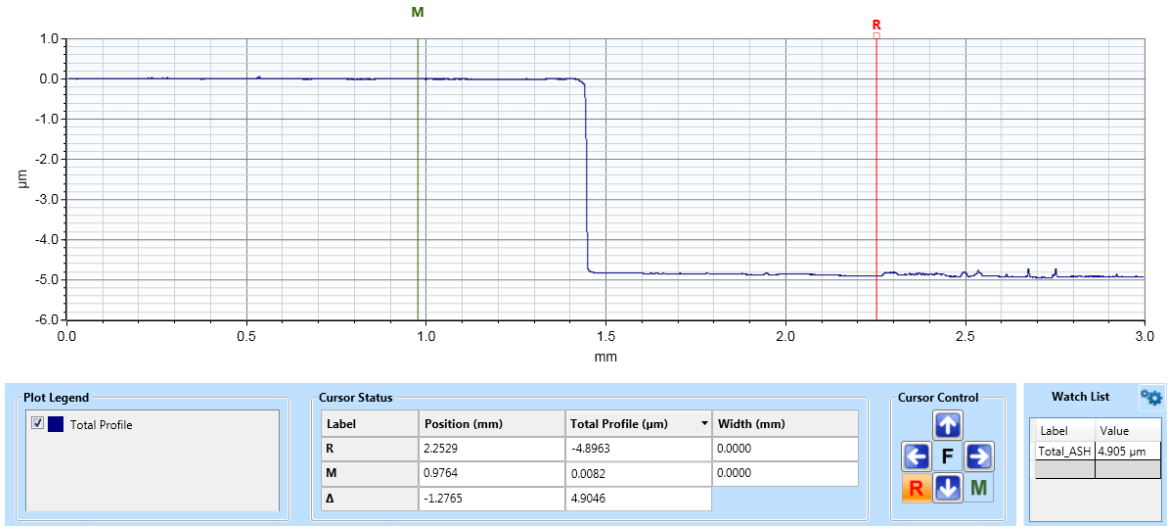

Figure 4.32. Thickness measurement of Parylene-C polymer coated on the surface.

The flexibility coefficient of the membrane structure has been optimized in a way that it can act in accordance with the changes in blood pressure values with the polymer material used. The next step is upper metal coating, which is the last layer of the sandwich structure membrane. The purpose of the final metal coating is to prevent the membrane structure from going beyond the desired expansion values due to the thermal expansion on the membrane. At the same time, due to the pressure difference in between the chamber and environment, a bend will occur on the membrane. Additionally, the top layer metal is also fix the unwanted bending in a mechanically convenient condition. This layer must therefore be thicker than the substrate metal of the multilayer membrane structure.

At this fabrication stage, metal plating process, PVD sputtering device is used again. As it is applied for other metal layers, the wafer kept into the chamber for 24 hours and 420 nm and 480 nm of aluminium and titanium metals are coated in 87 minutes and 95 minutes respectively. The metal coated surfaces are presented in Figure 4.33.

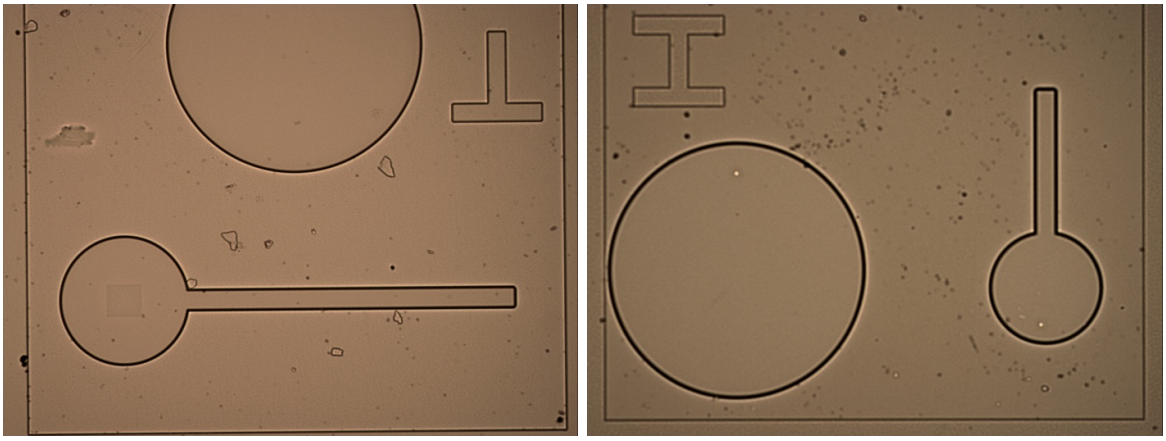

(a) Aluminium coating. (b) Titanium coating.

Figure 4.33. Upper metal coating of the membrane structure.

Thus, a structure that can bend sufficiently at blood pressure values (60-140 mmHg), which is aimed to be measured, is formed. With this bending, the structure where interferometric measurements can be performed based on the reflection of the light falling on the lower metal layer is built.

In the next phase, works focused on the release of the designed membrane with the steps shown. The multi-layer structure, which is homogeneously coated on the entire surface, should only be actively functional for the designed membrane structure. For this reason, the sequential solving processes of the multi-layer structure are carried out. In this direction, the layer needed to be etched in the first stage is the thick metal layer at the top of the membrane structure. In order not to damage the membranes from this dissolution process, a lithography process is used.

At this point, photoresist coating is applied on the thick metal surface. In the following stages, it is deemed appropriate to cover the photoresist material as a thick layer to protect the Parylene-C membrane structure, since the etching rates of photoresist and Parylene-c are nearly the same. Accordingly, the surface is coated with 5 ml of AZ4533 positive photoresist material at 2000 rpm for 60 seconds, and an 8.8 μm thick layer is formed. During the cooking phase of the photoresist, the hotplate is set to 50 °C in order not to effect the Parylene-C structure in the membrane and wafer is

kept there for 70 seconds. Thus, the photoresist layer is hardened on the surface. The photoresist coated wafer is exposed to UV light using third mask with the EVG620 mask aligner. Since the coated photoresist layer is thick, UV light is applied at the energy rate of 600 mJ/cm^{-2} and it is observed as a suitable amount for this step. Unused structures are bathed with 1:4 dilution of AZ400K developer-water solution for 70 seconds. Consequently, the formed surface has been made convenient to etch the upper layer metal with a suitable acid solution. However, at the cleaning step of the photoresist with developer solution, it is observed that aluminium coated wafers are corroded as developer contains a potassium based chemical component and rendered the structures unusable. Thus, etching process is held with titanium coated wafers after this point. The titanium coated wafers microscopic images are presented in Figure 4.34. The coated photoresist layer is measured with Bruker Dektak XT surface measurement microscope and the results are shown in Figure 4.35.

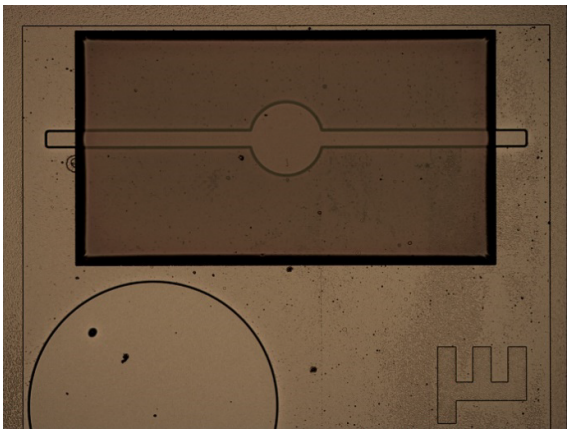

(a) Unit chip with two etching paths.

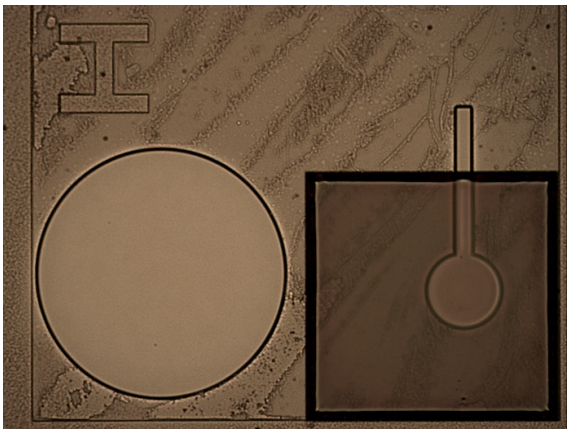

(b) Unit chip with one etching path.

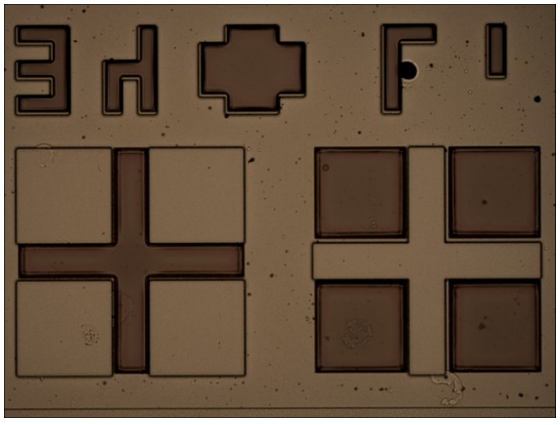

(c) Alignment markers.

Figure 4.34. Microscopic view of the photoresist layer used for metal etching process.

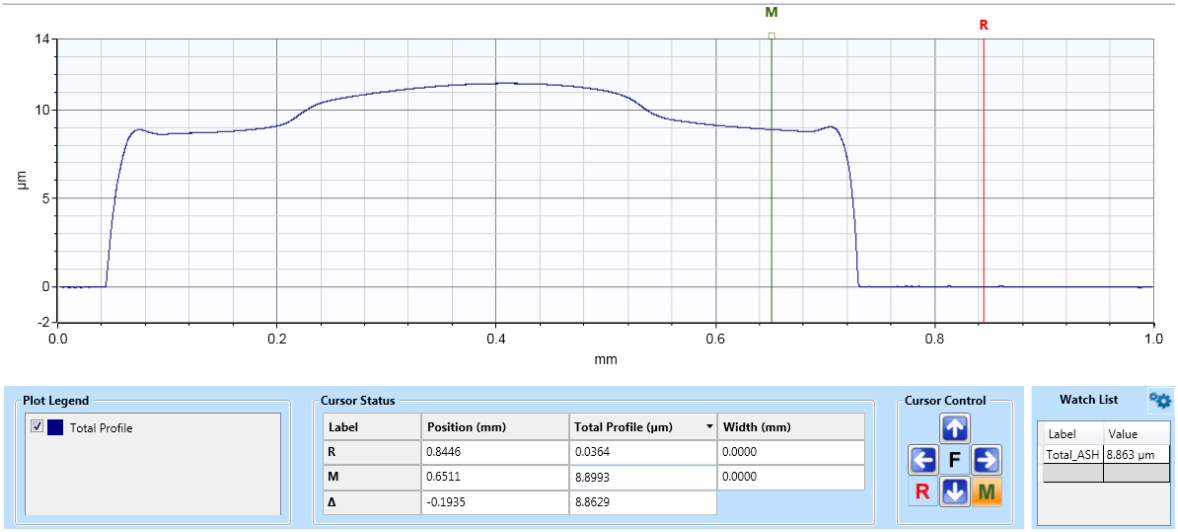

Figure 4.35. Thickness measurement of photoresist on the upper metal layer.

Thus, the wafers are ready for the necessary etching processes to reach the sacrificial layer. For this process, firstly, the upper layer of the sandwich structure is etched. Since the coated metal on this layer is titanium, the solvent to be used is a hydrogen fluoride acid (HF) solution. To use the acid properly, solution is prepared as 1:10 HF-water mixture. As HF is a strong acid, upper titanium layer is etched in a plastic container for 35 seconds. As HF is not harmful for plastic and polymer materials, Parylene-C layer escape damage during this process. Etched surface shapes are shown in Figure 4.36. Accordingly, the etched metal layer thickness is measured with Bruker Dektak XT surface measurement microscope and the results are shown in Figure 4.37.

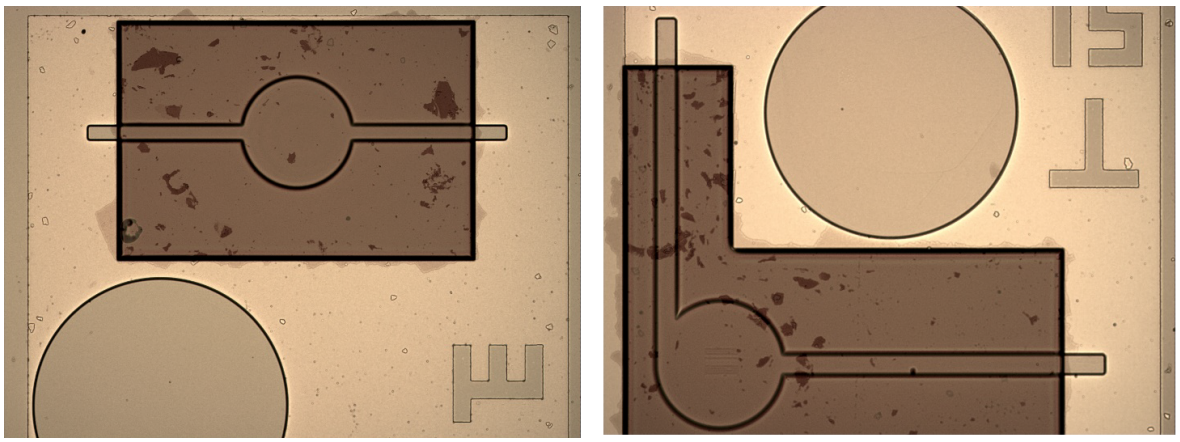

Figure 4.36. Surface shape after upper titanium layer is etched.

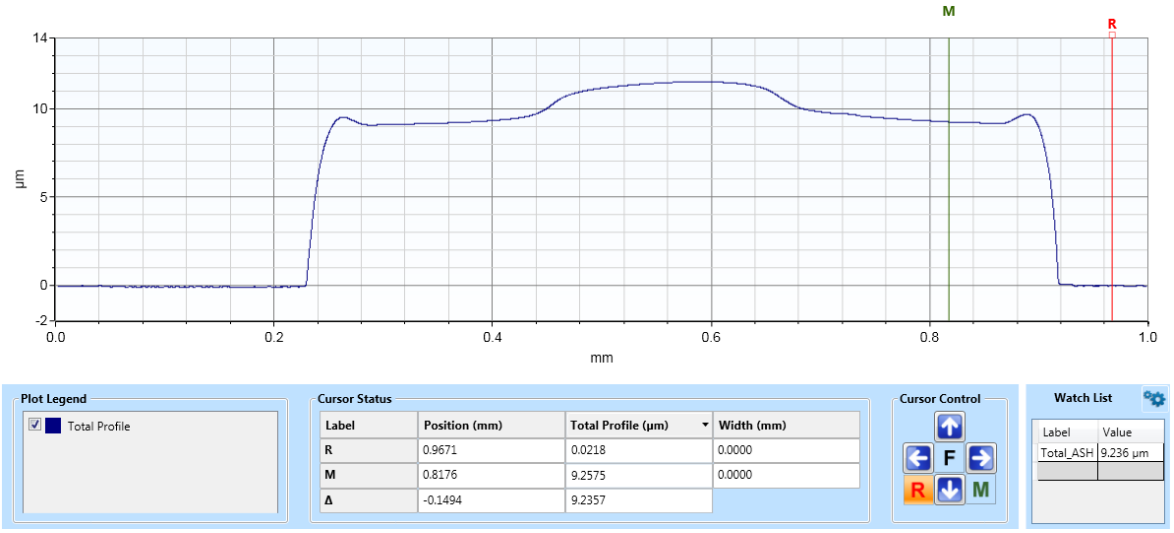

Figure 4.37. Measurement thickness of the surface after titanium layer is etched.

Hereby, it has been shown that the hydrofluoric acid solution does not damage the photoresist layer and the coated (and dissolved) titanium metal thickness is approximately 500 nm as can be seen the difference in Figure 4.35 and Figure 4.37.

The next step to reach the sacrificial layer is the etching of the Parylene-C layer. This process is realized in the Nordson March AP-300 RF Plasma Processing device by using oxygen plasma. Here, the shaped photoresist and metal layers on the membrane are acting as a mask that prevents the etching of the Parylene-C in sandwich structure. Process is carried out with 150 W RF power, 180-200mbarr pressure range and 100 sccm oxygen flow rate for 45 minutes. Thus, the unused Parylene-C material with a thickness of 5 μm on the surface is dissolved. Post process surface shapes are given in Figure 4.38.

The thickness is measured based on the difference in between the bottom metal layer on the substrate and upper titanium layers on the mambrane. At this point, it is observed that photoresist with a thickness of approximately 2 μm remains on the membrane.

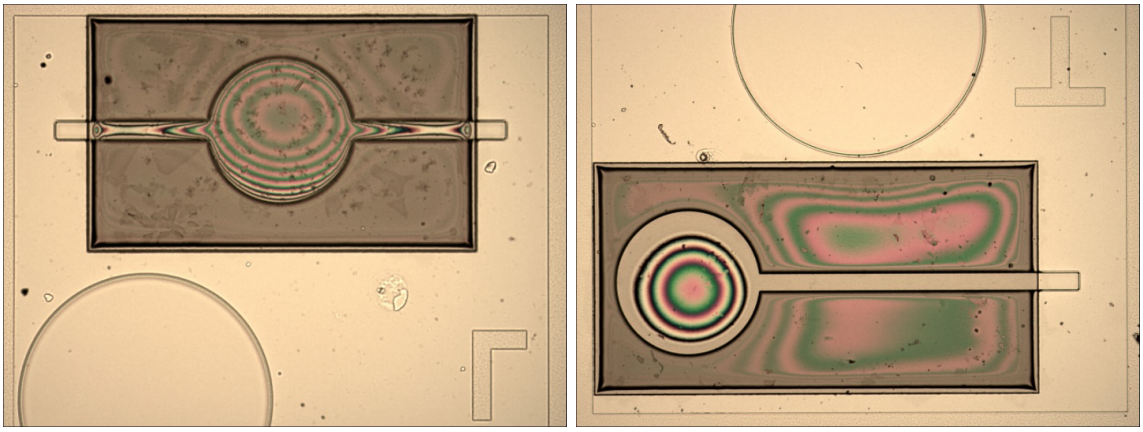

Figure 4.38. Surface structures after Parylene-C etching process.

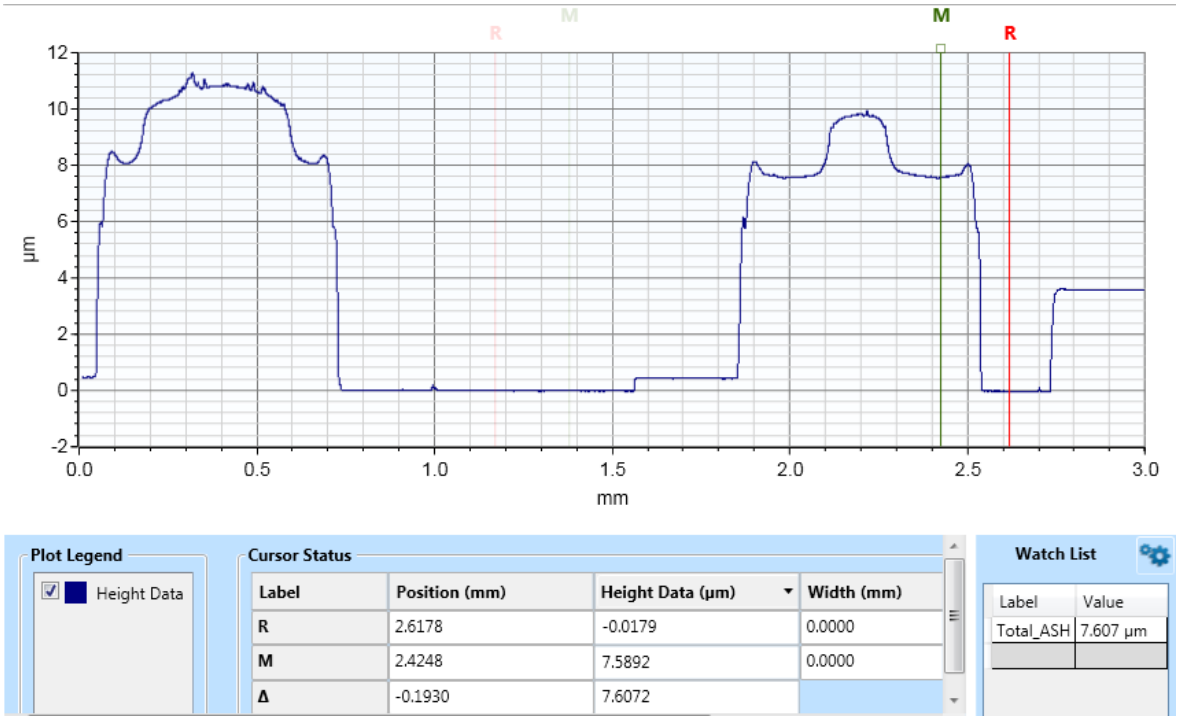

Figure 4.39. Measurement thickness of the surface after parylene layer is etched.

To reach the sacrificial layer, there is needed a final metal etching process. However, as it can be seen in the figures, in the Parylene-C etching process, the photoresist layer did not stripped out homogeneously and therefore, to protect the upper layer titanium metal, it become necessary to repeat the lithography step with mask-3. After the repetition of the lithography process, surface has been made suitable to etch the

bottom layer titanium with a suitable acid solution.

As a last step to reach the sacrificial layer, the non-functional regions of the bottom layer titanium metal is etched with using photoresist. A 1:10 HF-water solution is prepared again and the wafers are kept in the solution for 25 seconds as the layer is thinner than the upper one. Since the solution only corroded the metal, the photoresist coated on the chip helped protect the top layer of titanium and bottom titanium layer is etched successfully. The condition of the wafer after the last etching process is presented in Figure 4.40.

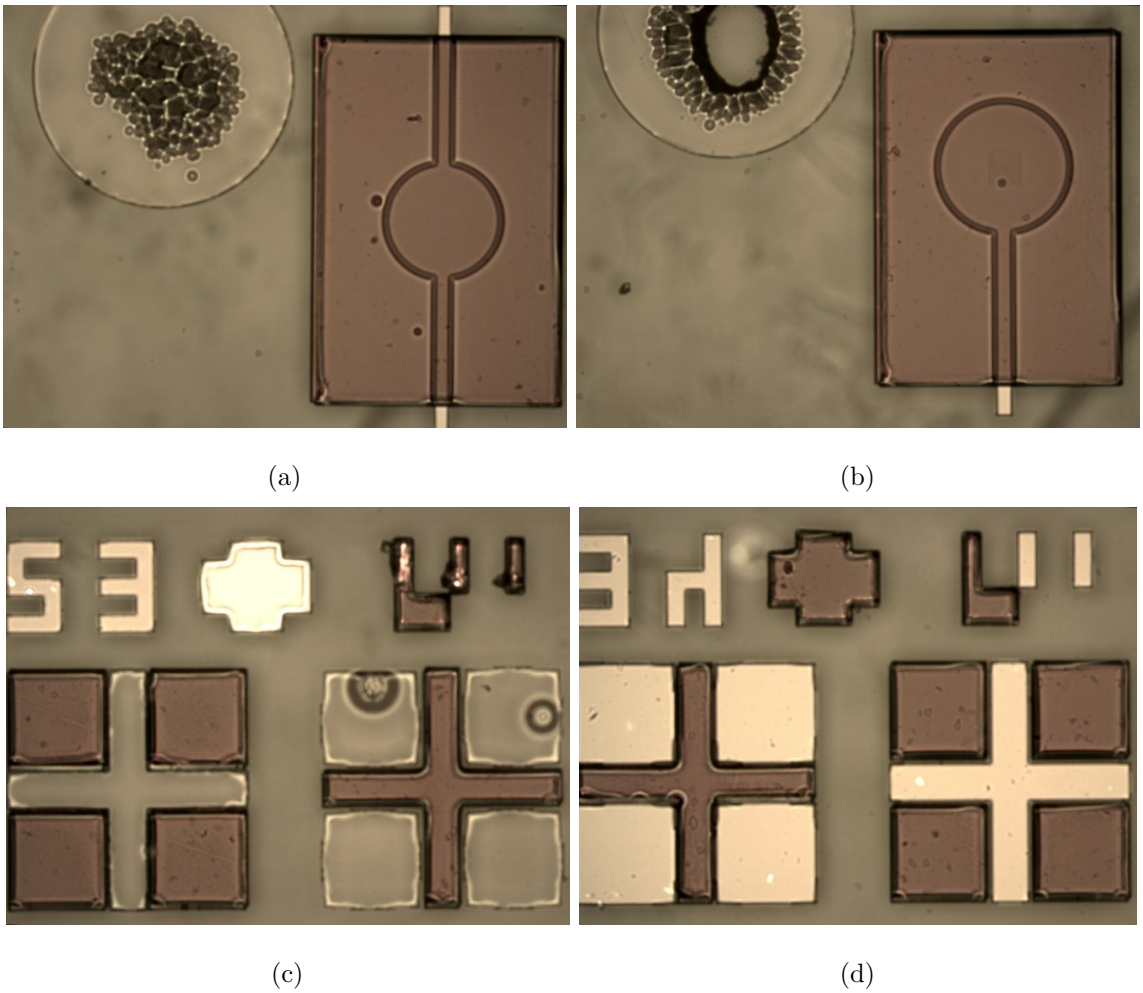

(a) (b)

(c) (d)

Figure 4.40. The production of the multilayer membrane structure is completed (a), (b) The image of the unit chips, (c), (d) the image of the alignment markers.

To characterize and to make available chips for aimed applications, wafers are diced as 6x6 arrays (Figure 4.41.a) and as single chip (Figure 4.41.b) size of 2.2 mm^2 at Sabancı University Nanotechnology Research and Application Center (SUNUM) with DISCO DAD 320 Automatic Dicing Saw.

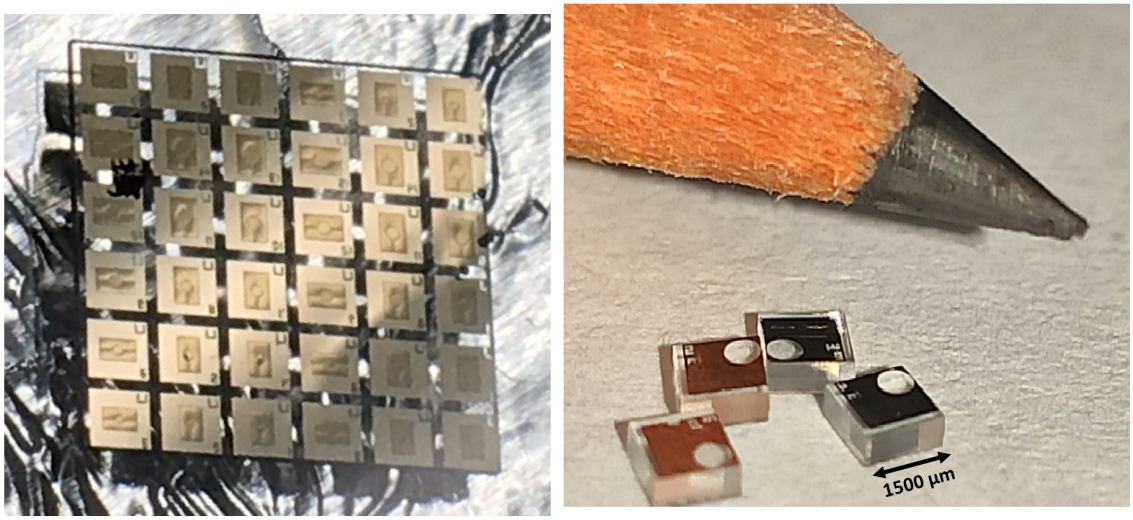

(a) Array of 6x6 single chips.

(b) Diced single chips.

Figure 4.41. Diced fabricated chips.

To etch the sacrificial photoresist layer, some methods are tried. To make it faster, first trials are realized with agitating the samples in sonicator. It is observed that, using ultrasound homogenizer sonicator are pulling off all the membranes from substrate even in 2 minutes. Alternatively, as a long way, chips are kept in acetone in between 24 hours and 120 hours. According to these trials, it is observed that keeping structures inside acetone for 36 hours is the most suitable method for releasing process of the membrane. To create a chamber under the membrane and making available sensors to detect the pressure change, cylindrical shaped chambers are sealed with a metal adhesive epoxy from the paths and the metal layer from edges.

To characterize the sensor, a fully sealed closed system is designed. To illuminate gratings and membrane, chips are sealed on a lamellae and this thin glass is sealed with a chamber. Then, created chamber is connected to a manometer and a manual air pump as shown in Figure 4.42.

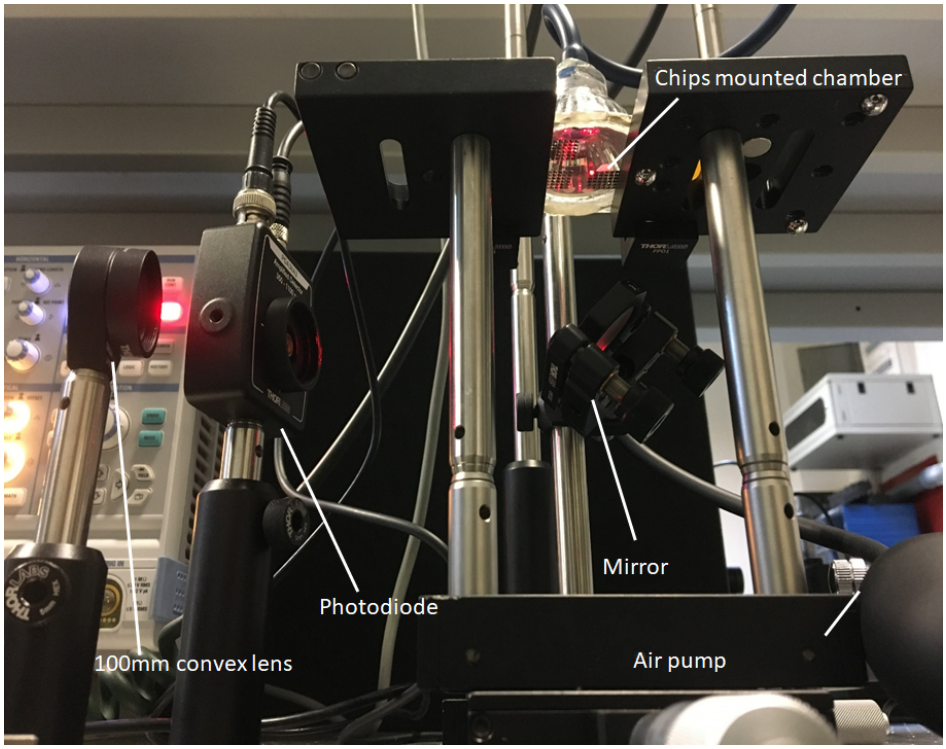

(a) Detailed image of chamber.

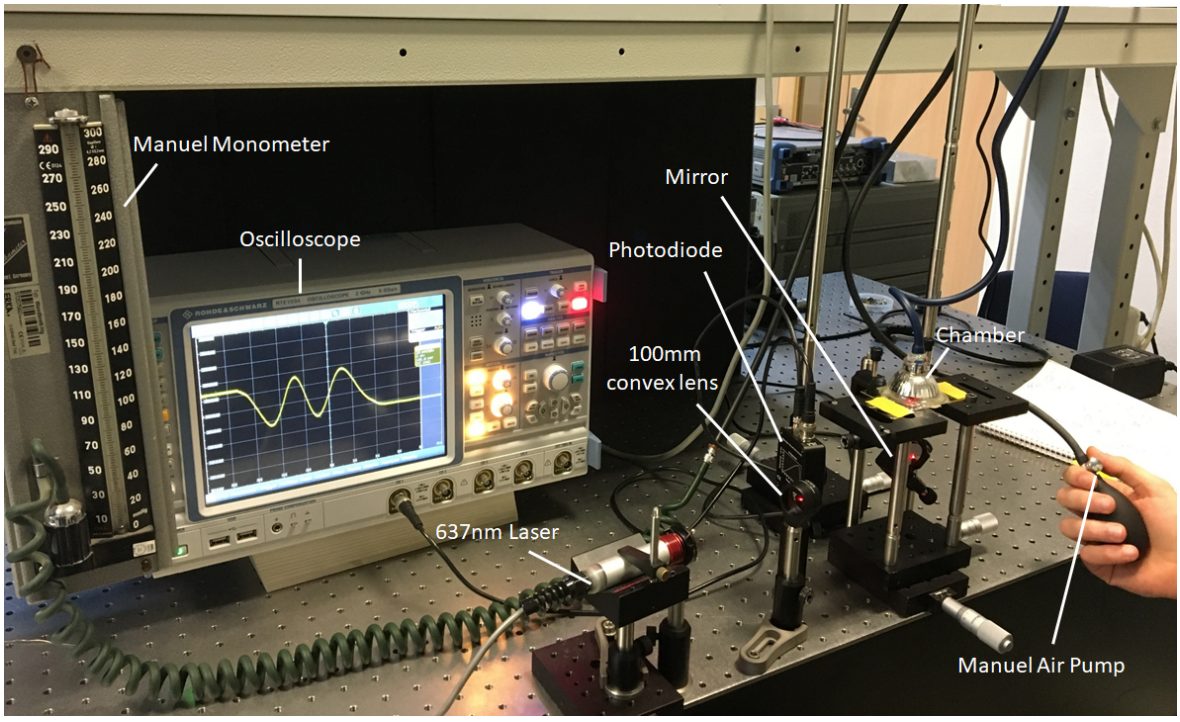

(b) Installed system.

Figure 4.42. Experimental setup for pressure sensor characterization.

As it can be seen in Figure 4.42, light beam from the laser source is trimmed with an optical diaphragm to get rid of the unwanted shapes of the beam. Then, beam size of a 637 nm laser ray is is collimated with a 100mm focal length convex lens. By using a mirror in 45°, minimized beam is coupled to the phase sensitive diffraction grating after passing through a transparent thin layer coverglass of the chamber and the quartz substrate. Light beam is passed through the gratings and reflected back from the titanium coated membrane. The first order diffracted beam is then detected using Thorlabs PDA-36A2 Amplified Detector at 40 dB gain and oscilloscope.

Presented sensor demonstrates a 2-λ readout method to improve sensitivity. According to theory, one full sinusoidal oscillation of a reflected light wave from the sensor, corresponds the displacement of the membrane as the same size of the wavelength of the illuminated light. As the system has a reflected surface membrane, due to the superposition theory of interference, two full sinusoidal oscillations of a reflected light become the same λ difference change of the wavelength of the light. The simulation and experimental measurement results of 200 μm, 250 μm, 300 μm, 350 μm, 400 μm diameter membranes are given in Figure 4.43, 4.44, 4.45, 4.46, 4.47.

As simulation parameters, the chamber pressure is kept as 1 atm which is equal to 760 mmHg. To simulate the blood pressure, the environmental pressure parameter is applied as 925 and 1010 mmHg which corresponds 165-250 mmHg blood pressure levels. Also, the simulations are made for half of the membrane, that's why, plotted graphs show the difference in between the middle and edge of the membrane.

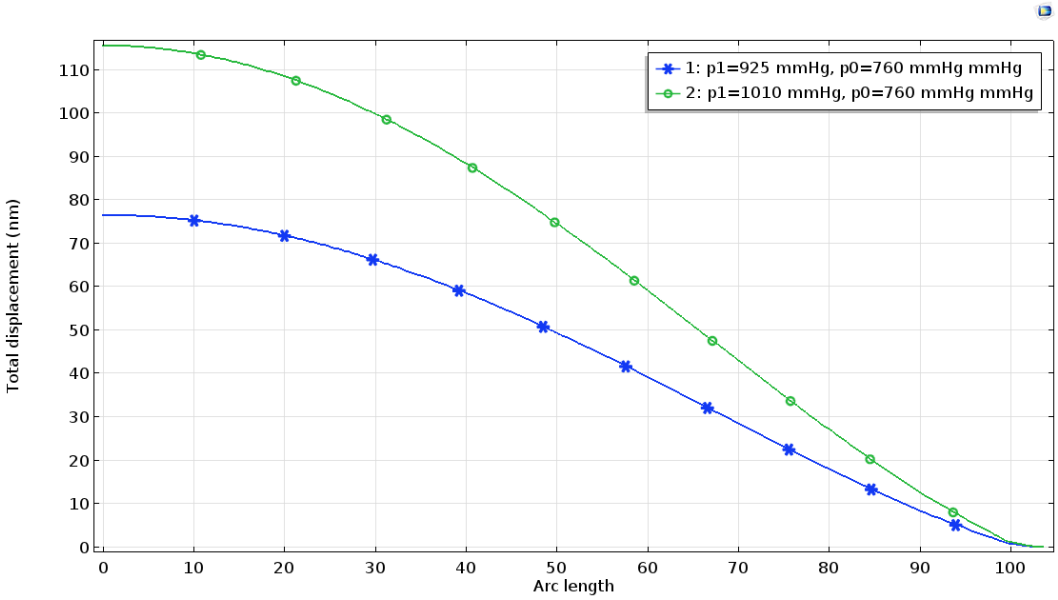

(a) Simulation result for the deflection of the membrane.

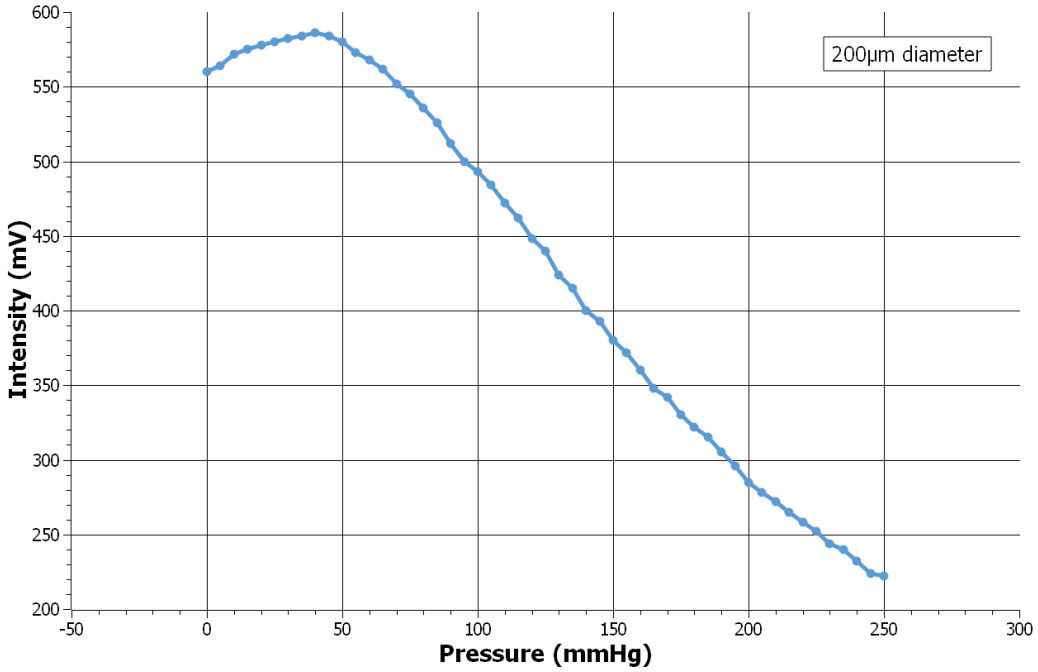

(b) Measured intensity change depending on the pressure value.

Figure 4.43. Simulated and measured membrane deflections for 200 μm diameter membrane.

From Figure 4.43, it can be seen that the simulation result of the deflection of the membrane is $\approx$ 118 nm in the middle of the membrane, where the measured deflection is 127.4 nm.

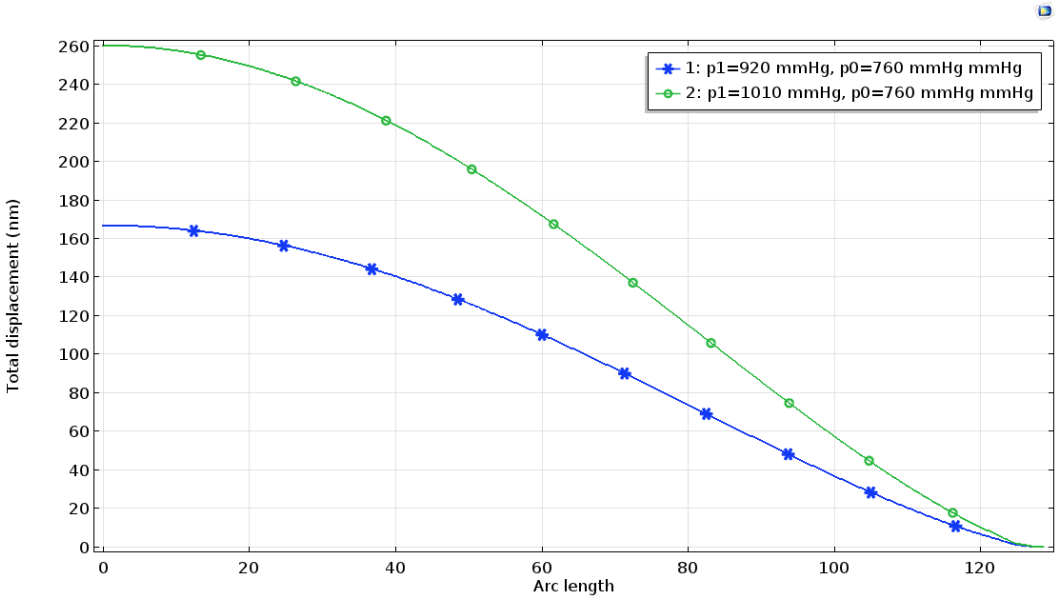

(a) Simulation result for the deflection of the membrane.

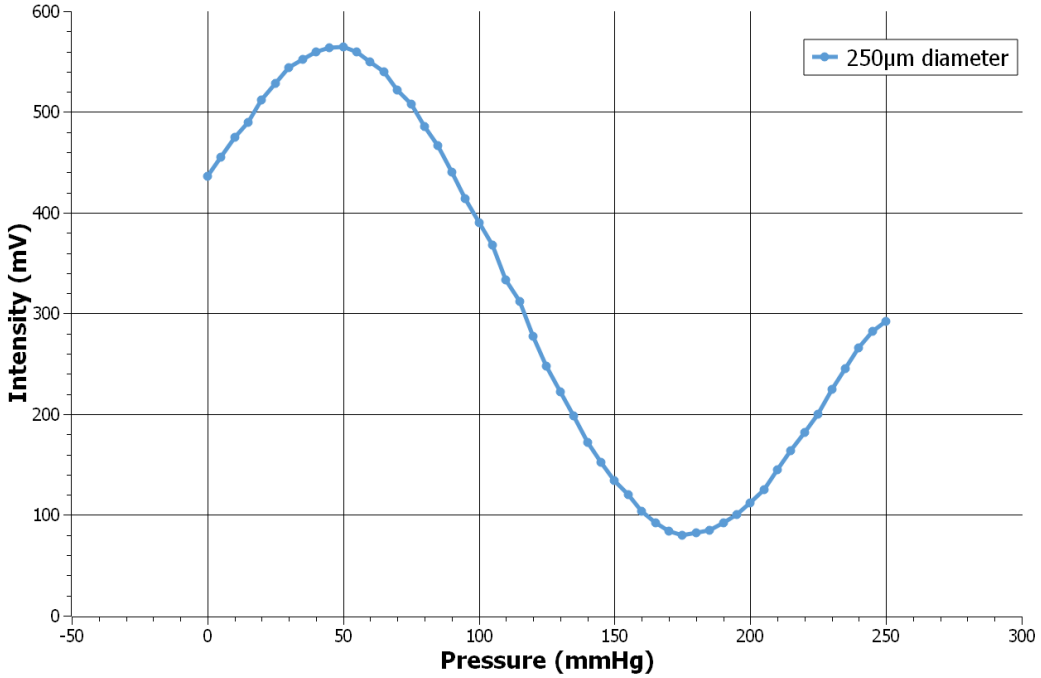

(b) Measured intensity change depending on the pressure value.

Figure 4.44. Simulated and measured membrane deflections for 250 μm diameter membrane.

From Figure 4.44, the simulation result of the deflection of the membrane is $\approx$ 260 nm in the middle of the membrane, where the measured deflection is 254.8 nm.

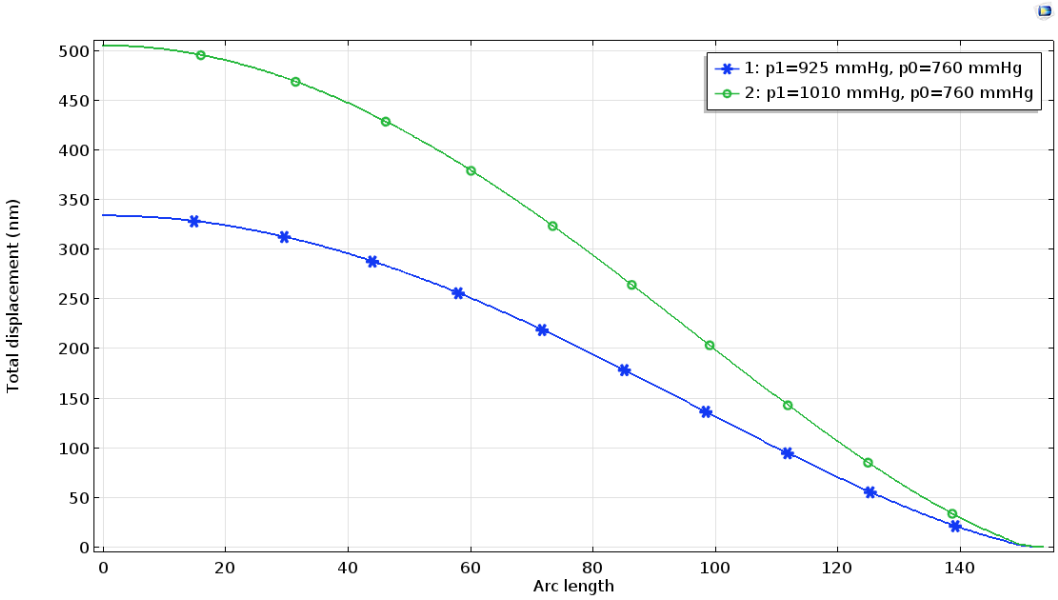

(a) Simulation result for the deflection of the membrane.

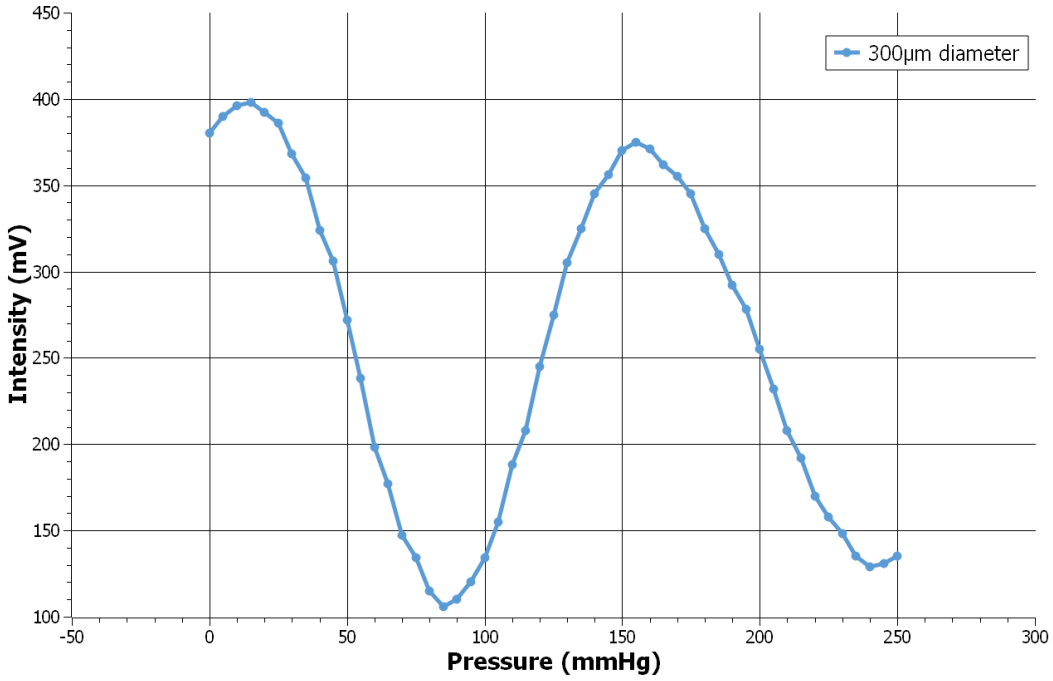

(b) Measured intensity change depending on the pressure value.

Figure 4.45. Simulated and measured membrane deflections for 300 μm diameter membrane.

From Figure 4.45, the simulation result of the deflection of the membrane is $\approx$ 508 nm in the middle of the membrane, the deflection measured as 509.6 nm.

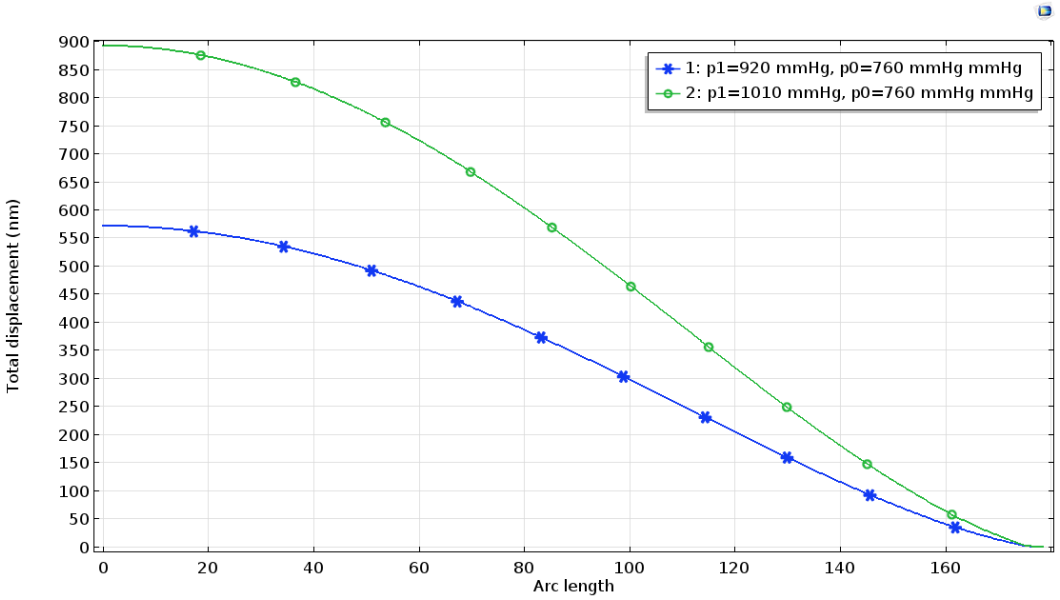

(a) Simulation result for the deflection of the membrane.

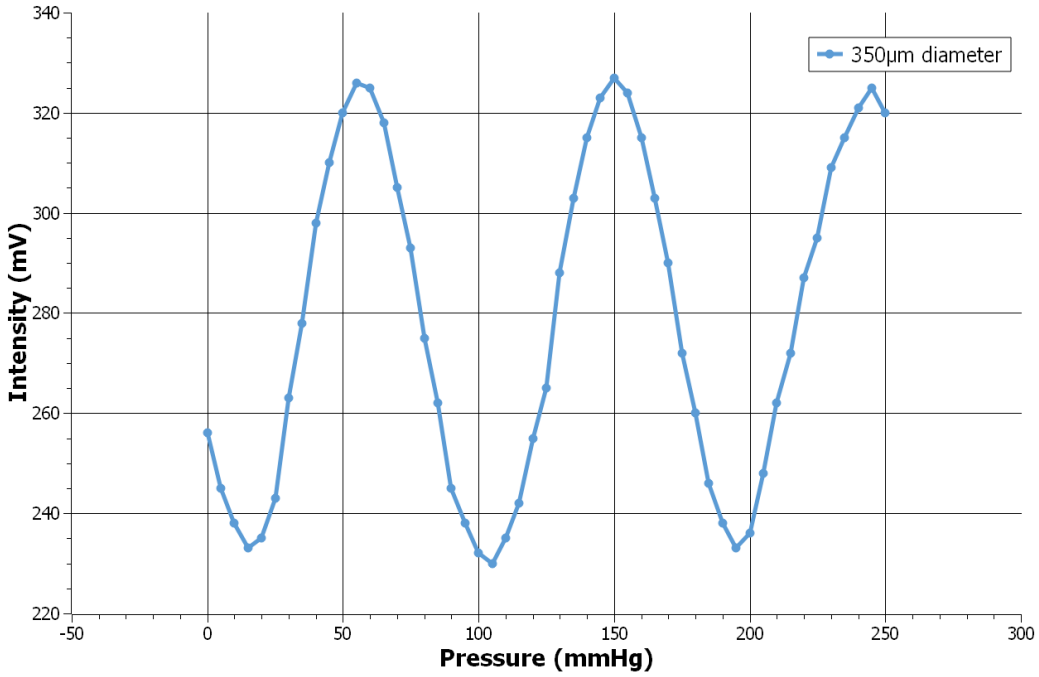

(b) Measured intensity change depending on the pressure value.

Figure 4.46. Simulated and measured membrane deflections for 350 μm diameter membrane.

From Figure 4.46, the simulated membrane deflection gives result as $\approx$ 890 nm in the middle of the membrane, and the deflection measured as 891 nm.

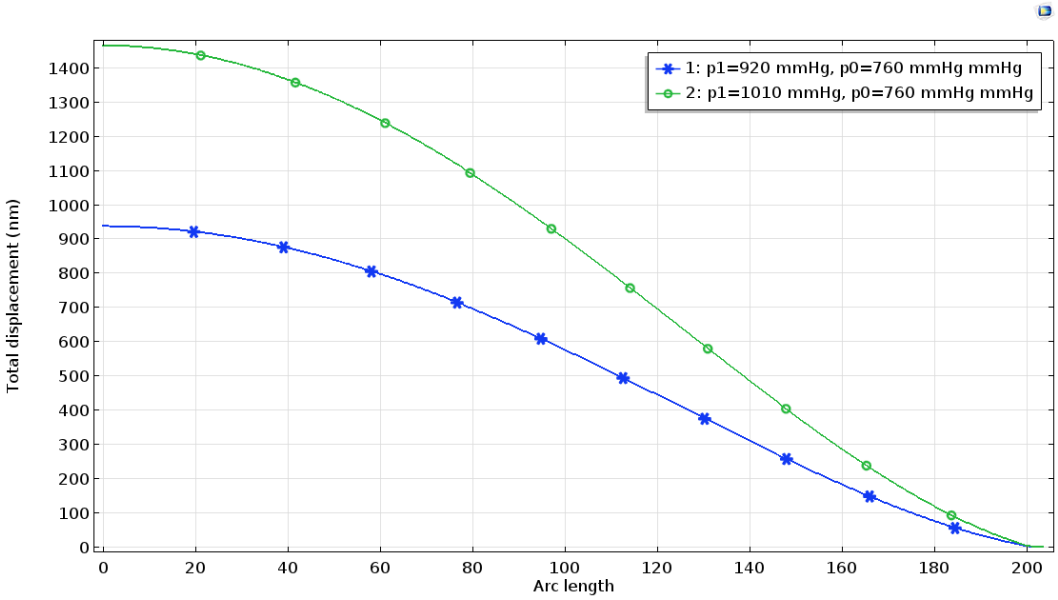

(a) Simulation result for the deflection of the membrane.

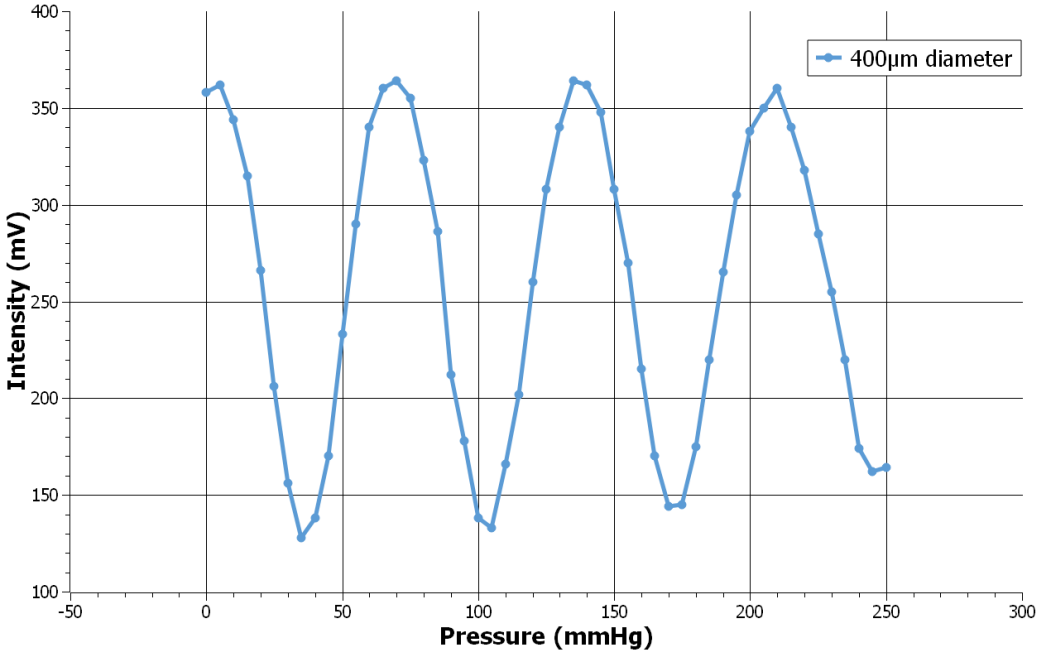

(b) Measured intensity change depending on the pressure value.

Figure 4.47. Simulated and measured membrane deflections for 400 μm diameter membrane..

As it can be seen from Figure 4.47, the simulation result of the deflection of the membrane is $\approx$ 1470 nm in the middle of the membrane, where the deflection is measured as 1210 nm.

Table 4.1. Simulation and Measurement Results of Deflection of the Membranes.

	Simulated Deflection	**Sine Cycles**	**Measured Deflection**
200 μm	118 nm	0.4	127.4 nm
250 μm	260 nm	0.8	254.8 nm
300 μm	508 nm	1.6	509.6 nm
350 μm	890 nm	2.8	891 nm
400 μm	1470 nm	3.8	1210 nm

According to the Table 4.1, the simulated and measured deflection rates are very close to each other. Some differences are caused by the non-ideal etching processes. Also, as it is expecting, membranes which are larger surface areas, deflected more than smaller sized ones. From the measured cycle numbers of the sine waves, it is observed that using 200 μm and 250 μm membranes are more suitable to use to detect the blood pressure changes in between 80-140 mmHg range, since the sensitivity values are calculated as 1.456 mV/mmHg and 1.884 mV/mmHg respectively from the reflected light.

5. CONCLUSION

In this thesis, a fiber optic integrated sensor microsystem is designed, fabricated and characterized. The main principle of the system is for catheter tracking for interventional operations in MRI. At the same time, device is able to track the body reactions as body temperature and blood pressure during operation. As system works under strong external magnetic field in MRI, data transmission is realized optically.

The described optical system consists of a localization, a temperature, a pressure sensor and an adaptor that holds together three sensors. The localization sensor detects the real time location of the catheter with using MRI gradients that shows an alteration in 30 mT range. The Magneto Optical Kerr Effect (MOKE) is adapted method to detect the location change in accordance with changed magnetic field. As a theory, MOKE is a change on the polarization of the light that reflected from a magnetic sample. To use this effect for catheter tracking, a micro-sized sample can be fabricate on the tip of the catheter and with a polarization maintaining cable, magnetic field effects on the light can be observable . As proof of concept work, a steel material is used to observe this effect. A polarized light beam is collimated with convex lenses and illuminated on the shiny surface of the ferromagnetic material and reflected light is detected with polarimeter. Here, as applied magnetic field changes on the steel, samples magnetization changes according to its M-H curve. Changing the magnetization effects the B field on the light as an EM wave, and accordingly, the E field either. Changing E field creates some polarization changes of the light which can detect by polarimeter. The polarimeter can detect the little changes of azimuth and elliptical angles, which are also identified as Kerr angles, and also, correspondingly, the power of the light.

At air optical setup of SS430 sample, observed minimum ΔH detection from azimuth degree change graph is 54 A/m H thus, the minimum localization change is calculated as 2.25 mm. Also, for the same setup, from the power change graph, ΔH observed as 12.94 A/m which corresponds 0.54 mm precision in localization change.

For the fiber optical setup with SS430, from the azimuth degree change results, the minimum detectable ΔH is calculated as 23.13 A/m. which corresponds 0.967 mm precision in the localization distance for the catheter. The power change gives results in ΔH change as 11.4 A/m by the experimental setup, which means 0.475 mm precision of the tracking device is detectable.

As the steel magnetically saturates at small magnetic fields, it is decided to use Fe_2O_3 which is not saturating at larger magnetic fields. From the experimental setup, obtained azimuth degree gives minimum ΔH as 106.36 A/m. So that, the precision of the catheter tracking can be calculated in 4.44 mm precision. Also, for this setup, the change in ellipticity degree is observed. The minimum ΔH is obtained as 254.865 A/m which means, the medical device in MRI can be tracked in 10.65 mm. However, from the power change graph, the change is observed according to magnetic field change, but obtained data do not gave meaningful results.

For the measurement of the body temperature, the used method is bandgap technology. According to changing the semiconductors temperature, the energy band gap in between valance and conduction bands. The GaAs is chosen as a semiconductor material. Illuminated near IR light can pass through the GaAs sample at room temperature. However, changing the temperature of the sample causes the interatomic spacing in between the bands and shifts on its transmission spectrum to higher or lower wavelengths. As more energy enters the crystal in the form of heat, the band gap narrows, and less additional energy is required to activate an electron. Thus, increasing the temperature of the sample causes to increasing the absorption coefficient of the sample and transmitted light's intensity becomes lower. Same effect can be observed by decreasing the temperature in opposite way.

To detect the temperature change, an available p type GaAs sample is used for experimental measurements. First, IR LED light sources exposed on the GaAs sample at room temperature. Then, the transmission effects depending on the temperature is observed with changing the temperature of the GaAs sample which located inside a water chamber. According to measurements, the minimum detectable temperature

change is reported as 1.215 °C and the sensitivity of the sensor is calculated as 0.494 nm/°C.

Also, the smoothly diced GaAs samples are going to be attached to the micro-fabricated structures and this sensor will become usable in interventional applications.

To measure the blood pressure, a micro structured membrane is microfabricated with sequential cleanroom processes. With the idea of interferometric optical readout method, a diffraction grating structures are fabricated with 3 μm size and 100 μm length. Different sized membranes, which is planned to bend with the effect of the external pressure, are fabricated as a sandwich structure with titanium and parylene layers in 200 μm, 250 μm, 300 μm, 350 μm and 400 μm diameters. The 2-λ readout method is used to improve the sensitivity for detection. The first diffraction order is used to monitor the membrane deflection. It is observed that membranes that are fabricated with 200 μm and 250 μm diameter size are usable to blood pressure measuring. As the measurements are taken in between 0 - 250 mmHg interval, the sensitivities are calculated as 1.456 mV/mmHg and 1.884 mV/mmHg respectively.

As a result, all of the fibers, which are carrying the sensor data, are coupled with substrate and merged with GRIN lenses in a single, 2.2 mm thick cylindrical 3D printed holder. This encapsulated structure is going to be used in catheters in in-vivo interventional applications.

APPENDIX A: GaAs SAMPLE PROPERTIES

Table A.1. P type GaAs technical properties [80].

Quality	GaAs
Materials	GaAS
Size	4”
Thickness	350±25 (μm)
Polished	Single Side
Dopant	Boron (P type)
Orientation	100
Resistivity	(1.2-9.9)E-3
Mobility	1000-3000
EPD	$\leq$ 3000
Growth Method	VGF
OF Lenght	17±1
IF Lenght	7±1

APPENDIX B: SPECTRAL DISTRIBUTIONS OF USED LED

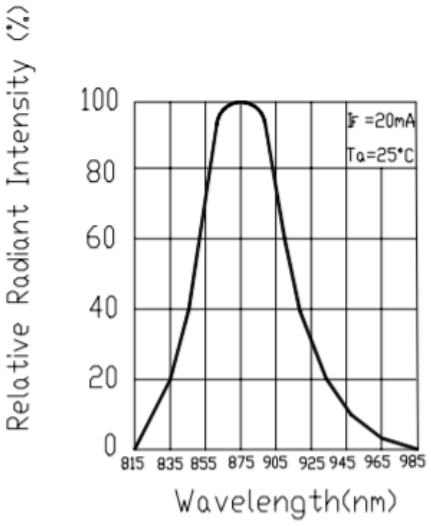

Figure B.1. Spectral distribution of 875nm LED.

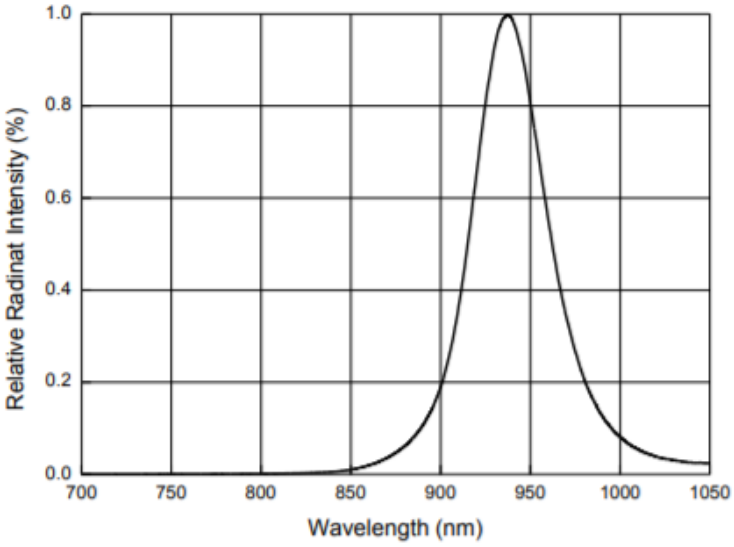

Figure B.2. Spectral distribution of 940nm LED.

APPENDIX C: STAINLESS STEEL MAGNETIZATION CURVE

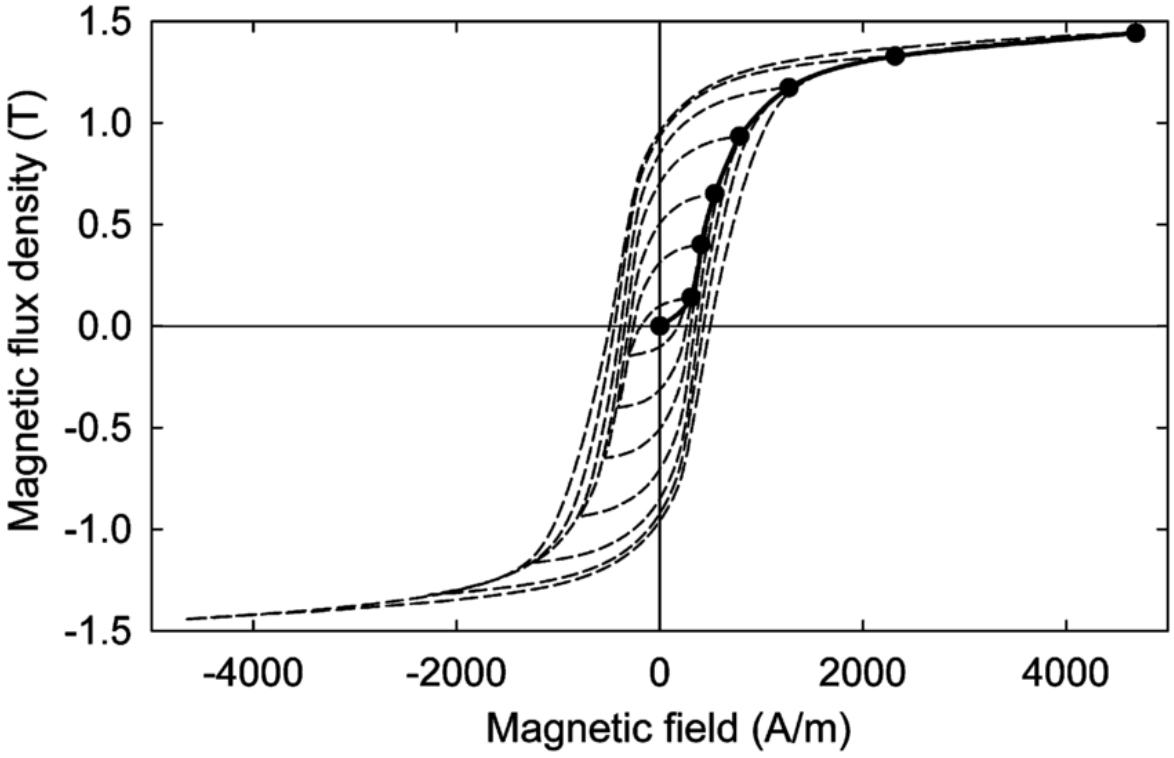

Figure C.1. B-H hysteresis curve of Stainless Steel 430.

REFERENCES

1. Kleinerman, R. A., "Cancer risks following diagnostic and therapeutic radiation exposure in children", *Pediatric radiology*, Vol. 36, No. 2, pp. 121–125, 2006.

2. Bushong, S., *Magnetic Resonance Imaging: Physical and Biological Principles*, The CV Mosy Company, St, 1988.

3. Reinhardt, H. F. and H. Landolt, "CT-guided "real time" stereotaxy", *Advances in Stereotactic and Functional Neurosurgery 8*, pp. 107–108, Springer, 1989.

4. Hynynen, K., R. Roemer, D. Anhalt, C. Johnson, Z. Xu, W. Swindell and T. Cetas, "A scanned, focused, multiple transducer ultrasonic system for localized hyperthermia treatments", *International Journal of Hyperthermia*, Vol. 3, No. 1, pp. 21–35, 1987.

5. Barnett, G. H., D. W. Kormos, C. P. Steiner and J. R. Weisenberger, "Use of a frameless, armless stereotactic wand for brain tumor localization with two-dimensional and three-dimensional neuroimaging", *Neurosurgery*, Vol. 33, No. 4, pp. 674–678, 1993.

6. Gumprecht, H. K., D. C. Widenka and C. B. Lumenta, "Brain Lab VectorVision neuronavigation system: technology and clinical experiences in 131 cases", *Neurosurgery*, Vol. 44, No. 1, pp. 97–104, 1999.

7. Nolte, L., L. Zamorano, H. Visarius, U. Berlemann, F. Langlotz, E. Arm and O. Schwarzenbach, "Clinical evaluation of a system for precision enhancement in spine surgery", *Clinical Biomechanics*, Vol. 10, No. 6, pp. 293–303, 1995.

8. Webster, J. G., *Minimally invasive medical technology*, CRC Press, 2016.

9. Andreassi, M. G., L. Ait-Ali, N. Botto, S. Manfredi, G. Mottola and E. Picano,

"Cardiac catheterization and long-term chromosomal damage in children with congenital heart disease", *European heart journal*, Vol. 27, No. 22, pp. 2703–2708, 2006.

10. Tweedle, M. F. and K. Kumar, "Magnetic resonance imaging (MRI) contrast agents", *Metallopharmaceuticals II*, pp. 1–43, Springer, 1999.

11. Tatli, S., P. R. Morrison, K. Tuncali and S. G. Silverman, "Interventional MRI for oncologic applications", *Techniques in Vascular and Interventional Radiology*, Vol. 10, No. 2, pp. 159–170, 2007.

12. Yang, X. and E. Atalar, "Intravascular MR imaging-guided balloon angioplasty with an MR imaging guide wire: feasibility study in rabbits", *Radiology*, Vol. 217, No. 2, pp. 501–506, 2000.

13. Lardo, A. C., E. R. McVeigh, P. Jumrussirikul, R. D. Berger, H. Calkins, J. Lima and H. R. Halperin, "Visualization and temporal/spatial characterization of cardiac radiofrequency ablation lesions using magnetic resonance imaging", *Circulation*, Vol. 102, No. 6, pp. 698–705, 2000.

14. Ozturk, C., M. Guttman, E. R. McVeigh and R. J. Lederman, "Magnetic resonance imaging–guided vascular interventions", *Topics in magnetic resonance imaging: TMRI*, Vol. 16, No. 5, p. 369, 2005.

15. Susil, R. C., C. J. Yeung, H. R. Halperin, A. C. Lardo and E. Atalar, "Multifunctional interventional devices for MRI: a combined electrophysiology/MRI catheter", *Magnetic Resonance in Medicine: An Official Journal of the International Society for Magnetic Resonance in Medicine*, Vol. 47, No. 3, pp. 594–600, 2002.

16. Lederman, R. J., M. A. Guttman, D. C. Peters, R. B. Thompson, J. M. Sorger, A. J. Dick, V. K. Raman and E. R. McVeigh, "Catheter-based endomyocardial injection with real-time magnetic resonance imaging", *Circulation*, Vol. 105, No. 11, pp.

1282–1284, 2002.

17. Rickers, C., M. Jerosch-Herold, X. Hu, N. Murthy, X. Wang, H. Kong, R. T. Seethamraju, J. Weil and N. M. Wilke, "Magnetic resonance image-guided transcatheter closure of atrial septal defects", *Circulation*, Vol. 107, No. 1, pp. 132–138, 2003.

18. Kuehne, T., S. Yilmaz, C. Meinus, P. Moore, M. Saeed, O. Weber, C. Higgins, T. Blank, E. Elsaesser, B. Schnackenburg, P. Ewert, P. Lange and E. Nagel, "Magnetic resonance imaging-guided transcatheter implantation of a prosthetic valve in aortic valve position: Feasibility study in swine", *Journal of the American College of Cardiology*, Vol. 44, pp. 2247–9, 01 2005.

19. Horvath, K. A., M. Li, D. Mazilu, M. A. Guttman and E. R. McVeigh, "Real-time magnetic resonance imaging guidance for cardiovascular procedures", *Seminars in thoracic and cardiovascular surgery*, Vol. 19, pp. 330–335, Elsevier, 2007.

20. Dickfeld, T., R. Kato, M. Zviman, S. Lai, G. Meininger, A. C. Lardo, A. Roguin, D. Blumke, R. Berger, H. Calkins *et al.*, "Characterization of radiofrequency ablation lesions with gadolinium-enhanced cardiovascular magnetic resonance imaging", *Journal of the American College of Cardiology*, Vol. 47, No. 2, pp. 370–378, 2006.

21. Schalla, S., M. Saeed, C. B. Higgins, A. Martin, O. Weber and P. Moore, "Magnetic resonance–guided cardiac catheterization in a swine model of atrial septal defect", *Circulation*, Vol. 108, No. 15, pp. 1865–1870, 2003.

22. Çamlı, B., *Design and characterization of the power supply unit and driver blocks of a CMOS based localization system for MRI*, Ph.D. Thesis, Boğaziçi University, 2013.

23. Fink, C., M. Bock, R. Umathum, S. Volz, S. Zuehlsdorff, R. Grobholz, H.-U. Kauczor and P. Hallscheidt, "Renal embolization: feasibility of magnetic resonance-

guidance using active catheter tracking and intraarterial magnetic resonance angiography", *Investigative radiology*, Vol. 39, No. 2, pp. 111–119, 2004.

24. Hofmann, L. V., R. P. Liddell, J. Eng, B. A. Wasserman, A. Arepally, D. S. Lee and D. A. Bluemke, "Human peripheral arteries: feasibility of transvenous intravascular MR imaging of the arterial wall", *Radiology*, Vol. 235, No. 2, pp. 617–622, 2005.

25. Quick, H. H., H. Kuehl, G. Kaiser, S. Bosk, J. F. Debatin and M. E. Ladd, "Inductively coupled stent antennas in MRI", *Magnetic Resonance in Medicine: An Official Journal of the International Society for Magnetic Resonance in Medicine*, Vol. 48, No. 5, pp. 781–790, 2002.

26. Glowinski, A., J. Kursch, G. Adam, A. Bucker, T. G. Noll and R. Gunther, "Device visualization for interventional MRI using local magnetic fields: basic theory and its application to catheter visualization", *IEEE Transactions on Medical Imaging*, Vol. 17, No. 5, pp. 786–793, 1998.

27. Dumoulin, C. L., R. D. Darrow, J. F. Schenck and S. P. Souza, "Tracking system to follow the position and orientation of a device with radiofrequency field gradients", Google Patents, May 1993, uS Patent 5,211,165.

28. Hillenbrand, C. M., D. R. Elgort, E. Y. Wong, A. Reykowski, F. K. Wacker, J. S. Lewin and J. L. Duerk, "Active device tracking and high-resolution intravascular MRI using a novel catheter-based, opposed-solenoid phased array coil", *Magnetic Resonance in Medicine: An Official Journal of the International Society for Magnetic Resonance in Medicine*, Vol. 51, No. 4, pp. 668–675, 2004.

29. Shellock, F. G., "Radiofrequency energy-induced heating during MR procedures: a review", *Journal of Magnetic Resonance Imaging*, Vol. 12, No. 1, pp. 30–36, 2000.

30. Ladd, M. E. and H. H. Quick, "Reduction of resonant RF heating in intravascular catheters using coaxial chokes", *Magnetic Resonance in Medicine: An Official Journal of the International Society for Magnetic Resonance in Medicine*, Vol. 43,

No. 4, pp. 615–619, 2000.

31. Weiss, S., P. Vernickel, T. Schaeffter, B. Gleich and V. Schulz, "Towards an RF-safe active catheter for MR-guided interventions", *Kontraste (Hamburg)*, Vol. 49, No. 3, pp. 48–53, 2005.

32. Woodward, T. and A. V. Krishnamoorthy, "1-Gb/s integrated optical detectors and receivers in commercial CMOS technologies", *IEEE Journal of Selected Topics in Quantum Electronics*, Vol. 5, No. 2, pp. 146–156, 1999.

33. Razavi, B., "Prospects of CMOS technology for high-speed optical communication circuits", *IEEE Journal of Solid-State Circuits*, Vol. 37, No. 9, pp. 1135–1145, 2002.

34. Guilar, N. J., T. J. Kleeburg, A. Chen, D. R. Yankelevich and R. Amirtharajah, "Integrated solar energy harvesting and storage", *IEEE Transactions on Very Large Scale Integration (VLSI) Systems*, Vol. 17, No. 5, pp. 627–637, 2009.

35. Schanze, T., L. Hesse, C. Lau, N. Greve, W. Haberer, S. Kammer, T. Doerge, A. Rentzos and T. Stieglitz, "An optically powered single-channel stimulation implant as test system for chronic biocompatibility and biostability of miniaturized retinal vision prostheses", *IEEE Transactions on Biomedical Engineering*, Vol. 54, No. 6, pp. 983–992, 2007.

36. Wu, M. C., O. Solgaard and J. E. Ford, "Optical MEMS for lightwave communication", *Journal of Lightwave Technology*, Vol. 24, No. 12, pp. 4433–4454, 2006.

37. Savastano, L., G. Maier, A. Pattavina and M. Martinelli, "Physical-parameter design in 2-D MEMS optical switches", *Journal of Lightwave Technology*, Vol. 23, No. 10, pp. 3147–3155, 2005.

38. Yu, K., D. Lee, N. Park and O. Solgaard, "Tunable optical bandpass filter with variable-aperture MEMS reflector", *Journal of Lightwave Technology*, Vol. 24,

No. 12, pp. 5095–5102, 2006.

39. Lee, C., "A MEMS VOA using electrothermal actuators", *Journal of Lightwave Technology*, Vol. 25, No. 2, pp. 490–498, 2007.

40. Mikov, A. and V. Svirin, "Laser therapy in oncological diseases and its hardware implementation", *Meditsinskaia Tekhnika*, Vol. 141, No. 4, p. 26, 2009.

41. Barkin, J., "HIFU: Definitely ready for prime time", *Canadian Urological Association Journal*, Vol. 5, No. 6, p. 422, 2011.

42. Wilber, D. J., C. Pappone, P. Neuzil, A. De Paola, F. Marchlinski, A. Natale, L. Macle, E. G. Daoud, H. Calkins, B. Hall *et al.*, "Comparison of antiarrhythmic drug therapy and radiofrequency catheter ablation in patients with paroxysmal atrial fibrillation: a randomized controlled trial", *Jama*, Vol. 303, No. 4, pp. 333–340, 2010.

43. Erez, A. and A. Shitzer, "Controlled destruction and temperature distributions in biological tissues subjected to monoactive electrocoagulation", *Journal of Biomechanical Engineering*, Vol. 102, No. 1, pp. 42–49, 1980.

44. Baek, J. H., J. H. Lee, R. Valcavi, C. M. Pacella, H. Rhim and D. G. Na, "Thermal ablation for benign thyroid nodules: radiofrequency and laser", *Korean Journal of Radiology*, Vol. 12, No. 5, pp. 525–540, 2011.

45. Zarrabi, A. and A. J. Gross, "The evolution of lasers in urology", *Therapeutic advances in urology*, Vol. 3, No. 2, pp. 81–89, 2011.

46. Blana, A., S. C. Brown, C. Chaussy, G. N. Conti, J. A. Eastham, R. Ganzer, F. J. Murat, G. Pasticier, X. Rebillard, J. C. Rewcastle *et al.*, "High-intensity focused ultrasound for prostate cancer: comparative definitions of biochemical failure", *BJU international*, Vol. 104, No. 8, pp. 1058–1062, 2009.

47. Jai¨ s, P., M. Hai¨ ssaguerre, D. C. Shah, S. Chouairi, L. Gencel, M. l. Hocini and

J. Cle´ menty, “A focal source of atrial fibrillation treated by discrete radiofrequency ablation”, *Circulation*, Vol. 95, No. 3, pp. 572–576, 1997.

48. Testani, J. M., S. G. Coca, B. D. McCauley, R. P. Shannon and S. E. Kimmel, “Impact of changes in blood pressure during the treatment of acute decompensated heart failure on renal and clinical outcomes”, *European Journal of Heart Failure*, Vol. 13, No. 8, pp. 877–884, 2011.

49. Pollak, J. T., M. Neimark, J. T. Connor and G. W. Davila, “Air-charged and microtransducer urodynamic catheters in the evaluation of urethral function”, *International Urogynecology Journal*, Vol. 15, No. 2, pp. 124–128, 2004.

50. Cooper, M., P. Fletter, P. Zaszczurynski and M. Damaser, “Comparison of air-charged and water-filled urodynamic pressure measurement catheters”, *Neurourology and Urodynamics*, Vol. 30, No. 3, pp. 329–334, 2011.

51. Wang, Q., H. R. Brunner and M. Burnier, “Determination of cardiac contractility in awake unsedated mice with a fluid-filled catheter”, *American Journal of Physiology-Heart and Circulatory Physiology*, Vol. 286, No. 2, pp. H806–H814, 2004.

52. Roriz, P., A. Ramos, J. L. Santos and J. A. Simões, “Fiber optic intensity-modulated sensors: A review in biomechanics”, *Photonic Sensors*, Vol. 2, No. 4, pp. 315–330, 2012.

53. Roriz, P., O. Frazão, A. B. Lobo-Ribeiro, J. L. Santos and J. A. Simões, “Review of fiber-optic pressure sensors for biomedical and biomechanical applications”, *Journal of Biomedical Optics*, Vol. 18, No. 5, p. 050903, 2013.

54. Rubin, D. L., A. V. Ratner and S. W. Young, “Magnetic susceptibility effects and their application in the development of new ferromagnetic catheters for magnetic resonance imaging.”, *Investigative Radiology*, Vol. 25, No. 12, pp. 1325–1332, 1990.

55. Bakker, C. J., R. M. Hoogeveen, J. Weber, J. J. van Vaals, M. A. Viergever and W. P. Mali, "Visualization of dedicated catheters using fast scanning techniques with potential for MR-guided vascular interventions", *Magnetic Resonance in Medicine*, Vol. 36, No. 6, pp. 816–820, 1996.

56. Bock, M., R. Umathum, J. Sikora, S. Brenner, E. Aguor and W. Semmler, "A Faraday effect position sensor for interventional magnetic resonance imaging", *Physics in Medicine & Biology*, Vol. 51, No. 4, p. 999, 2006.

57. Wang, W., "Magnetic resonance–guided active catheter tracking", *Magnetic Resonance Imaging Clinics*, Vol. 23, No. 4, pp. 579–589, 2015.

58. Qiu, Z. and S. D. Bader, "Surface magneto-optic Kerr effect", *Review of Scientific Instruments*, Vol. 71, No. 3, pp. 1243–1255, 2000.

59. Serway, R. A. and J. W. Jewett, *Physics for scientists and engineers with modern physics*, Cengage learning, 2018.

60. Thorlabs, *Thorlabs PAX1000 Operation Manual*, Thorlabs, `https://www.thorlabs.com/thorproduct.cfm?partnumber=PAX1000IR1/M"`, Accessed May 2019.

61. Hecht, E., *Optics, 5e*, Pearson Education India, 2002.

62. Hamrle, J., *Magneto-optical determination of the in-depth magnetization profile in magnetic multilayers*, Theses, Université Paris Sud - Paris XI, Mar. 2003, `https://tel.archives-ouvertes.fr/tel-00002948`.

63. Yamamoto, S. and I. Matsuda, "Measurement of the resonant magneto-optical kerr effect using a free electron laser", *Applied Sciences*, Vol. 7, No. 7, p. 662, 2017.

64. Schmitte, T., "Bragg-moke and vector-moke investigations: Magnetic reversal of patterned microstripes", *Doktorarbeit Experimentalphysik IV, Ruhr-Universität Bochum*, 2002.

65. Buchenberg, W. B., T. Dadakova, J. Groebner, M. Bock and B. Jung, "Comparison of two fiber-optical temperature measurement systems in magnetic fields up to 9.4 Tesla", *Magnetic resonance in medicine*, Vol. 73, No. 5, pp. 2047–2051, 2015.

66. Çirkinoğlu, H. O., H. Bilgin, F. Civitci, H. Torun and O. Ferhanoğlu, "Fiber temperature sensor utilizing a thermomechanical MEMS detector", *Journal of Lightwave Technology*, Vol. 34, No. 3, pp. 1025–1030, 2015.

67. Micronor, *GaAs temperature sensing system (TS Temperature Sensors).*, 2014, `https://micronor.com/products/ts-temperature-sensors/`, Accessed May 2020.

68. Barbarino, G., R. De Asmundis, G. De Rosa, C. M. Mollo, S. Russo and D. Vivolo, "Silicon photo multipliers detectors operating in geiger regime: an unlimited device for future applications", *Photodiodes-World Activities in 2011*, InTechOpen, 2011.

69. Buana, C. W. S., *Gallium arsenide spectrum shift.*, 2011, `http://www.cwsb.co.id/product/328/Fiber-Optic-GaAs-principle-and-the-temperature-sensor.html`, Accessed May 2020.

70. Chmill, V., *Radiation tests of semiconductor detectors*, Ph.D. Thesis, KTH, 2006.

71. Schroder, D. K., *Semiconductor material and device characterization*, John Wiley & Sons, 2015.

72. Harris, T. R., *Optical Properties of Si, Ge, GaAs, GaSb, InAs, and InP at Elevated Temperatures*, Master's Thesis, Air Force Institute of Technology, 2010.

73. Brancato, L., G. Keulemans, T. Verbelen, B. Meyns and R. Puers, "An implantable intravascular pressure sensor for a ventricular assist device", *Micromachines*, Vol. 7, No. 8, p. 135, 2016.

74. LIGO-Caltech, *What is an Interferometer?*, 1984, `https://www.ligo.caltech.edu/page/what-is-interferometer`, Accessed

August 2020.

75. Wolfe, G., E. Gasper and J. Kretchman, *College Physics for AP® Courses*, Rice University, 2015.

76. Torun, H., *Design and fabrication of thermo-mechanical thermal detector arrays with optical readout*, Ph.D. Thesis, Koç University, 2005.

77. MIT, *Physics Open Course, Chapter 14: Interference and Diffraction*, 2007, `http://staff.ustc.edu.cn/ bjye/em/MIT-ID.pdf`, Accessed July 2020.

78. Torun, H., J. Sutanto, K. K. Sarangapani, P. Joseph, F. Degertekin and C. Zhu, "A micromachined membrane-based active probe for biomolecular mechanics measurement", *Nanotechnology*, Vol. 18, No. 16, p. 165303, 2007.

79. Hall, N. A. and F. L. Degertekin, "Integrated optical interferometric detection method for micromachined capacitive acoustic transducers", *Applied Physics Letters*, Vol. 80, No. 20, pp. 3859–3861, 2002.

80. Nanografi, *Gallium Arsenide (GaAs) Wafer Size: 2, Thickness: 350±25 µm, Single Side Polished Technical Properties*, 2011, `https://nanografi.com/silicon-wafers-semiconductor-wafers/gaas-wafer/`, Accessed May 2020.